Optimization of a Cover Design for Acid Rock Drainage Prevention in a Permafrost Environment

by

Hilary Louise Smith

A thesis submitted in partial fulfillment of the requirements for the degree of

Master of Science

in

Geoenvironmental Engineering

Department of Civil and Environmental Engineering
University of Alberta

Abstract

The extraction of sulfide-bearing waste rock can contribute to the generation of acid rock drainage (ARD). ARD is the effluent generated due to the oxidation of sulfide minerals which can be toxic to the receiving environment. Waste rock material which contains potentially acid-generating (PAG) material is often covered with a soil cover to mitigate the production of ARD. When a soil cover system is implemented in a permafrost environment such as northern Canada, it may realize additional PAG management capabilities as a result of annual freezing temperatures.

ARD is a known issue at the Diavik Diamond Mine (the Site). It is located on an island in Lac de Gras roughly 300 km northeast of Yellowknife, Northwest Territories. The Site is located on the boundary of continuous and discontinuous permafrost with an active layer ranging between 1.5 and 5 m in depth. The mean annual average temperature of the Site was determined to be -8.9°C.

The waste material at this Site is separated according to sulfide content and therefore its acid-generating potential. The key material types included in this research include the Type I (T1) material which is classified as non acid generating (NAG), Type III (T3) material (PAG), and till material (NAG). The bulk of the material on Site is the PAG T3 material, which is stored in a large, 80 m tall waste rock storage area called the North Country Stock Pile (WRSA-NCRP).

A proposed cover system for the WRSA-NCRA included 3.0 m of T1 waste rock overlying 1.5 m of a finer layer of till. The till material properties allow for the formation of a latent heat layer due to a low permeability and high moisture content. An adjustment to this design included the removal of fine fractions of the T1 material to form a higher permeability upper layer of the cover system with the intent to induce natural convective cooling. This material was denoted T1 (coarse), and the system was called an Air Convective Cover (ACC).

Previous research included the development of a simulation model to analyze this effectiveness of this ACC design on a structure like the WRSA-NCRP in a program called COMSOL Multiphysics® (Comsol). The field conditions were approximated assuming heat transfer and fluid flow coupling. This

simulation considered an annual surface temperature increase as a result of climate change. Results demonstrated the success of the soil cover system in maintaining the underlying PAG material frozen after 100 years.

This thesis builds on these findings in order to optimize the soil cover design prior to moving towards test cell recommendations for the WRSA-NCRP. The optimization process was designed to minimize volume requirements while maintaining the material frozen for the same long-term timeline of 100 years. Similar to previous modelling, this research will also account for an annual surface temperature increase due to climate change.

The key objectives in this research were to demonstrate a successful model benchmark analysis, conduct a sensitivity analysis, optimize soil cover thicknesses, and provide suggestions for future test cell constructions.

A model benchmarking analysis was established and the rebuilt model in Comsol was deemed an acceptable equivalence to the original model simulation. A sensitivity analysis explored the parameter uncertainties of the till volumetric moisture content, the T1 (coarse) permeability, and the annual temperature increase as a result of climate change. Each parameter had a functional range that would produce accurate and expected results.

The model optimization of the soil cover included different combinations of materials including T1 (coarse), T1 (all fraction), and till. The model optimization step provided options that account for material availability at the site. The accepted optimization combinations were further classified according to the definition of success for each simulation which provided four levels of added contingency. The optimized results from the lowest contingency buffer category were either 1.00 m T1 (Coarse) + 1.25 m Till or 2.00 m T1 (coarse) + 0.25 m Till. The highest contingency buffer resulted in an optimized prescription of 2.25 m T1 (coarse) + 1.25 m Till. Proposed field test plot prescriptions were generated according to these optimization results.

Land Acknowledgement

I would like to respectfully acknowledge that the land on which I have taken my coursework and written this thesis is Treaty 6 territory, which is the traditional and ancestral territory of the Anishinabae (Saulteaux), Denesuliné (Dene), Nakota Sioux (Stoney), Nehiyawak (Cree), and Niisitapi (Blackfoot) First Nations. I acknowledge that this territory is home to Métis Settlements and Métis Nation of Alberta, Regions 2, 3, and 4 within the historical Northwest Métis Homeland. Furthermore, I would like to recognize the specific land of amiskwacîwâskahikan (Edmonton) which has been occupied, travelled, and cared for by a diverse range of Indigenous peoples (First Nations, Métis, and Inuit) since time immemorial.

Additionally, I would like to respectfully acknowledge that this research is based on a site which is located on both traditional lands of the Akaitcho Peoples (Deninu K'u, Lutsel K'e Dene, and Yellowknives Dene) and the Tłı̨chǫ Nation (Dechi Laot'I, Dog Rib Rae, Gameti, and Wha Ti).

Personal Acknowledgements

It feels surreal to be at the point where I get to sit down and write these acknowledgements. I feel like I have been thinking about what I would say here for the entirety of my research and I hope I can adequately capture how much I have appreciated all of those who have contributed to this journey.

I must begin by thanking my supervisor, Dr. Nicholas Beier, who has been nothing short of extremely supportive and understanding through what has ended up being a *very* long two-year degree. The discussions that I have had over the years with Dr. Beier along with my co-supervisor Dr. David Sego have been extremely valuable and thought provoking through the challenges that have come with this research and I am thankful to have been able to learn from both of them.

To the Testpilers who came before me and paved the way for this research, particularly those that I had the opportunity to work with and learn from. Thank you, David Barsi, David Wilson, and Colleen Atherton. I also greatly appreciate Nam Pham who spent much of his personal time answering my seemingly infinite questions regarding this research.

To the remainder of the geotechnical department (past and present) who work so hard to keep everything working smoothly and even managed to do so during a global pandemic. I would like to specifically thank Sally Petaske, Annette Busenius, Christine Heregyers, Lucas Duerksen, and Jen Stogowski.

My time completing coursework and research has given me the good fortune to meet many people who I am lucky to consider my friends. To those that I took courses with or those that lapped me(!), thank you for all the support, academically and non-academically. I am honoured to have had this experience with you. Thank you to Umme Rima, Gabriella Wahl, Rebecca Hurtubise, Taylor Hall, Riley Morin, and Craig Unterschultz.

Of these friendships, a few require a specific mention. Kelsey Steinwand started and completed her own research at the same time as me and I am so thankful that she did – I can not imagine going through this process without her. I look forward to the next phase of our lives where we don't have to talk about formatting or chosen referencing software when we get together. I also want to thank Haley Schafer, who started as my unofficial geotech mentor (perhaps unknowingly) but who I now consider one of my closest friends. Thank you for always challenging me and supporting me through this process. It has been an honour to sometimes be mistaken for you.

To Vivian Giang and Dr. Ahlam Abdulnabi, the conversations I have had with both of you has made me not only a better engineer but more importantly a better human. I look forward to continuing these conversations. I feel hopeful for the future of our industry knowing you are both a part of it.

To my family who always wanted to help and support me even though this process was just as foreign to them as it felt to me some days. To my parents Diana and Steve, and my brothers Cory and Alexander, thank you so much. To both my grandmothers, Sandra and Melva, who both passed this year. I wish I could tell them that I finally finished, though I already know how proud they are of me.

I must also mention my dog Goose who was adopted in May 2020, despite the fact that getting a dog was supposed to be the *reward* for completing this thesis. He is going to be quite pleased with all the newfound time for walks.

Finally, I need to thank my partner Damien Charron, who has been the ultimate supporter of this work. His patience and understanding despite three and a half years of "sorry I can't, I am working on my thesis" or "we can do this once I have finished my thesis" has kept me mostly sane and encouraged me to complete this work. I am so thankful that you are in my life.

Table of Contents

List of Tables

List of Figures

1 Introduction

Mining is essential to maintain the quality of life that we rely on in Canada. According to the Government of Canada (2019), the Canadian mineral sector directly contributed $72.4 billion (3.5%) of the countries' total gross domestic product (GDP) in 2018. When accounting for the indirect impacts of the mining industry this brings the total contribution to $97.7 billion (4.7%) of Canada's 2018 GDP. Furthermore, the domestic mineral exports of Canada were valued at $104.6 billion, which represents 19% of total merchandise exports. While the economic benefits of the mining industry are evident and have historically been the main factor in future projects the environmental impacts of mining can no longer be ignored. The global mineral extraction sector is considered a significant contributor to an ever-growing list of environmental issues. As such, the practice of mining in the 21st century has become increasingly polarized, particularly in the wake of evident and worsening climate change impacts. Can Canada continue to exploit their natural resources while also maintaining a high level of environmental protection and integrity? While the debate is ongoing, there have been multiple fields of research established in order to combat and reduce the impacts of both well-understood and emerging environmental challenges.

Of all environmental concerns associated with the mining industry, a problem called acid rock drainage (ARD) is one of the most serious issues. This issue has an huge liability cost according to the Mining Association of Canada (MAC 2009). Over twenty years ago, the liability associated with the clean-up of Canada's ARD issues was estimated to be between $2 – 5 billion (MEND5.8.1 1995). Although an updated value has not been presented, by accounting for inflation, increased environmental regulations, and increased mining project sizes over the past twenty-five years the true estimate would be substantially larger. Putting the cost of liability aside, remediation strategies do not offer blanket solutions and they must be tailored to each individual project. This makes finding the answer to mitigating ARD complex and challenging. Through research and an increasing understanding of the ARD challenges in Canada, new technologies and methods for remediation have been discovered and are currently being implemented across the country.

In the past few decades, the industry has begun to improve on the historically environmentally damaging practices that have been around since large-scale mining operations began in Canada. With the drive to achieve a respected level of corporate social responsibility, today's companies must demonstrate a balance of not solely economic success, but also environmental and social stewardship. An example of this change was with the establishment of the Mine Environment

Neutral Drainage (MEND) program in 1989. This initiative was introduced to develop new technologies and encourage research into the prevention and control of ARD. This program is directed by a multi-stakeholder committee with members from industry, government, and non-government organizations (MEND 2017).

The astounding amount of effort being poured into ARD research both academically and through industry demonstrates how high of a priority it is to find functional mitigation efforts. In line with this, this thesis and supporting research is one of those projects. This document will focus on an individual mining operation with a climate-specific ARD problem and the proposed mitigation technique.

1.1 Statement of Problem

ARD is a chemical effluent present in most mining operations. This effluent can often pose a significant environmental risk to downstream surface and ground waterbodies. ARD is the resulting effluent of a chemical reaction (oxidation) where sulfide bearing rocks are exposed to air and water. The sulfides in these materials are naturally being weathered and releasing small amounts of ARD in situ prior to human intervention. However, the conditions imposed during mineral excavation (breaking of material which exposes more surfaces to water and oxygen) can expedite the problem and create volumes of ARD which are no longer able to be buffered by the receiving environment. The mitigation of ARD once the problem has reached the magnitudes that are seen in the mining industry is usually difficult and costly; however, there are a few unique strategies that may be successful when the climate is favourable. ARD is a known issue at the Diavik Diamond mine (the Site) in Northern Canada. The Site is located on a 20 km^2 island (East Island) in Lac de Gras, Northwest Territories as displayed in Figure 1-1. It is situated in a zone which is classified as a continuous permafrost environment. The mining of three kimberlite pipes has produced a large volume of waste rock on-site, much of which is considered potentially acid-generating (PAG) material. As outlined by Indigenous and Northern Affairs Canada et al. (IAND et al. 1999) the ultra-oligotrophic nature of the lake increases the impact that even small amounts of ARD can have and as such the acidic runoff must be prevented, mitigated, or addressed. The use of a two-layer, non acid-generating (NAG), convective soil cover in combination with the effects of surrounding permafrost temperatures has exhibited success in field-scale experiments (Pham 2013) in limiting the production of ARD. The full-scale pile has also demonstrated successful results in modelling simulations despite long term temperature increases. The next step in this research is to optimize the soil cover design prior to moving towards test cell recommendations for the full-scale structure. Successful results would demonstrate an optimized

soil cover simulation of NAG material which is able to keep the underlying PAG material frozen year-round for a duration of 100 years while accounting for a given climate change annual temperature increase.

Figure 1-1: Location of Diavik Diamond Mine
Reproduced from Smith et al. (2013a) with permission

1.2 Objectives and Scope of this Research

Pham (2013) developed a simulation model of the heat transfer and fluid flow conditions within the waste rock pile at the Site. This simulation was able to demonstrate the success of a proposed soil cover system that maintains the underlying PAG material frozen after 100 years under a given annual temperature increase. The current research aims to optimize this soil cover system and identify sensitive parameters in order to minimize required material volumes on the full-scale waste rock pile. The optimization process will be conducted using a modelling software called COMSOL Multiphysics® (Comsol) (Comsol 2018a, 2018b). This research uses a newer version (Comsol 5.4) than the one used by Pham (2013) (Comsol 3.4). The modelling environment was required to be rebuilt in order to upgrade model versions. As such, a benchmark study is included in this research to evaluate equivalence.

The specific objectives of this thesis are as follows:

1. Demonstrate a successful model benchmark analysis between this research and Pham (2013)'s model
2. Conduct a sensitivity analysis to determine the model robustness and uncertainty in assumed parameters
3. Optimize the soil cover thicknesses that will be sufficient to maintain frozen conditions after 100 years
4. Provide future suggestions for construction of test cells and potential soil cover prescriptions to be constructed on top of the full-scale waste rock pile

1.3 Organization of Thesis

This thesis is organized into five chapters and one appendix. Their purposes are defined below.

Chapter 1 introduces the problem statement and objectives of this work.

Chapter 2 provides a literature review to both demonstrate that this researcher has conducted the appropriate background research as well as to set a baseline for the reader. The literature review outlines general mining definitions, permafrost definitions and parameters, and the concept of ARD that may be generated during mining. Next is a description of key soil property definitions and the corresponding fluid dynamics and heat transfer mechanisms expected in a porous media. The soil cover design and function are presented and then site-specific information such as location, climate, reclamation plan, and previous research follow. Finally, this chapter concludes with the potential impacts of climate change, particularly those seen in an environment such as this Site.

Chapter 3 guides the reader through the general workflow of model building and considerations. This includes an introduction to the modelling software as well as the description of the base case research used for benchmarking purposes. Next, the modelling assumptions and limitations, geometry, governing equations, and physics modules are described. Specific modelling factors such as mesh size, model width, and step size follow. This chapter concludes with model benchmarking which compares the results to previous modelling and confirms that the reconstruction process was successful.

Chapter 4 describes the model analysis. The first portion of this chapter presents the sensitivity analysis which explores the sensitivity of the till volumetric moisture content, the T1 (coarse) permeability, and the annual temperature increase at the surface of the cover due to climate

change. The second portion of this chapter describes the optimization process that is undertaken to determine an optimum cover thickness. This also includes considering Type 1 (all) material and conditions without a till layer to offer a flexible site recommendation that will maintain the PAG material frozen after 100 years.

Chapter 5 summarizes the conclusions found during the sensitivity analyses as well as the thickness optimization of the soil cover. The recommendations for proposed field testing and future research considerations follow.

Appendix A includes model input data for simulations outlined in this research. This appendix will also serve as a quick guide to recreate the modelling environment described in this research.

2 Literature Review

2.1 Mining and Waste Rock Storage Areas (WRSAs)

2.1.1 Mining Definitions

In mining operations there are a few key terms used to describe the material in the ground. Relevant definitions below are based on the descriptions provided by Harman and Mutmansky (2002), Younger et al. (2002), and Vick (1990).

Mineral A naturally occurring, inorganic, solid substance (element or compound) with defined characteristic chemical composition, crystalline structure, and physical properties. A *mineral deposit* is a mineralized mass that may be economically viable but has not yet been proven.

Rock A naturally formed aggregate (mix) of one or more mineral particles. Rock is relatively homogeneous at large scale.

Ore A mineral deposit that is profitable after it has been removed from the ground, processed, and delivered to the customer. Ore is a mixture of both ore minerals and gangue. An *ore deposit (orebody)* is a mineral deposit which has shown to be profitable.

Gangue Minerals within an ore deposit which have no economic value. Depending on geology, the gangue material can be separated from the valuable ore minerals either during excavation or in the processing plant.

Overburden The rock or soil which overlies a mineral deposit. Depending on a mining configuration, the volume ratio of overburden to ore can be extremely large (open pit mining) or small (underground mining).

Host Rock Also called country rock. This is the non-mineralized bedrock or rock enclosing (“hosting”) an orebody. It often has different chemical and physical properties than the orebody as they tend to be formed from different geological processes.

Waste Waste represents all material that is removed from the ground that is non profitable. This will encompass overburden, host rock, and gangue material.

Tailings Tailings is another form of waste material, but it is often separated from the mine waste streams described above. This material is the finely ground mill or mineral processing waste that is generated during the extraction of the profitable ore. Tailing material often exits the processing stream in slurry form and require dewatering and/or containment.

2.1.2 Waste Rock Storage Areas (WRSAs)

Waste rock is often grouped together and called a waste rock pile, a waste rock dump, or a waste rock storage area (WRSA). As most mining operations have different types of waste material, they may form separate WRSAs if their properties require different geochemical or geotechnical considerations. Some waste material may be suitable for construction purposes. When waste material is placed in a pile with the intention to rehandle and use elsewhere it is called a stockpile.

WRSAs have many different final design configurations which usually depend on the natural topography of a site. The five main structures are outlined in Figure 2-1 (Hawley and Cunning 2017). The structures consist of one or a combination of these designs. In addition to the advantageous use of natural topography, the location and configuration of a WRSA will consider factors such as structural stability, haul distances, future resource development, watersheds, and potential environmental impacts. A view of a typical active WRSA will show a complex structure with ramps, multilevel benches, contrasting material types, and monitoring stations.

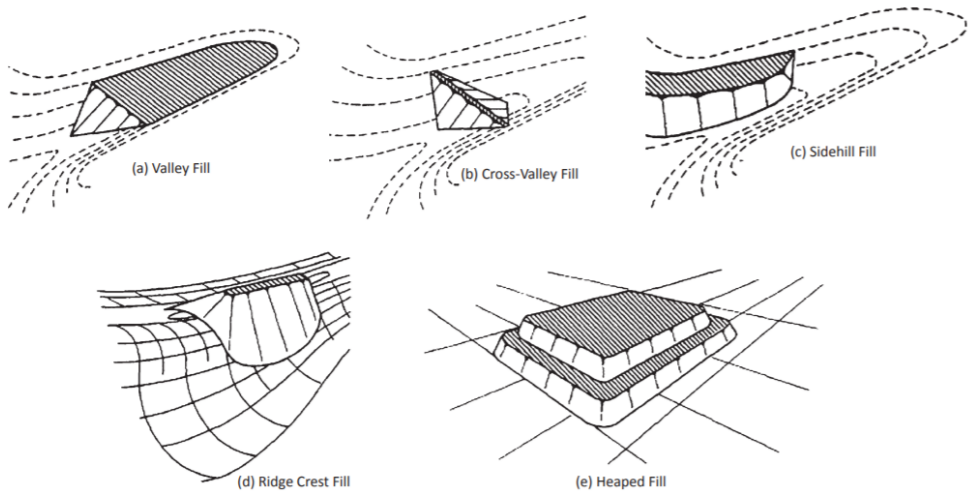

Figure 2-1: WRSA structure examples
Reproduced from Hawley and Cunning (2017) with permission from CSIRO Publishing.

The size of WRSAs may vary drastically based on their material mining types. In general, underground mining produces very little waste for two reasons. First, underground mining only

requires a small volume of overburden material to be removed (relative to surface mining) in order to access the orebody through the excavation of mine shafts and horizontal adits. In addition, underground mines will often back-fill waste into mined out voids for both storage and stability purposes. Underground mines rarely produce a WRSA on the surface (Hartman and Mutmansky 2002). In contrast, open pit (surface) mines require a large amount of overburden excavation to reach the orebody and therefore they produce large WRSAs. These WRSAs can be the size of small mountains which can generate significant challenges for both geochemical and geotechnical stability. In fact, in terms of volume and mass, WRSAs are considered some of the largest man-made structures on earth (Hawley and Cunning 2017). As the mining industry continues to expand and excavate more material to retrieve deeper, more valuable ore, WRSAs have increased in size over the years. For example, a WRSA at Antamina Mine, located in the mountainous Andes of Peru, towers at an overall height of 500 m from crest to toe and contains more than 1 billion tonnes of material over a footprint of 240 ha (Hawley and Cunning 2017). Although this WRSA in Peru is much larger than the average structure, most are in the 30 – 100 m height range (Blowes et al. 2014). In addition to their significant heights, these structures are also horizontally expansive at widths of hundreds of meters up to a few kilometers resulting in volumes in the millions of cubic meters of material (Lu 2001).

The risks associated with WRSAs are primarily related to geotechnical (physical) or chemical stability. Often these two risks may counter each other as described by Wilson (2008). A saturated WRSA may be considered geochemically stable as it prevents the inflow of oxygen to the potentially acid-generating (PAG) material whereas geotechnically this is considered hazardous. The pore pressures of a saturated WRSA may lead to static liquefaction – a failure mode that is destructive, sudden, and therefore difficult to prepare for. On the contrary, a free-draining structure is likely to be structurally sound, but the free infiltration of water and oxygen produces the ideal environment for the generation of acid rock drainage (ARD, defined in Section 2.3). While these issues appear difficult to manage together, a fine balance of solutions can be found, particularly if a WRSA is managed proactively.

Unfortunately, many waste rock piles are abandoned after their operating life without having reached an acceptable level of chemical and physical stability. This issue tends to lead to much costlier alternatives during reclamation and reminds us that planning and incorporating a final reclamation plan into everyday operations is the best (if only) way to operate.

2.2 Permafrost and Cold Regions

2.2.1 General Definitions

Cold regions have been defined based on a number of variables such as air temperature, snow depth, ice cover on lakes, and freeze depth (Andersland and Ladanyi 2004). Many of these definitions incorporate the use of an isotherm – a line on a map connecting points that have the same temperature. This provides a spatial boundary based on temperature. Historically, the southern limit of the cold regions of the Northern Hemisphere were defined using the 0°C mean air temperature isotherm (Bates and Bilello 1966). An arbitrarily chosen frost penetration depth (300 mm), just once in ten years, is another generally accepted criteria for this cold region limit (Andersland and Ladanyi 2004).

Cold regions can be further divided based on the presence or absence of permafrost. Defining the term permafrost, classifying permafrost terrain, and mapping the boundary of a permafrost region can be challenging as it relies on a condition (temperature) rather than a substance (Heginbottom 2002). In addition to the annual cyclic nature of temperatures, the annual temperature increases due to climate change are shown to be amplified in cold regions, with nearly twice the temperature increase in Canada's arctic as compared to the world average (Bush and Lemmen 2019). Furthermore, there are separate terms such as "cold regions", "permafrost", "perennially frozen ground", and "seasonally frozen ground" which have historically had changing definitions. Much of these variations stemmed from the earliest days of cold region research where several countries (such as Russia (formerly USSR), China, U.S (Alaska), and Canada) established their own baseline of terminology and definitions independently. The International Permafrost Association (IPA) has established a working glossary of terms to unite these differences (IPA 1998).

Perennially frozen ground, or permafrost, is one of two classifications of frozen ground. Permafrost is defined as any ground that remains at or below freezing continuously for at least two consecutive years (Brown and Péwé 1973, Davis 2001, Andersland and Ladanyi 2004, Smith 2011). The other frozen ground type is seasonally frozen ground which is described by Brigham and Nelson (2003) as material which freezes and thaws annually.

Further definitions are assigned to the various zones that exist within a cold region – continuous, discontinuous, sporadic, and mountain permafrost. Discontinuous permafrost zones are where permafrost is only found in certain areas beneath the exposed land surface (Andersland and Ladanyi 2004). Mountain permafrost exists as a result of high altitude or a large fluctuation in

topography (IPA 1998, Gruber et al. 2015). It is noted that there is no sharp distinction or boundary between discontinuous and continuous permafrost zones. Further classifications are outlined by the IPA (1998) and Smith and Burgess (2004) in Table 2-1 which take into account their mean annual air temperatures (MAATs). These four zones are reproduced in Figure 2-2 in a permafrost map of Canada (Heginbottom 2002, Smith 2011). About 42% of Canada, almost 4 million km^2, is underlain by permafrost (Brown 1970, MEND1.61.2 1996, Smith and Burgess 2004).

As demonstrated thus far, the definitions and conditions for the term permafrost can vary significantly depending on the source and usage. The term permafrost will be used in the remainder of this document.

Table 2-1: Classifications of permafrost zones by underlying permafrost percent and MAAT As per IPA (1998) and Smith and Burgess (2004)

Zone	Permafrost underlying the landscape	MAAT
Continuous	90 – 100%	<-7.5°C
Discontinuous	50 – 90%	-7.5°C to -1°C
Sporadic	0 – 50%	>-1°C

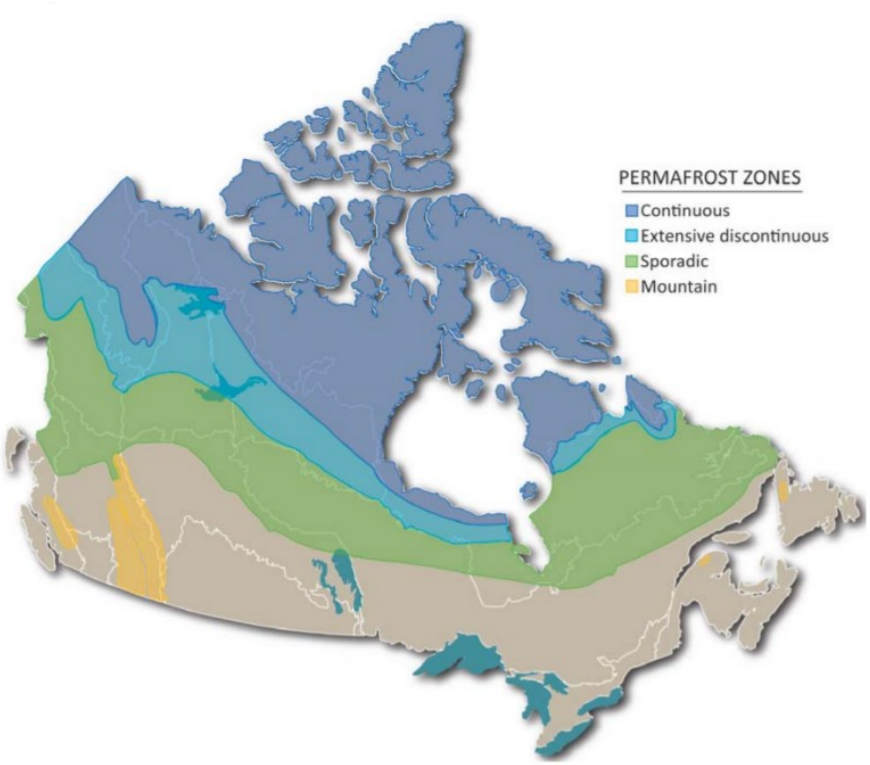

Figure 2-2: Permafrost zones in Canada Reproduced[1] from Smith (2011).

[1] This reproduction is a copy of an official work that is published by the Government of Canada and that the reproduction has not been produced in affiliation with or with the endorsement of the Government of Canada.

Layers of permafrost are built annually due to a negative heat imbalance (Brown 1970), eventually reaching over 700 m thick such as the permafrost located in the Canadian Arctic Archipelago (Smith and Burgess 2004). These thick layers of frozen ice, soil, and rock are built over thousands of years, however at some point an equilibrium is reached with the downward freezing temperatures are balanced with the earth's core temperature, causing a maximum thickness to be reached (Brown 1970). The lower portion of a freezing curve, below the line of zero seasonal changes, demonstrates this gradient as shown in Figure 2-3.

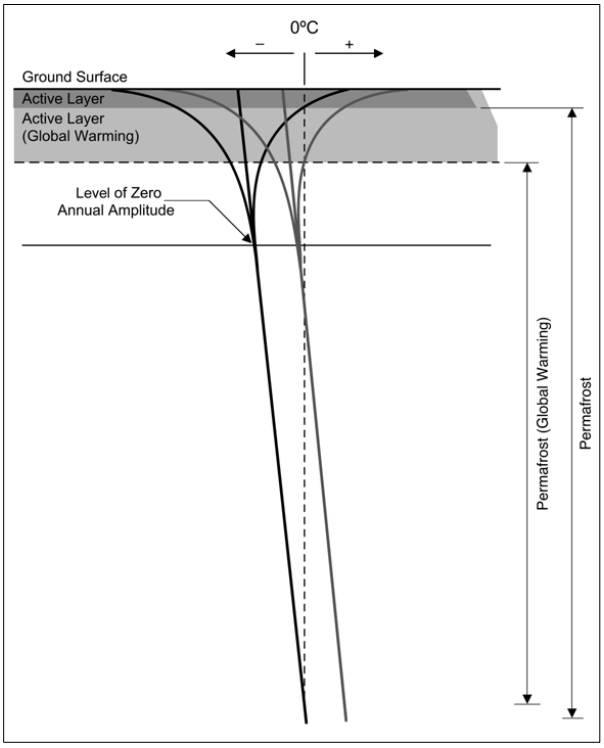

Figure 2-3: Ground temperature profile in a permafrost environment under global warming Reproduced from Brigham and Nelson (2003) with permission.

Temperature is not the only driver of permafrost and ice formation. Brown (1970) explains that although permafrost material contains mostly ice, there is still unfrozen water that may contain impurities or are under pressure which can lower the freezing temperature. Typically, this depends on the mineral, organic, and water contents of the pore fluid (Andersland and Ladanyi 2004). As a result, the frozen and unfrozen portions of pore fluid may need to be considered when conducting relevant permafrost calculations.

2.2.2 Cold Temperature Parameters

General characteristics of a permafrost region include a low MAAT, low mean annual precipitation (LMAP), and little to no vegetation (Wagner 2008). The MAAT can give an indication of the mean annual surface temperature (MAST) trend as they usually only vary by a few degrees. The MAST

is the temperature of the ground measured 1 cm below the surface (Brown 1963). The temperature difference between MAST and MAAT can depend on a number of different factors, a number of which have been empirically expressed by a surface n-factor (Brown 1963, Smith and Burgess 2004). The n-factor is controlled by site-specific conditions such as solar radiation, wind speeds and frequency as well as the ground conditions such as thermal properties, terrain relief, and sub-surface drainage.

The n-factor has two forms: freezing n-factor (n_f) and thawing n-factor (n_t). These particular variables also depend on the thawing indices of both the air and soil. The fluctuation between temperature maximums and minimums in a given season is represented by the freezing or thawing indices, in degree-days. The magnitude of the n-factors represent the intensity of the temperature fluctuations (Andersland and Ladanyi 2004). These temperature fluctuations exist as air freezing and thawing (I_{af} and I_{at}) and soil freezing and thawing (I_{sf} and I_{st}) indices. The relationships between these variables are defined in Equations 2-1 and 2-2.

$$n_f = \frac{I_{sf}}{I_{af}} \quad \textbf{2-1}$$

$$n_t = \frac{I_{st}}{I_{at}} \quad \textbf{2-2}$$

Temperatures at and below the ground surface will fluctuate annually with seasonal changes. The maximum and minimum temperatures seen during the year at each depth will form the annual ground-temperature envelope (Smith and Burgess 2004). The difference between the maximum and minimum temperature is also called the annual temperature swing (ATS). The ATS can be defined at any depth. It is largest at the surface and it approaches zero as the profile increases with depth as seen in Figure 2-3 (Andersland and Ladanyi 2004). The active layer is the thaw depth, which includes the upper portion of the ground that freezes in the winter and thaws in the summer (Brown 1970). Being tied closely with surface temperatures, the active layer may increase with climate warming over the years, again denoted in Figure 2-3 (Davis 2001). The effects of climate change on permafrost are outlined in Section 2.11. The active layer may vary from just a few centimeters to a few meters, increasing as the permafrost approaches the southern (Northern Hemisphere) outskirts of the region (Wagner 2008).

2.3 Acid Rock Drainage (ARD)

2.3.1 Introduction to ARD

ARD is an environmental issue that can occur in any type of rock which contains sulfide minerals. It is one of the most common and problematic type of runoff to exist within the mining industry (Benzaazoua et al. 2017). ARD can be expected when sulfide minerals in rocks become exposed to air and water, allowing for the chemical oxidation of sulfides. The most common sulfide bearing mineral associated with waste rock is pyrite (FeS_2). The full chemistry describing the production of ARD, specifically pyrite oxidation, is complex (Jaynes et al. 1984) and involves not just chemical, but also biological and electrochemical reactions (Benzaazoua et al. 2017). A simplified general chemical equation is provided by Nordstrom and Alpers (1999) in Equation 2-3.

$$FeS_{2(s)} + \frac{7}{2}O_{2(g)} + H_2O_{(l)} \rightarrow Fe^{2+}_{(aq)} + 2SO_4{}^{2-}_{(aq)} + 2H^{+}_{(aq)} \quad \textbf{2-3}$$

The stoichiometry presented in Equation 2-3 demonstrates how one mole of pyrite (FeS_2) reacts with oxygen and water to produce ferrous iron, sulfate, and hydrogen. In other terms, for each mole of pyrite and three and a half moles of oxygen, there are two moles of acid being produced (Jaynes et al. 1984). The pH of the effluent is decreased through this process. While this process will occur naturally due to erosional weathering processes, mining operations will dramatically increase the opportunity and surface area of exposed material thus accelerating the production of ARD.

Some mine waste material which has sulfides can also contain sufficient neutralizing carbonate minerals which will buffer the pH and reduce the impact. Mine waste rock or tailings is often tested in a variety of ways to determine their acid-producing potential which accounts for this buffer capacity. A number of static and kinetic tests are listed in detail in MEND1.20.1 (2009). After material has been adequately tested it can be broken out into either PAG or non acid-generating (NAG) material.

Extensive amounts of research have been conducted on ARD generation from tailings (MEND1.61.2 1996, MEND1.61.4 2004, Coulombe et al. 2012, Pham and Sego 2013) and waste rock (Adu-Wusu and Yanful 2006, 2007, Amos et al. 2015, Elghali et al. 2018, 2019). The two waste streams are different and therefore often require separate considerations. Vick (1990) outlines the key factors of sulfide oxidation within tailings. When ARD is associated with tailings it is often due to the existence of a common sulfide mineral, pyrite (FeS_2), in the ore. The mineral

extraction circuit usually rejects pyrite during the concentration step which then produces tailings (often in slurry) which has an elevated concentration of pyrite. During active deposition a tailings impoundment is usually saturated, and the phreatic surface (water level) is often carefully controlled for structural stability. The saturated tailings prevent oxygen from reacting with the sulfides and therefore limits the production of ARD. However, once an impoundment is full and deposition has ceased, the phreatic surface will drop and the sulfides are then exposed to oxygen. Options for the management of tailings with the potential for acid generation may be to keep the impoundment saturated, completely submerged below a water cap, and/or to collect and treat the effluent. Both options require treatment in perpetuity. In contrast, waste rock is often stored in WRSAs which are often free draining. Waste rock material is also much coarser than tailings in general, however, the construction methods of WRSAs can produce fine and coarse layers and the structure is rarely homogeneous. These interbedded layers are caused by the range of particle sizes, material placement methods, and trafficked surfaces. Fine-grained material can maintain saturation even while the remainder of the structure is considered coarse grained and free draining. The preferential pathways that exist in the fine layers of waste rock piles and their contribution to sulfide oxidation are described by a number of authors including Herasymuik (1995), Stockwell et al. (2006), Azam et al. (2007), Neuner (2009), Smith et al. (2013a), Amos et al. (2015), Barsi (2017), and Barsi et al. (2019). The increased heterogeneity of waste rock piles and their unsaturated conditions provide separate challenges than the saturated and (relatively) more homogeneous tailings. Mitigation of ARD for waste rock is described in a later section.

2.3.2 Microbial Activity and Cold Temperatures

The ARD reaction may also be catalyzed by certain types of microbial bacteria. For example, the chemoautotrophic *Thiobacillus ferrooxidans* may act as a catalyst by using released energy from pyrite oxidation (Jaynes et al. 1984, Bailey et al. 2016). This can cause the acceleration of ARD (Nordstrom and Southam 1997, Blowes et al. 2014).

Cold temperatures are beneficial in controlling the microorganisms that exist in mine waste piles. As summarized by Godwaldt et al. (2000), cold temperatures result in a slowing of the physiological processes (such as the catalyzing effect) of microorganisms. This is due to the cell membranes of the bacteria losing their fluidity and resulting in decreased activation energies. In addition, the freezing of the PAG material restricts the entrance of the percolating pore water which could introduce solutes to the oxidants within the waste rock (Langman et al. 2017). It should be noted that these temperatures do not completely eliminate microbial activity in waste

rock. At even extremely low temperatures there may still be unfrozen porewater which allows bacteria to survive in normally impossible temperatures (Wagner 2008).

Wagner (2008) notes that in a permafrost environment the variability of the local climate (directly affecting MAAT and LMAP) in combination with soil heterogeneity and varied salt/organic contents supports the development of microcolonies of microorganisms. This adds to the uncertainty of microorganisms within a frozen structure, but overall conservative assumptions are used, anticipating the presence of microcolonies throughout a waste rock pile.

2.3.3 ARD Mitigation

Mitigation strategies of ARD consider the three reactants in the ARD equation – sulfides, water, and oxygen. The removal of any of these parts would mitigate the issue by preventing the required chemical reaction. According to Robertson (1987), there are three approaches to mitigate ARD from waste rock piles:

1. Control of Acid Generation
2. Control of Acid Migration
3. Collection and Treatment of Acidic Drainage

Risk analysis would show that the best option is to prevent the hazard at all, followed by managing or mitigating the hazard, and lastly by remediating the damages caused by the hazard. Therefore, it is best practice to prevent the generation of acid to begin with. In the control of acid production, the removal of acid-generating material is not a feasible nor a technically sound option (Robertson 1987). Robertson (1987) includes water infiltration as also being impractical to prevent, however, cold temperatures can greatly improve the feasibility of this prevention tactic. The third component would be to control the oxygen infiltration.

Oxygen infiltration may be reduced with the use of a saturated material layer incorporated into a soil cover system. Further descriptions of these soil covers are outlined in Section 2.6. Research of the geochemistry of a Covered test pile by Langman et al. (2017) showed that a soil cover which contained a saturated material layer acted both as a thermal insulator and reduced the temperature fluctuations in the PAG material, resulting in the reduction of ARD from the Covered pile.

2.3.4 ARD in Permafrost Regions

Waste rock piles situated in permafrost regions may benefit from cold temperatures in the mitigation of ARD. In addition to slowing the microbial activity (catalysts), low temperatures

interrupt the flow of water through a waste rock pile when it freezes. These low temperatures (below 5°C) have been shown in laboratory testing to slow down (but not completely halt) the production of acid (MEND1.61.2 1996).

A literature review conducted by MEND1.61.2 (1996) of ARD within permafrost environments was produced as a baseline review of the state of practice at that time. At the time of reporting, mines with ARD issues situated within the permafrost region were predominately associated with tailings, with much fewer occurrences of waste rock. Literature from mostly tailings and natural incidences of ARD were reviewed. Following the review, the report does emphasize that a permafrost environment alone can not eliminate ARD generation although it may show signs of reducing the impacts. The author points to the material within the active layer which is susceptible to acid generation during the thaw months and as a result it is recommended to prevent the active layer from penetrating into the PAG material.

Case studies of ARD mitigation in permafrost environments can be seen in Section 2.10 which include the work conducted at Raglan Mine, Lupin Mine, and Nanisivik Mine.

2.4 Fluid Flow in Soils and General Definitions of Soil Mechanics

2.4.1 Definitions

This research focuses on two branches of physics. The first is fluid flow within a porous medium (specifically the flow of air through the interconnected voids of soil). The study of the flow of a fluid through soil is an important aspect of soil mechanics and particularly this research. While classic soil mechanics focused on the flow of water, the past few decades has seen the focus shift to defining the flow of fluids (both air and water) in a soil (commonly described as unsaturated soil mechanics). The fluid flow for this research will assume any moisture within a volume of soil remains stationary and the only fluid transport is air. A detailed explanation of this assumption is presented in Section 3.3.

Preliminary definitions of key soil mechanics relationships are required before proceeding. A schematic showing mass and volumes of frozen and unfrozen soil structures is presented in Figure 2-4. This figure assumes that there is no unfrozen water in frozen conditions. The following definitions were provided from Holtz et al. (2011). Porosity (η) is the ratio of the volume of voids (V_v) to the total volume (V_t) and the degree of saturation (S_r) is the volume of water (V_w) over the volume of voids as seen in Equations 2-4 and 2-5, respectively. The gravimetric moisture content (ω_g) of a material is the mass of water (M_w) over the mass of solids (M_s) whereas the volumetric

moisture content (ω_v) of a material is defined as the volume of water over the total volume as shown in Equations 2-6 and 2-7, respectively.

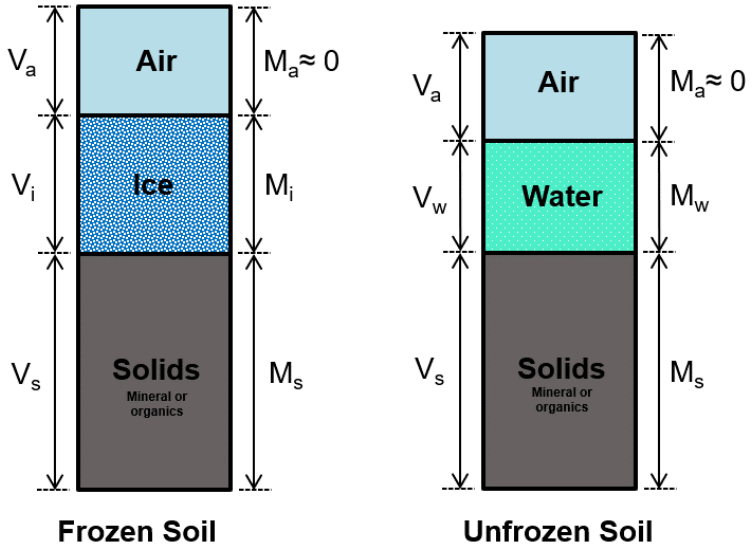

Figure 2-4: Frozen and unfrozen soil-volume diagrams per on Andersland and Ladanyi (2004)

$$\eta = \frac{V_v}{V_t} \quad \textbf{2-4}$$

$$S_r = \frac{V_w}{V_v} \quad \textbf{2-5}$$

$$\omega_g = \frac{M_w}{M_s} \quad \textbf{2-6}$$

$$\omega_v = \frac{V_w}{V_v} \quad \textbf{2-7}$$

A fluid (water, air, or a mixture both) can flow through a porous medium (soil particles) through interconnected pores (voids). The study of the flow of a fluid through soil is an important aspect of soil mechanics and particularly this research.

Holtz et al. (2011) describe Bernoulli's Equation which defines the relationship of pressure (u), velocity (v), and elevation (Z) to the total head (h, energy) of a fluid (Equation 2-8). The total head of a fluid at any given point can be defined by this equation. The hydraulic gradient (i) is described as the ratio of the change in head (Δh) over the distance between two points (L) as presented in Equation 2-9. A further description and analysis of this equation is provided in detail in Holtz et al. (2011).

$$h = \frac{u}{\gamma} + \frac{v^2}{2g} + Z \quad \textbf{2-8}$$

$$i = \frac{\Delta h}{L} \qquad \text{2-9}$$

2.4.2 Darcy's Law

Darcy's Law is an empirical equation for the discharge velocity (or "Darcy" velocity, v_d) of water through a saturated soil as presented in Equation 2-10 below (Holtz et al. 2011). The Darcy velocity is dependent on the hydraulic conductivity (k) and the hydraulic gradient of a porous media system. The fluid flow (q) through a porous media system is then demonstrated in Equation 2-11 as a product of Darcy velocity and the cross-sectional area (A). In addition to Darcy velocity, there is a separate term called the seepage velocity (v_s). The seepage velocity is dependent on the path of a water droplet which is neither linear nor consistent throughout a porous medium. As a result, the seepage velocity is always greater than Darcy velocity. Holtz et al. (2011) emphasize that these two variables are defined as an average through the system and each of these velocities will have an instantaneous and unique value at a given location, depending on the local porous makeup. The relationship between the seepage velocity, Darcy velocity, and porosity is displayed in Equation 2-12 (Holtz et al. 2011). A graphic representation of these variables is presented in Figure 2-5.

$$v_d = ki \qquad \text{2-10}$$

$$q = v_d A \qquad \text{2-11}$$

$$v_s = \frac{v_d}{\eta} \qquad \text{2-12}$$

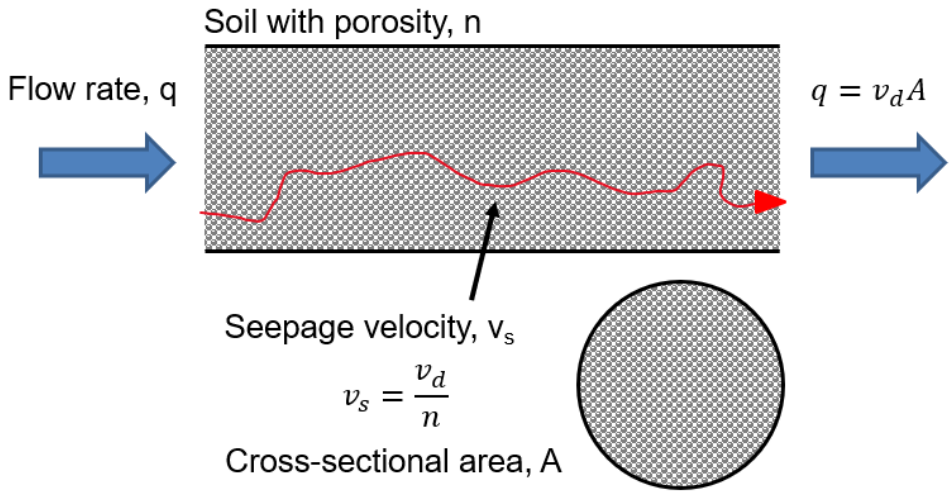

Figure 2-5: Flow rate, seepage velocity, and discharge velocity through a soil volume (Adapted from Das (2013))

The hydraulic conductivity of a soil is dependent on both properties of the fluid (permeant) and the porous media (soil). This includes the density of the fluid (ρ_f), absolute viscosity of the fluid (μ_f), and the coefficient of permeability (K) as shown in Equation 2-13. In addition, the dynamic viscosity of a fluid (v_f) is shown in Equation 2-14 as the ratio of the absolute viscosity over the density.

$$k = \frac{\rho_f g}{\mu_f} K \quad \textbf{2-13}$$

$$v_f = \frac{\mu_f}{\rho_f} \quad \textbf{2-14}$$

2.5 Heat Flow in Soils

The second branch of physics in this research is heat transfer (flow) through soils. Farouki (1981) provides a baseline understanding of these concepts and the following is a summary presenting topics which are integral to the understanding and development of this thesis. Further details may be found in the original source which provides an excellent in-depth analysis of the material presented.

The thermal properties of soils tend to be complicated to calculate or measure due to their dynamic nature and variability. Key properties include temperature, soil composition, and soil structure. Considering climatic temperature fluctuations (both daily and seasonal) and the general heterogeneous nature of soils there are many considerations to the heat flow problem.

2.5.1 Definitions

The following heat transfer definitions are summarized from Farouki (1981) with the cold temperature aspects provided by Andersland and Ladanyi (2004). This section will aim to provide a baseline of the terms and formulae that impact the heat transfer in soils, particularly those which undergo freeze-thaw.

2.5.1.1 Thermal Conductivity

Heat transfer through conduction will be introduced briefly and discussed in further detail in a later Section. Conduction depends on kinetic energy from a warm particle transferring to a colder particle (Andersland and Ladanyi 2004). In a given volume of soil, the thermal conductivity (λ) represents how much heat flow over a unit of time (Q) will pass through a cross-sectional area over a distance given a temperature gradient ($T_2 - T_1$) as outlined in equation 2-15 and demonstrated in Figure 2-6.

$$\lambda = \frac{Q * L}{A(T_2 - T_1)} \qquad \text{2-15}$$

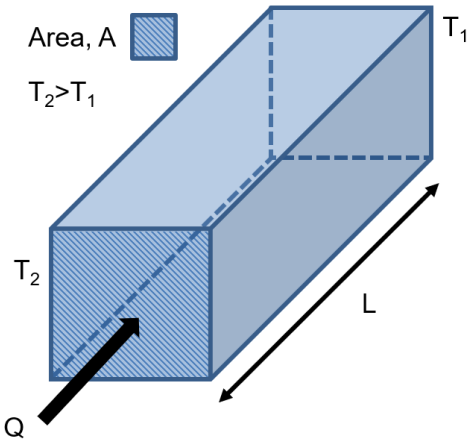

Figure 2-6: Conductive heat transfer through a volume of soil, adapted from Farouki (1981)

Tables of common materials and their respective thermal conductivities can be found in many source materials, including Farouki (1981) and Andersland and Ladanyi (2004). These values can range significantly for different materials. For example, a volume of dry sand may consist of two materials air (λ = 0.026 W/(m·K)) and quartz (λ = 8.4 W/(m·K)). The thermal conductivity of a purely conductive soil volume will be influenced by it's constituent's thermal conductivities like air (λ_a), solid (λ_s), water (λ_w), and ice (λ_i) and their volumetric proportions (Andersland and Ladanyi 2004).

Furthermore, while heat transfer primarily occurs through conduction, there are other mechanisms such as convection and radiation which may occur in soil (Farouki 1981). These terms will be described in later sections. When there are multiple thermal heat transfer mechanisms the term *thermal conductivity* and its definition (Equation 2-15) still holds but it may be called *effective* or *bulk thermal conductivity*.

Soil temperatures will also impact thermal conductivity in fully or partially saturated soils. This is because frozen water (ice) and unfrozen water have different thermal conductivities (λ_i = 0.56 W/(m·K) and λ_w = 2.21 W/(m·K), respectively). Freeze and thawing conditions may also change the composition and structure of a soil and increase the porosity as water particles increase in volume as they freeze (Andersland and Ladanyi 2004). For this reason, a material which is undergoing freeze and thaw will often have both a frozen and unfrozen thermal conductivity, denoted as λ_{fr} and λ_{uf}, respectively.

In a system which is not in a steady state, a measured effective thermal conductivity is an instantaneous average of the condition between the two points. Often boundary conditions can impact the moisture distribution in a soil and therefore the thermal conductivity would not be expected to be the same at every point (Farouki 1981).

To summarize, the effective thermal conductivity of a soil may vary significantly depending on temperature (frozen/unfrozen), composition (material densities, respective thermal conductivities), and structure (porosity, texture). A few methods have been established to empirically calculate the thermal conductivity based on known soil parameters.

Andersland and Ladanyi (2004) summarize the Johansen (1975) method for calculating the unfrozen thermal conductivity for mineral soils. This method includes the definition of the unitless Kersten number (K_e) which incorporates findings from Kersten (1949). The Kersten number is defined in Equation 2-16 and correlates to the unfrozen thermal conductivity of a soil in comparison to its dry and saturated conditions condition (λ_{dry} and λ_{sat}, respectively). In this formula, a dry material will yield a Kersten number of zero and a saturated material will yield a Kersten number of 1 (Johansen 1975). The Kersten number for an unfrozen material in between dry and saturated conditions is approximated empirically according to its soil texture (coarse or fine) and degree of saturation as shown in Equations 2-17 and 2-18, respectively.

$$K_e = \frac{\lambda_{uf} - \lambda_{dry}}{\lambda_{sat} - \lambda_{dry}} \quad \textbf{2-16}$$

Unfrozen Coarse-Grained Soil, S_r >0.05 $$K_e = 0.7 \log S_r + 1.0 \quad \textbf{2-17}$$

Unfrozen Fine-Grained Soil, S_r >0.10 $$K_e = \log S_r + 1.0 \quad \textbf{2-18}$$

The Johansen (1975) method is generally considered the best option for determining the thermal conductivity of a material given the large range of soil types and degrees of saturation that it covers (Andersland and Ladanyi 2004). However, as with many empirically derived models, this method does have a few limitations. As outlined by Côté and Konrad (2005) the Johansen (1975) method did not account for the volume change effects of porosity and saturation when water turns to ice (not necessarily a concern in an open system). This was not considered in the calculation for the Kersten number of a coarse-grained soil (Equation 2-17) since the formula is tailored to medium and fine-grained sandy soils and therefore this effect is negligible. However, when this method is applied to a coarser grained material (which has a much larger particle size distribution and typically a lower density) the calculated thermal conductivities can be inaccurate (Côté and Konrad 2005). In addition, while the Johansen (1975) method provides a way of incorporating

quartz content of a mineral, the remaining impact of other minerals and their respective thermal conductivities were not considered. As a result, Côté and Konrad (2005) expanded the Johansen (1975) method of normalized thermal conductivities to account for these disparities. While the focus of this method was primarily on a common road building layer called “base-coarse”, it may be applied to some mine waste coarse material as well.

The process identified by Côté and Konrad (2005) begins with the calculation of the dry and saturated thermal conductivities. The dry thermal conductivity is defined in Equation 2-19 which uses a modified form of a geometric mean and includes fitting parameters from experimental data. The saturated thermal conductivity is calculated in both unfrozen and frozen terms in Equations 2-20 and 2-21, respectively. These formulae incorporate the thermal conductivities of the solid material, air, and water/ice along with the porosity of the material. The solid thermal conductivity of a material can be calculated using the geometric mean if the mineralogy is known, however, there is also a table of typical material values provided by the authors.

$$\lambda_{dry} = \lambda_s^{(1-\eta)^{0.59}} \lambda_a^{\eta^{0.73}} \quad \textbf{2-19}$$

Unfrozen $$\lambda_{sat} = \lambda_s{}^{1-\eta} \lambda_w{}^{\eta} \quad \textbf{2-20}$$

Frozen $$\lambda_{sat} = \lambda_s{}^{1-\eta} \lambda_i{}^{\eta} \quad \textbf{2-21}$$

The normalized thermal conductivity (λ_r) is then defined empirically according to the degree of saturation of the material with separate values for both unfrozen (Equation 2-22) and frozen (Equation 2-23) cases. Finally, Equation 2-24 calculates the thermal conductivity using Equations 2-19, 2-20, and 2-22 or Equations 2-19, 2-21, and 2-23 for unfrozen and frozen conditions, respectively.

Unfrozen $$\lambda_r = \frac{4.7 S_r}{1 + 3.7 S_r} \quad \textbf{2-22}$$

Frozen $$\lambda_r = \frac{1.8 S_r}{1 + 0.8 S_r} \quad \textbf{2-23}$$

$$\lambda = (\lambda_{sat} - \lambda_{dry}) \lambda_r + \lambda_{dry} \quad \textbf{2-24}$$

2.5.1.2 Heat Capacity and Specific Heat

Andersland and Ladanyi (2004) explain that the thermal conductivity defined in Section 2.5.1.1 assumes a steady state condition. A volume of soil in the field will have a temperature which is changing over time which would indicate that the system is experiencing heat loss or gain. The

temperature changes of a volume of soil due to the heat flow in the system is dependent on a parameter known as specific heat. The (mass) specific heat (C) is defined as the amount of heat required to raise the temperature of a soil sample (1 kg) by one degree. The volumetric equivalent is called the (volumetric) heat capacity (c_v) which is the amount of heat required to raise the temperature of a unit volume by one degree. The calculation for heat capacity is the product of a materials specific heat and density (ρ) as outlined in Equation 2-25 below. The properties of each volume fraction that makes up a soil volume (solid, water, ice, and air) can be multiplied individually by its respective known heat capacity and summed to calculate the overall heat capacity of a soil. This is seen in Equation 2-26 where x_s, x_w, x_i, and x_a are the respective volume fractions in the soil volume, and $c_{v,s}$, $c_{v,w}$, $c_{v,l}$, and $c_{v,a}$ are the respective heat capacities for solids, water, ice, and air. This can also be done with the specific heats (C_s, C_w, C_i, and C_a) and the weight fractions (X_s, X_w, X_i, and X_a) for solids, water, ice, and air, respectively (Equation 2-27).

$$c_v = C\rho \quad \textbf{2-25}$$

$$c_v = c_{v,s}x_s + c_{v,w}x_w + c_{v,i}x_w + c_{v,a}x_a \quad \textbf{2-26}$$

$$C = C_sX_s + C_wX_w + C_iX_i + C_ax_a \quad \textbf{2-27}$$

2.5.1.3 Thermal Diffusivity

In a variable-temperature unsteady state problem a volume of soil has a thermal diffusivity (α) which is defined as the ratio of a soil's thermal conductivity over the heat capacity as seen in Equation 2-28 (Andersland and Ladanyi 2004). The thermal diffusivity measures a soil's ability to transfer thermal energy from high to low.

$$\alpha = \frac{\lambda}{C\rho} = \frac{\lambda}{c_v} \quad \textbf{2-28}$$

As per Andersland and Ladanyi (2004), a high value of thermal diffusivity is indicative of a soil's ability for rapid and considerable changes in temperature. For example, given two identical soils with equal moisture contents, a frozen soil will have a much higher thermal diffusivity than an unfrozen soil. This is because the frozen soil has a both a higher thermal conductivity and a lower specific heat (Equation 2-28) than an unfrozen soil.

2.5.2 Climatic and Geothermal Influences on Soil Temperature

The main driving force for heat transfer within a porous media such as soil is the climatic temperature changes of the air at the surface. As mentioned in Section 2.2.2, the air surface

temperatures oscillate on a daily and seasonal basis (daily superimposed onto the seasonal cycle) and the cyclic nature of the temperature change is transferred within a soil to a given depth (Farouki 1981). The air temperatures make up a part of the soil-surface heat energy balance which couples with the impacts of ground cover to determine the soil temperatures at surface. Ground covers such as vegetation or snow can significantly alter the air-soil temperature relationship. Snow has an extremely low thermal conductivity which effectively acts as an insulator between air and soil (Zhang 2005). In the same way, the amount of vegetation present on the surface will also act as an insulator with many more implications being involved when accounting for roots, moisture content, and evapotranspiration (Walker et al. 2003).

The overall temperature profile of a volume of soil will display a cyclic change during the year which dampens as the profile increases with depth. At a certain depth the cyclic changes due to surface temperatures are no longer visible and will remain constant in equilibrium with the geothermal gradient acting upon the bottom of the soil (Figure 2-3). The geothermal gradient is a result of the heat generation from the earth's core and will increase linearly with depth. Estimates of the geothermal gradient are in the range of +0.3°C to +1.5° per 30 m of depth (Brown 1963, Bear 1972).

2.5.3 Heat Transfer Mechanisms in Soil

There are three mechanisms in which heat is transferred through a soil for unsaturated porous waste rock in a permafrost environment (Pham 2013):

1. Conduction
2. Radiation
3. Convection

2.5.3.1 Conduction

Conduction is the transfer of kinetic and vibrational energy of molecules due to a temperature gradient. This is known as Fourier's Law of Conduction (Jiji 2009). The transfer of energy through conduction moves from high energy to low energy. In a porous media, conduction may be complex due to the multiple phases that may occur in a soil (solid particles, water, air) (Lunardini 1981).

2.5.3.2 Radiation

Radiation energy is energy in the form of electromagnetic waves. By definition, all bodies that have a temperature greater than absolute zero (-273.15°C) emit energy through radiation (Lunardini 1981). In a porous media, the radiative effects are negligible relative to conductive and

convective heat transfer mechanisms except for some coarse, dry materials (Johansen 1975, Côté et al. 2011).

2.5.3.3 Convection

Convection is different than conduction and radiation as it depends on mass transport in order to produce the transfer of energy (Lunardini 1981). As a fluid increases in temperature its volume increases (thus decreasing its density). This warm fluid will rise due to its decreased density and any cold fluid above would sink relative to the warm fluid. The process of this movement is called convection (Lunardini 1981).

In a porous medium such as soil heat transfer convection can be either forced or natural. A forced convection system may involve an external implement which operates either mechanically (pump, fan, or compressor) or naturally (wind or pressure variations) to initiate a cyclic fluid flow (Nield and Bejan 2006, Pham 2013). This differs from natural convection, which instead relies on the driving force of the density variation of a fluid (via temperature or pressure). The key difference here is that the fluid flow in a forced system is driven from a force that is independent to the temperature or pressure effects (Nield and Bejan 2006).

2.5.4 Natural Convection in Porous Media

Natural convection may also be known as thermogravitational or buoyancy-driven convection (Getling 1998). The earliest and base case of buoyancy-driven natural convection is a horizontally infinite layer of a fluid heated from below, which is commonly denoted as the Rayleigh-Bénard problem (Rayleigh 1916, Getling 1998). This problem is dependent on the Oberbeck-Boussinesq approximation in which a fluid is assumed to be incompressible and therefore allows density to form a linear correlation with temperature. As such, a fluid's density only is referenced when it is acted on (multiplied) by gravitational acceleration (g) (Joseph 1976, Getling 1998, Nield and Bejan 2006).

When the Rayleigh-Bérnard problem is applied to a porous media it becomes the Horton-Rogers-Lapwood problem as shown in Figure 2-7 (Horton and Rogers 1945, Lapwood 1948, Nield and Bejan 2006). This situation tends to appear in the field with cold climatic temperatures at the top of a layer of a material and warmer temperatures at the base of the layer (Pham 2013). In the right conditions, a buoyancy-induced convection cell can occur which pulls heat up and out of a porous medium such as a waste rock pile in the winter months without reinjecting the temperatures during the warmer summer months.

2.5.4.1 Rayleigh Number

A horizontally infinite layer heated from below does not immediately induce natural convection. There are several conditions which must be satisfied before the convection cells will form. The Rayleigh-Darcy number, usually simplified to Rayleigh number (Ra), is a dimensionless value used as a threshold to determine the occurrence of natural convection (Nield and Bejan 2006). Through the assumption of valid Darcy's law, Oberbeck-Boussinesq approximation, and additional standard assumptions, Nield and Bejan (2006) provide the formula for the Rayleigh number in a porous media (Equation 2-29). The Oberbeck-Boussinesq approximation is used to demonstrate how fluid density changes with temperature. The full problem is demonstrated in Nield and Bejan (2006). As seen in Equation 2-29, the Rayleigh value depends on system variables (thickness of the convection layer (H) and the temperature difference between the top and bottom of the convection layer (ΔT)), fluid parameters (density, coefficient of volumetric thermal expansion (β), dynamic viscosity, and heat capacity) and porous medium parameters (permeability and thermal conductivity). The coefficient of thermal expansion is a parameter of a fluid which represents the expansion and contraction as a result of a change in temperature. For gases this can be approximated as 1/T (Nield and Bejan 2006).

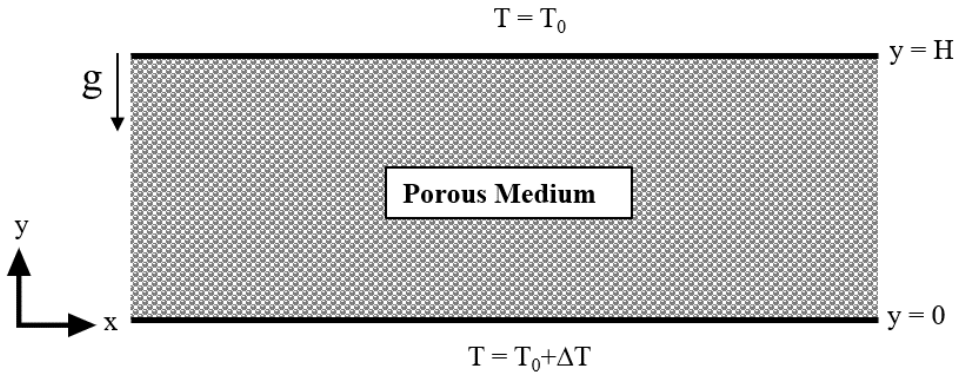

Figure 2-7: Horton-Rogers-Lapwood problem, adapted from Nield and Bejan (2006)

$$Ra = \frac{\rho_f g \beta K H c_v \Delta T}{\nu_f \lambda} \qquad \textbf{2-29}$$

Should the right conditions occur, and a critical Rayleigh value (Ra_c) is reached, the schematic presented in Figure 2-7 would include convection cells. Nield and Bejan (2006) provide a list of various different boundary conditions and their corresponding critical Rayleigh values. The simplest case assumes an impermeable upper and lower boundary condition with conductive heat transfer. This results in a critical Rayleigh value of 39.49 ($4\pi^2$). For a different system such as a waste rock pile, the upper boundary would be assumed to be open to the atmosphere and the

lower boundary can be assumed to be impermeable. These boundaries are still considered conductive. The result for the critical Rayleigh value in with these conditions is 27.10 (Nield and Bejan 2006). Values smaller than this will not induce natural convection and rather will have a system which is dominated by conduction. Further details, analyses, and descriptions can be found in Nield and Bejan (2006).

As the Rayleigh value increases there are some changes to the stability of the convection cell. At an upper threshold of Rayleigh value, the heat transport mechanism is still convective but stable cell regimes may no longer be reached. Different research techniques and numerical modelling have been conducted to determine this upper boundary of Rayleigh values, though these were determined primarily for the case where $Ra_c = 4\pi^2$ (both boundaries impermeable, conductive). Pham (2013) summarizes the research which provides a range of values between 280 to 400. The upper boundary expected for the condition of a waste rock pile (upper boundary permeable, lower boundary impermeable, both conductive) is not included though it is likely to be within the same magnitude of this range.

2.5.5 Latent Heat

Andersland and Ladanyi (2004) describe the latent heat (of water) as the heat energy which is absorbed when ice is melting into liquid or released when liquid is freezing into ice. The term is called the latent heat of fusion during thawing and the latent heat of solidification during freezing. It is the excess energy needed to change the phase of a substance. In fact, given a system with a constant temperature decrease, the temperature of a fluid will hold at 0°C while water begins to transition into ice as all of the energy being transferred to the system goes to the phase change process. The temperature may then continue to decrease below zero once available water has fully transformed into ice.

The definition of the soil (volumetric) latent heat of fusion (L_f) is shown in Equation 2-30. The soil latent heat of fusion depends on the dry density of the soil (ρ_d), the gravimetric water content, and the mass latent heat for water (L' = 333.7 kJ/kg) (Andersland and Ladanyi 2004). This formula assumes that there is no unfrozen water content value.

$$L_f = \rho_d L' \omega_g \qquad \textbf{2-30}$$

To summarize, heat transfer within a porous media is dominated by external processes (intentional, climatic, or geothermal heat fluctuations) which can impact the moisture content and phase (frozen versus unfrozen) of a soil and therefore impact the resulting thermal conductivity.

To further complicate the matter, a temperature gradient imparted onto a soil will induce mass transfer (convection) in addition to heat transfer by conduction. Coupled with frozen and unfrozen water contents, and dynamic boundary conditions, the heat and mass transfer problem can be complicated and is well-suited to numerical modelling.

2.6 Soil Cover Systems

A soil cover is an example of an engineered barrier that can be used to prevent the movement of materials of concern either in or out of a potentially contaminated source. These systems are common in the mining industry on both mine waste piles and tailings deposits. In fact, the International Network for Acid Prevention (INAP 2017) states that a soil cover system is an "essential component of modern mine waste management". These systems can be either a single or multilayer system with at least one saturated layer (Pham and Sego 2013). Generally, the purpose of a soil cover system is to meet the end target of reclaiming the area (either mine waste pile or tailings pond) that is both chemically and geotechnically stable, reliable, and sustainable for both the waste and the receiving environment (INAP 2017). In a non-reactive site, a soil cover may simply offer a buffer between the waste and surface to allow for vegetation growth to establish on the final landscape. Reactive waste requires a more involved design. While mine waste structures will tend to have numerous contaminants of concern, a soil cover system is commonly in place to target potential ARD issues. As outlined in Section 2.3, the management of water and oxygen is a vital part of ARD management in chemically reactive mine waste. More specifically, depending on the site, a cover system would be required to either eliminate or reduce any of the following methods of transport:

1. Meteoric water influx
2. Oxygen influx
3. Contaminant seepage

Further purposes of a soil cover are outlined by INAP (2017) and include items such as meeting regulatory requirements, diverting clean water (thus minimizing overall required treatment), and managing the wind and water erosion of a waste material to improve overall geotechnical stability.

A soil cover design would be tailored to each individual site as it requires a clear understanding of the climate and waste and how a particular cover system would fit in the system. INAP (2017) describes 6 soil cover classifications as outlined in Table 2-2. Soil covers will often fall under more than one of these categories depending on the site requirements.

Table 2-2: Cover system design classifications and examples, modified from INAP (2017)

Cover System Classifications	Definition	Examples
Simple protection systems	Simple cover to promote the final design – this can vary depending on stakeholder requirements (vegetation, topography, contamination isolation, dust/erosion control, long term stability of structure)	Reclamation, re-vegetation, isolation, erosion protection
Store-and release systems	Cover can store excess water during percolation events (precipitation or spring run-off), water released through evaporation and transpiration	
Enhanced store-and-release systems	Store-and-release functionality with added layers to further control water (i.e., for root development). Enhanced water diversion. Frozen layers used to decrease suction, not designed for long term frozen conditions.	Lower permeability layer added, capillary break, engineered frozen capillary break diversion (SFCBD)
Barrier-type systems	Incorporation of at least one layer of low hydraulic conductivity to slow ingress of water or oxygen. Frozen layers depend on convective cooling of the frozen layer over time.	Compacted soil (clay, sand-bentonite) permanently frozen layer/permafrost aggradation layer
Barrier-type systems with engineered layers; and	Using an engineered geosynthetic/geomembrane material to achieve substantially reduced net percolation rates. Requires inspection and replacement to maintain design targets over long timespans.	Geosynthetic or geomembrane material (PP, CPE, PVC, LLDPR, HDPE, GCLs, BGMs)
Saturated soil or rock cover systems	Disposal of materials kept under saturated conditions (significantly reduces oxygen availability and therefore potential acid generation). Phreatic surface is maintained within an inert layer.	Saturated inert coarse material or in some cases under a water cap

2.6.1 Air Convective Embankments (ACEs) and Air Convective Covers (ACCs)

Soil cover sites located in permafrost regions have their own unique considerations. Although these projects tend to be more remote and therefore more expensive than a standard soil cover system there are also added benefits to building in these areas. Some soil covers, such as an air convective cover (ACC), are able to take advantage of frozen conditions.

An ACC is a barrier-type cover system employing the use of a permanently frozen layer. The ACC design is based on a similar type of structure called an air convective embankment (ACE). Goering and Kumar (1996) discuss how the concept of the ACE was derived during the construction of northern roadways and embankments (Alaska and Northern China) which were underlain by permafrost. In addition to climate warming conditions, roadway embankments can also alter the temperature of the ground below them as they interrupt the natural energy balance in the area. Since the areas could be susceptible to thawing, a solution was required to ensure the long-term success of these projects. Goering and Kumar (1996) and Pham (2013) summarize

the numerous research projects that were undertaken as the amount of northern infrastructure construction continued to increase. Goering and Kumar (1996) divide the approaches into three categories:

1. Modification of conditions at embankment surface to reduce MAST
2. Removal of heat from the embankment structure during winter
3. Insulation either within or beneath the embankment

While many options had been considered, they were generally found to be too unsafe, ineffective, and costly to be conducted successfully in the challenging northern environment. The ACE design was able to combat these challenges to successfully maintain the embankment in frozen conditions. The structure consists of a highly porous embankment material with low fines which results in a high permeability layer. This is intended to take advantage of the unstable air density stratifications that exist in the winter. Goering and Kumar (1996) describe it as a "one-way heat transfer device, or thermal diode". This pulls the heat from the embankment and underlying foundation and releases it into the surrounding air during the winter without re-injecting the heat back into the embankment during the summer.

A summary of ACE covers and their corresponding research is outlined in Pham (2013). Extensive numerical and experimental studies were performed in China during the construction of the Qinghai-Tibet railway (Yanhu et al. 2018). The method was mostly successful in preventing damage from thawing ice in the discontinuous permafrost zones of Alaska and Northern China.

As explained by Pham (2013), the ACE cover design is adjusted by adding a latent heat layer of low permeability, high moisture content material. This design is called an ACC and is used to prevent heat penetration (the active layer) into PAG material. The added saturated material, or latent heat layer, requires extra energy to thaw and therefore provides added protection to warming temperatures. The ACC design is an artificial cooling technique which is a candidate for ARD mitigation in a permafrost region. The technique of ACCs are known for rapid cooling of waste rock and can remain frozen year-round (Pham and Sego 2013).

2.6.2 Air Convective Cover (ACC) Design Concept

An ACC design to be placed over a reactive waste rock pile would have a latent heat layer (low permeability, high saturation) overlain with an air convection layer (high permeability, low saturation). Both the latent heat and air convection layers would be built from NAG material.

The air convection layer is designed to induce natural air convection during the winter months. Depending on material properties, natural convection is initiated at a given critical Rayleigh value and temperature stratification (Section 2.5.4). Construction activities of waste rock piles and their covers tend to occur during the warm, summer months. During the first winter following construction, the bottom of the convection layer is significantly warmer than the surface temperatures. Given adequate permeability, a convective system will be initiated which will pull warm air up to the surface of the cover (and thereby releasing to the atmosphere). In the same way, the cold temperatures from the surface are pulled downwards toward the latent heat layer. During both winter and summer months the transfer of heat via conduction continues and moves from warm to cold (upwards in the winter, downwards in the summer). As conductive heat transfer is significantly less efficient than convective heat transfer, the amount of warming that does transfer downwards during the summer is negligible compared to the convective transfer during the winter. Similarly, even though conductive heat transfer will pull heat upwards in the winter, the effect is still negligible compared to the convective heat transfer mechanism. This process of driving the cold temperatures down in this way is called permafrost aggradation.

The latent heat layer within the ACC protects against active later penetration into the PAG material below. Since the amount of heat energy required for ice to melt into water is high, the till will stay frozen longer than it would if it was unsaturated. This keeps the underlying PAG material frozen longer. In addition, the frozen structure of the saturated till can also offer the added benefit of reducing oxygen infiltration to the PAG material, acting sometimes as an impermeable barrier, thereby decreasing potential acid generation (Collette 2017, Yi et al. 2021).

2.7 Site Description

2.7.1 Location and Climate

The Diavik Diamond Mine (the Site) is located in the Northwest Territories, Canada, approximately 300 km northeast of the capital city of Yellowknife. Roughly 220 km from the Arctic Circle, the area is just north of the boundary between the widespread discontinuous and continuous permafrost zones which can be seen by comparing Figure 1-1 and Figure 2-2 (Heginbottom et al. 1995, Heginbottom 2002, Tetra Tech Canada Inc. 2017). The mine site is situated on the informally named 20 km^2 East Island within the Lac de Gras (Figure 1-1). This lake is considered ultra-oligotrophic, which means it has low concentrations of nutrients such as nitrogen and phosphorus according to Indigenous Affairs and Northern Development et al. (IAND et al. 1999). This means that even small incremental changes to the pH can cause significant changes to the

lake. As demonstrated in Figure 2-8, the MAAT on-site is found to be -8.9°C according to data collected from Environment Canada (2018) from 1998 to 2015. The active freeze-thaw depth, also considered the active zone, extends 4 m into the ground (Pham 2013).

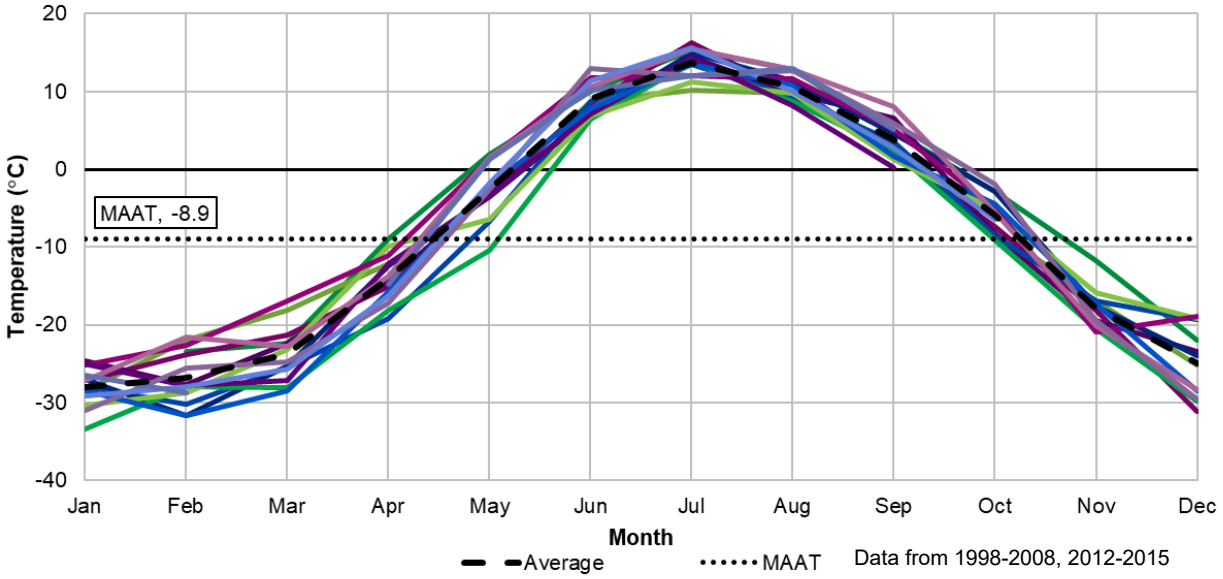

Figure 2-8: Monthly temperature data from Ekati A Weather Station, NWT (With data from Environment Canada (2018))

2.7.2 Mine Site

Worker access to the remote site is by aircraft between the airstrip and Yellowknife year-round with remaining freight delivered over a seasonal winter road according to Diavik Diamond Mines Inc. (DDMI 2018). The mine was initially developed in 2003 with the establishment of the A154 pit which was targeting two kimberlite pipes called A154 North and A154 South. A second pit was developed in 2007 to access the A418 kimberlite pipe. By 2014, both pits had reached their surface mining economical cut off depth and the mining method switched to underground (Shigley et al. 2016). In the same year plans for the development of the A21 pit were made public and by the second quarter of 2018 the A21 pit began ore production. Current mine plans indicate that the A21 pit will continue as a surface mine through to 2022 and the mining of the underground A154 and A418 structures will continue until 2025 (DDMI 2021). The final footprint of the mine site at full development is anticipated to be 12.76 km^2.

The locations of the pits are shown in Figure 2-9. This figure also demonstrates the additional challenge that is involved with the access of the kimberlite pipes. The tops of the pipes are not located on the island therefore the A154 and A418 pits required large dikes to be constructed.

The A21 kimberlite pipe development also followed the same process and the A21 dike allowed for the future pit footprint to be dewatered in 2020.

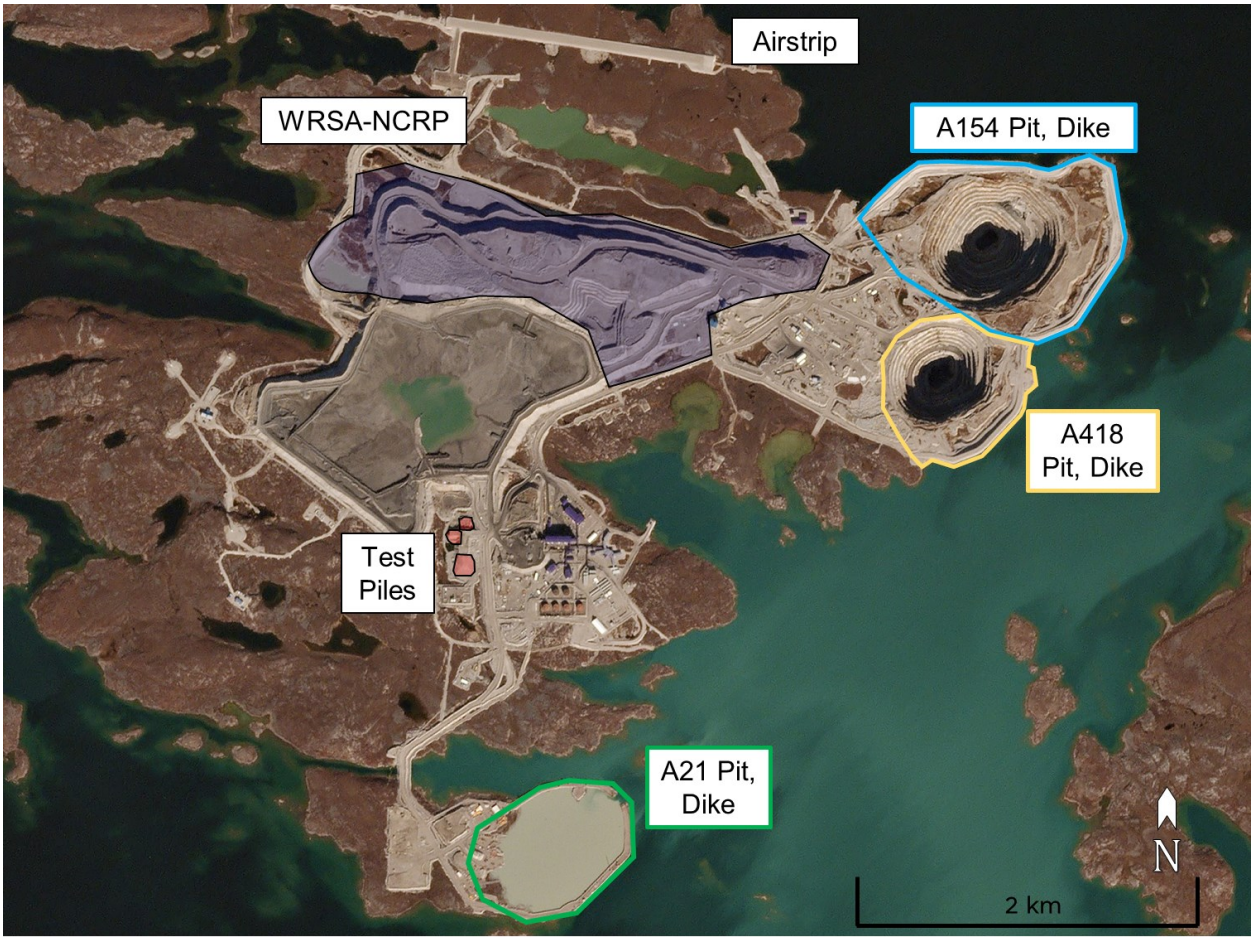

Figure 2-9: Site map, with background image from Planet Gallery (September 21, 2016) (Overlain with data from DDMI (2018))

2.7.3 Geology

The country rock (waste rock) required to be removed to access the kimberlite pipes is generally granitic in nature with small amounts of pegmatite, diabase, and biotite schist lithologies (DDMI 2018). The biotite schist material accounts for approximately 10 to 20% of the rock mass and is PAG. The remaining material is considered non-reactive (NAG) with relatively low sulfur levels. The sulfur content within the biotite schist is also considered low, however, in combination with the low natural alkalinity of the biotite schist the potential for acid generation remains.

A classification of the material overlying the kimberlite pipes (A154 and A418) was described by Golder (2006). The pipes were originally situated under Lac de Gras and were covered with a layer of glacial till (average 4 m) followed by lakebed sediments (average 1.2 m). The glacial till and lakebed sediment are both considered NAG. Golder (2006) describes the lakebed sediments

as a non-plastic silty clay with depths up to 4.6 m. This report also classifies the glacial till as a non-plastic, stony till which has a thickness in the range of 0.4 m to more than 29 m in some locations. It is assumed that the material overlying the newest A21 pipe has similar properties.

2.7.4 Waste Rock Storage Area – North Country Rock Pile (WRSA-NCRP)

This research focuses on the North Country Rock Pile (WRSA-NCRP) which was originally designed as a holding area for the material from the open pit mining of the A154 and A418 kimberlite pipes. The location of the WRSA-NCRP is shown in Figure 2-9.

As the waste rock contains PAG material it is considered a reactive structure and will require a mitigation technique to prevent ARD generation. Figure 2-10 shows areas of the final structure design that will contain PAG material as well as the final footprint of the structure once the WRSA-NCRP structure is resloped according to the closure landform design (Golder 2017). The WRSA-NCRP is expected to contain 184 Mt of waste material at the end of mine life which will span over an area of 3.5 km^2 (DDMI 2018). The different types of waste rock material on-site are separated according to their sulfur content and are stored in separate cells in the WRSA-NCRP. Each cell has an independent seepage collection system. These materials will be defined further in a later section.

According to DDMI (2018) the community outreach during the duration of the mine life has revealed that the top priority of stakeholders is of the caribou access safety. An elevated waste rock pile such as the NCRP may resemble an esker. This makes for a desirable location for wildlife such as caribou for insect relief as well as for the ability to spot prey. As such, the community members want to ensure that the slope of the NCRP is graded in such a way as to not generate a hazard for the caribou. This is one of the targeted closure goals of the Site which is detailed further in the next section.

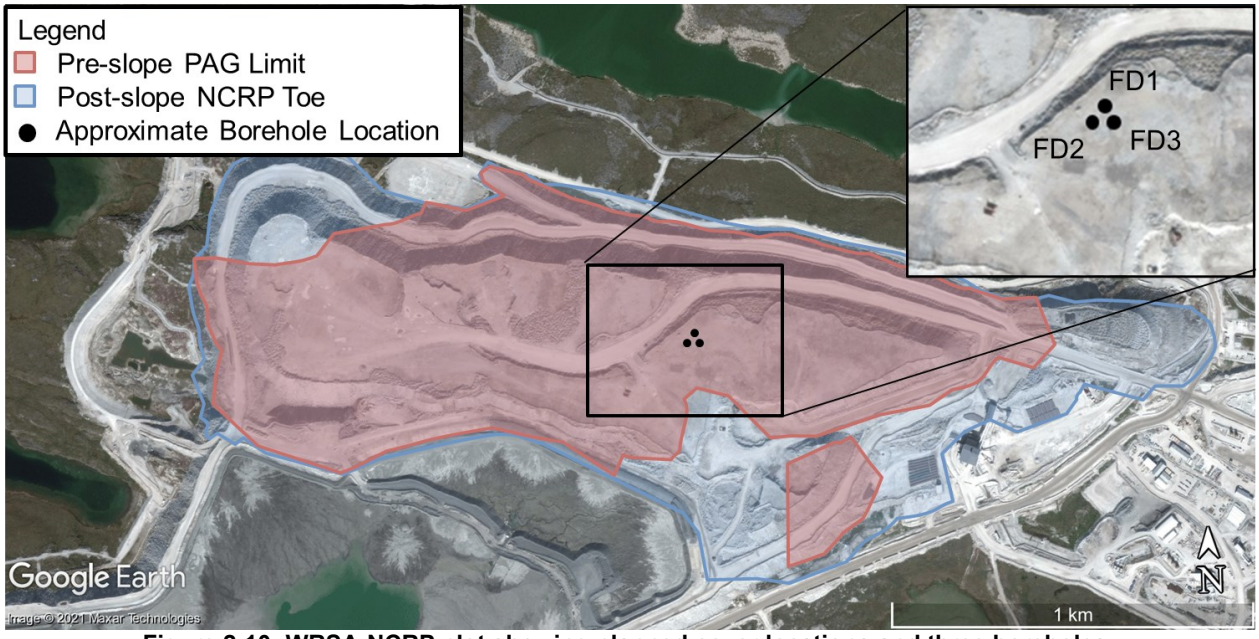

Figure 2-10: WRSA-NCRP plot showing planned cover locations and three boreholes With data from Golder (2017) with background image from Google Earth (2020)

2.8 Reclamation Planning and Targets

Closure planning at the Site began once the mine opened in 2003, with the establishment of a multi-discipline, interdepartmental committee 3 months after production began (DDMI 2018). This was a vital commitment that will promote the success of achievable reclamation objects. Table 2-3 shares an outline of the Site closure goals as presented by DDMI (2018).

Table 2-3: Site closure goals as per DDMI (2018)

1	Land and water that is physically and chemically stable and safe for people, wildlife, and aquatic life.
2	Land and water that allows for traditional use.
3	Final landscape guided by traditional knowledge.
4	Final landscape guided by pre-development conditions.
5	Final landscape that is neutral to wildlife – being neither a significant attractant nor significant deterrent relative to pre-development conditions.
6	Maximize northern business opportunities during operations and closure.
7	Develop northern capacities during operations and closure for the benefit of the north, post-closure.
8	Final site conditions that do not require a continuous presence of Mine Staff.

In addition, specific closure objectives (Table 2-4) were defined for the WRSA-NCRP.

Table 2-4: Site closure objectives for waste rock and till areas DDMI (2018)

1	Physically stable slopes to limit risk of failure that would impact the safety of people or wildlife.
2	Rock and till pile features (shape and appearance) that match aesthetics of the surrounding natural area.
3	Contaminated soils and waste disposal areas that cannot contaminate land and water.

The high standards established for the site and the WRSA-NCRP from key stakeholders since the beginning of the mine development have largely driven the research required to complete these objectives. The Diavik Waste Rock Project is one example of this research projects.

2.9 Diavik Waste Rock Project

The Diavik Waste Rock Project has been ongoing since 2004 with the purpose of demonstrating and quantifying the fundamental hydrological and biogeochemical processes occurring in waste rock. The project is a partnership between the University of British Columbia, University of Alberta, University of Waterloo, and Carleton University. Funding for the project has been supplied by numerous organizations including DDMI, INAP, and the National Sciences and Engineering Research Council (NSERC).

2.9.1 Test Piles

At the Site the waste rock material is classified into three different categories based on their respective sulfur contents as summarized in Table 2-5: Type I (T1, <0.04 wt.% S); Type II (T2, 0.04 to 0.08 wt.% S); and Type III (T3, >0.08 wt.% S). One of the key parts of the Diavik Waste Rock Project involved the construction of three 15 m tall waste rock piles, commonly called the “test piles”. Figure 2-9 shows the location of the three structures (T1, T3 and the Covered test pile) in relation to the rest of the site. A closer view of the piles is shown in Figure 2-11. Smith et al. (2013b) describes the design basis of the three structures. The T1 and T3 piles have the same geometry and are based on a minimum crest width of 20 m to allow for equipment access. They have a height of 15 m and a slope angle set at the angle of repose of 38° (1.3H:1V). The resulting base was 50 m by 60 m. The third test pile (the Covered test pile) is larger, designed with a 24 m crest with a shallower slope angle of 18° (3H:1V) to coincide with the closure design of the WRSA-NCRP (DDMI 2018). The resulting base is 60 m by 80 m. The T1 and T3 test piles are composed of just one material while the Covered test pile contains the proposed cover design by DDMI (2018) of 3.0 m of T1 material and 1.5 m of till on top of the T3 waste rock (10.5 m).

Table 2-5: Site material classifications according to sulfur content

Material Classification	Wt.% Sulfur	Acid-Generating Potential
Type I (T1)	<0.04	Not Acid Generating (NAG)
Type II (T2)	0.04 to 0.08	Low Acid-Generating Potential
Type III (T3)	>0.08	Potentially Acid Generating (PAG)

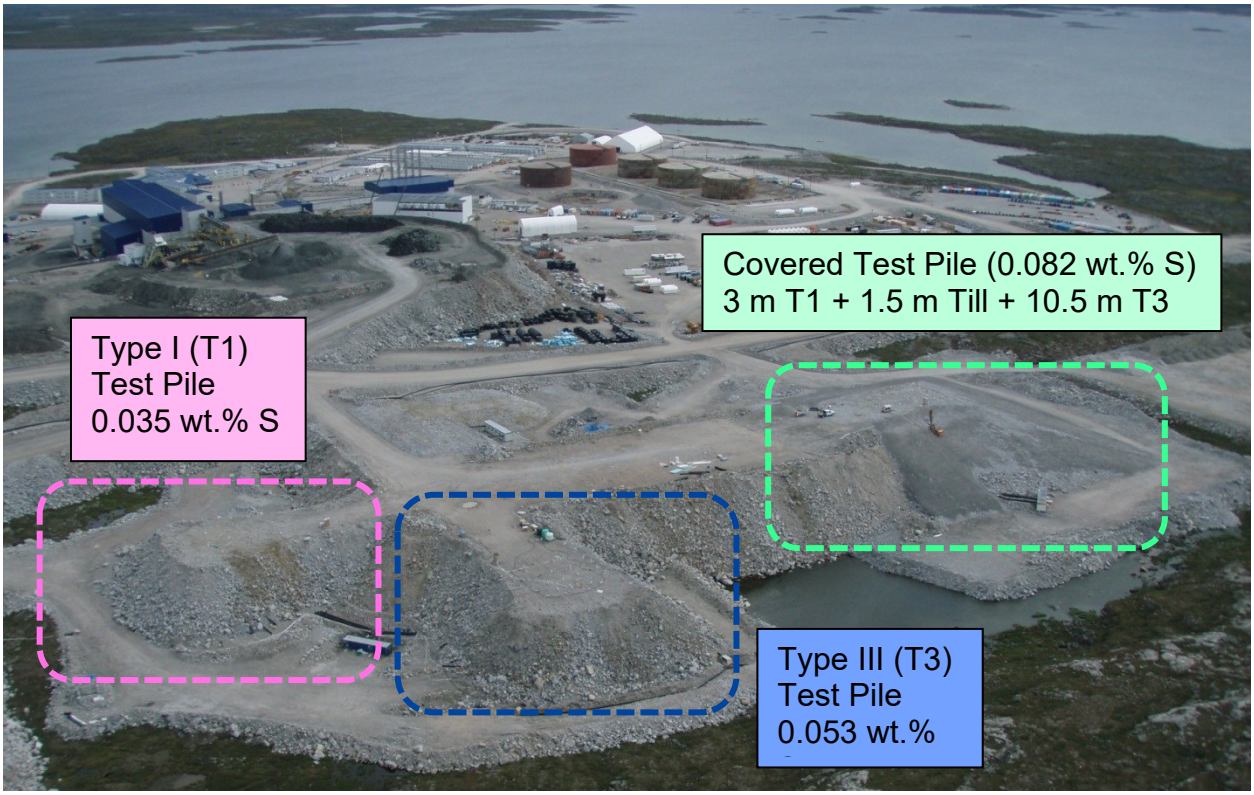

Figure 2-11: Overhead photo of the T1, T3, and Covered test piles at Site

The test piles were installed with various measuring systems to analyze a host of parameters such as temperature, air permeability, water flow, and water quality. The extensive list of testing instrumentation was summarized by Barsi (2017) and is presented in Table 2-6. A detailed description of the installation of the instruments are outlined in Smith et al. (2009) and Bailey et al. (2016).

Table 2-6: Site test pile and full-scale pile instrumentation
(Modified from Barsi (2017) and Pham (2013))

Instrumentation Name	Target Parameter	Location
Air permeability probes	Air Permeability	Internal pile, full-scale pile
Basal collection lysimeters	Water flow, Water quality	Basal, discrete collection
Basal drain collection lines	Water flow, quality	Basal, bulk
Gas sampling lines	Gas phase composition	Internal test pile, full-scale pile
Microbiology access ports	Microbial population	Internal test pile
Soil-water suction sampler (SWSS)	Water quality	Internal test pile, full-scale pile
TDR Probes	Moisture content	Internal test pile
ECH2O Probes	Moisture content	Full-scale pile

Instrumentation Name	Target Parameter	Location
Tensiometers	Matric water potential	Internal test pile
Thermal conductivity probes	Thermal conductivity	Internal test pile
Thermistors	Temperature	Bedrock, internal test pile, full-scale pile
Upper collection lysimeters	Water flow, water quality	Active zone

2.9.2 Full-Scale Pile Instrumentation

The full-scale pile (WRSA-NCRP), had a number of instrumentation installed in order to monitor the evolution of thermal, geochemical, and hydrogeological processes within the structure (Pham 2013). Pham (2013) describes three boreholes (FD1, FD2, and FD3) which were drilled into the structure in May 2010. The instruments installed in the boreholes included thermistor cables, gas lines, SWSS, moisture content sensors, and permeability probes as listed in Table 2-6. The boreholes were drilled 5 m apart at a diameter of 8" (approximate locations shown in Figure 2-10). The depths of the holes for FD1, FD2, and FD3 were 32.2 m, 30.7 m, and 40.2 m, respectively. The key measurement from this research was temperature from the installed thermistors. This thermistor strings had beads (measurement points) installed at 5 m vertical spacing with temperatures recorded in 12 h intervals.

2.10 Similar Research Examples

A number of corresponding documents with the Wek'èezhì Land and Water Board (WLWB) and DDMI lead to further thermal modeling of the WRSA-NCRP in order to satisfy conditions of their water license (W2015L2-0001) (WLWB 2015) This included a thermal model for the WRSA-NCRP developed by Tetra Tech (2017). While this model is similar to the research conducted in this thesis, the simulation does not account for convective heat transfer in either the (as-named) convective cover layer nor through the main waste material pile.

The following three mine sites show the use of similar soil covers operating in a permafrost environment.

2.10.1 Raglan Mine

A description of Raglan Mine is provided by Coulombe et al. (2012).The nickel-copper mine located in northern Quebec has been in production since 1997 under the operation of Glencore (previously Xstrata Nickel) and is still in operation today. The mine is located in a continuous permafrost environment with a MAAT of -10.3°C, which contributes to an active layer that is approximately 1 m thick (Coulombe et al. 2012). Tailings are stored on-site as dry-stack tailings in a tailings storage facility (TSF). As is often the case with metal mining, the tailings are PAG and

require a form of treatment to control ARD generation. An initial plan to use the surrounding permafrost environment and an insulating cover were proposed in 2002.

Coulombe et al. (2012) describe the cover system which is used to permanently keep the tailings in a frozen state to control the ARD generation. The tailings, stacked at a filtered solids content of 85%, are covered initially with a 1.2 m thick insulation cover consisting of crushed rockfill. As described by Elberling (2001, 2005), temperatures below zero may only reduce tailings oxidation rather than stop them completely, and as such an oxygen consumption test is employed to measure the effectiveness of an insulation cover (Coulombe et al. 2012). The results of the preliminary testing showed that the oxygen reactions were significantly reduced at temperatures at and below tailings temperatures of -5°C, which are shown to exist both with and without the cover system. This demonstrated that the insulation cover did not appear to have a significant impact on the oxygen consumption.

Further testing was conducted using a treated tailings material as an insulation layer (Benzaazoua et al. 2017). This research is part 1 of 2 focused on the environmental management of the pyrrhotite tailings at Raglan Mine. Once it was determined that the tailings could in fact be desulfurized (<0.5 wt.% sulfides) by removing more than 95% of the pyrrhotite material, the project advanced to part 2. Part 2, as described by Lessard et al. (2018), was the testing of the desulfurized tailings in a column test. The results of this study found that in addition to an insulation layer it may also act as an oxygen barrier, further promoting the reduction of sulfide oxidation. Finally, the desulfurized tailings were shown to have the desired physical and hydrogeological properties to be used as a cover material for the Raglan Mine tailings (Lessard et al. 2018).

2.10.2 Lupin Mine

A comparable study was conducted at the Lupin mine, located on Contwoyto Lake in Nunavut (previously the Northwest Territories), approximately 145 km northeast of the Diavik Diamond Mine (Pham and Sego 2013). The mine was a standard gold and silver operation which began operating in October 1982 (MEND1.61.2 1996). Due to the value of gold, the site has been in care in maintenance, non-producing since 2005, according to Crown-Indigenous Relations and Northern Affairs Canada et al. (CIRNAC et al. 2018). The site is situated within a continuous permafrost region and has a MAAT of -10.9°C (Pham and Sego 2013). Lupin Mine's ARD challenge is associated within the tailings impoundment. According to MEND1.61.2 (1996), the tailings are contained in a frozen dike impoundment, located within a tailings containment area.

In addition to acidic leaching there is also the presence of arsenic (a toxic, heavy metal) which threatens the water quality of the surrounding areas.

Beginning in 1988, Lupin Mine implemented a monitoring program which was intended to understand the permafrost development within the tailings, the effects of soil cover, and finally the resulting water quality. Progressive reclamation began in 1995 by placing a cover of sand and gravel-esker material at a thickness ranging from 0.6 – 1.6 m (MEND1.61.4 2004). This cover was designed to be saturated at 50% to provide a stagnant water oxygen barrier. The author goes on to describe the conclusions determined from the soil cover system at Lupin Mine. The field results showed that the active layer varied between 1.2 and 1.8 m, with greater active layer depths corresponding to lower cover thicknesses. Even though the warmer months allowed the active layer to penetrate 0.4 m into the tailings, no significant oxidation occurred. In addition, due to small loadings, the resulting water quality of the surface water passed discharge standards despite pore water being measured as slightly exceeding limits (MEND1.61.4 2004).

Pham and Sego (2013) modelled this cover system using COMSOL Multiphysics® 3.5a (Comsol 2018b, 2018a) and found similar results. They found that a 2 m thick esker-sand layer, with the lower 0.4 m being saturated, was enough to maintain freezing conditions in the PAG tailings material at Lupin mine. Further parameters were tested to determine the possibility of forming a convection cover within the esker material. It was found that if the material was permeable enough ($\geq 4 \times 10^{-7}$ m^2) then the 2 m thick cover would be sufficient to contain the active layer within the cover system. Additionally, the temperature results in the simulation demonstrated that the convective-cooling design generated colder temperatures than the conduction-only condition (Pham and Sego 2013).

2.10.3 Meadowbank Mine

The Meadowbank Mine is located in the Kivialliq region of central Nunavut, 300 km north of Hudson Bay. The mine site has been in operation since 2010 and the gold-producing operations have generated both PAG waste rock and tailings since then (Boulanger-Martel et al. 2021). The site is situated in the continuous permafrost region with a MAAT of -11°C and an active layer that ranges between 1.3 m and 4.0 m.

The PAG tailings has an average sulfur content of 2.17%, primarily from pyrite. The tailings are disposed in slurry form in external TSFs. Two experimental covers were constructed on a TSF in 2014 (2 m and 4 m) with NAG material. While technically the insulation cover material consists of just one material, it forms a two-layer system as the bottom 0.50 m of the cover is allowed to

remain saturated. This results in a highly saturated material with an overlying well-drained cover. Thermal behaviours were shown to be dominated by conductive heat transfer. Boulanger-Martel et al. (2021) found that both covers were able to maintain adequately cold temperatures which mitigated sulfide oxidation. Since the 2 m cover did allow some summer thawing of the PAG material over the study period (2014-2018), it may indicate future acid generation issues over a longer period of time. The study did not consider warming temperatures due to climate change and the author suggested the use of a more conservative cover thickness (4 m instead of the 2 m) to account for this and other uncertainties.

This soil cover was similarly used for the PAG mine waste rock pile on-site. The pile had a total of 5 benches with each bench having 4 m of cover. The total pile was 114 m resulting in a total pile and cover height of 118 m. Reactive transport modelling was conducted for the structure on-site with the 4 m cover thickness. The model was able to adequately simulate the conditions while accounting for freeze-thaw, water flow, geochemical reactions, and mass transport. This model did not consider the long-term effects of climate change (Yi et al. 2021).

2.11 Climate Change

Climate change is an extremely important factor in the engineering design of any structure located in a permafrost region, particularly those that are within the discontinuous zone of permafrost. The Diavik Diamond Mine is situated just north of the boundary of continuous and discontinuous permafrost (Tetra Tech Canada Inc. 2017).

Davis (2001) explains that solar energy is the largest contributor to near-surface ground temperatures and as a result it can directly impact ground temperatures from the top down. The author adds that climatic or other changes in temperature will result in the change of the active layer as well as the redistribution of permafrost zones. As global temperatures are predicted to increase and follow warming trends of the past century, effects of climate change must be taken into account when considering any type of modelling work, especially with those including climatic temperatures (Esch and Osterkamp 1990). An additional concern for northern sites is that the warming in higher latitudes is larger than that of lower latitudes (Brigham and Nelson 2003). MEND1.61.7 (2011) mentions that climate change is expected to have an impact on the closure of mines, particularly those which depend on a soil cover. This means that permafrost covers will need to be adapted to suite a warmer climate. A thicker cover would be required to account for a deeper active layer (MEND1.61.7 2011). If climate change is not taken into account, then a permafrost-dependent cover system would not be a practical solution for an ARD-generating site

Smith (2011) explains that the permafrost areas of Canada have been warming over the last 3 to 4 decades. These temperature increases are expected to continue over the next century, potentially eradicating the annual freezing of soils in the outer discontinuous permafrost areas. Overall, permafrost areas will see thickening of the active layer and a thinning of the frozen layer (Smith and Burgess 2004). This change due to warmer temperatures is included in Figure 2-3. The overall sensitivity of permafrost to global warming was characterized by Smith et al. (2004) by considering the present ground-temperature regime, the thermal response to warming, and the physical response to warming.

The Government of Canada (Bush and Lemmen 2019), published a report titled “Canada’s Changing Climate” which is the first report of a national assessment process. This assessment aims to examine how Canada’s climate is changing, the impacts, and how Canadians are adapting to the risk. This report is of particular importance due to a complete chapter on the changes in snow, ice, and permafrost across Canada. The report confirmed that over the past 3 to 4 decades permafrost temperatures have increased and that all emission scenarios show increases in mean air temperatures in permafrost regions in Canada.

Future climatic modelling is complicated and includes scenarios that consider many interconnected variables. For permafrost and frozen ground conditions the data is often directly measured which provides values of high confidence but can be sparse (both spatially and chronologically) considering the vast area and time frame that the data is required to represent. Despite the uncertainties in specific values, the editors of this report do present the following statement which is the key takeaway considering the future of Canada’s permafrost:

“*The proportion of Canadian land and marine areas covered by snow and ice have decreased, and permafrost temperatures are rising. These observed changes to the cryosphere are* ***virtually certain*** *to continue over the coming century in response to long-term increases in surface air temperatures under all emission scenarios.”*

(Bush and Lemmen 2019)

2.12 Software Considerations

The modelling environment required for this research needs to be able to account for density-driven (buoyancy) heat flow to adequately represent natural convective heat transfer. In addition, the model must be able to capture the latent heat impacts of freezing and thawing water.

Both the finite equilibrium software GeoStudio (Arenson et al. 2006, Arenson and Sego 2006, Wicky and Hauck 2017) and Comsol (Pham 2013, Pham and Sego 2013, Wicky and Hauck 2020) have been used to simulate similar problems.

Arenson and Sego (2006) established that there are limited numerical models that can model the effect of density driven air convection within soils. Arenson et al. (2006) noted that GeoStudio has the ability to solve air and water flow within unsaturated soils, though the code was required to be modified to solve for compressible air flow. Wicky and Hauck (2017) generated a numerical model of convective heat transport in talus slopes using GeoStudio. They noted that while this software was able to explicitly model the convective heat transfer in two dimensions, it was unable to account for the impacts of latent heat corresponding to freezing or thawing water. In addition, the authors mentioned the desire for a pressure boundary condition at the top of the model rather than an air flow boundary with the atmosphere.

More recent research from Wicky and Hauck (2020) transitioned to modelling using Comsol. The authors found pointwise validation beneficial to properly assess model performance as well as to quantify the contribution of convection to ground temperatures. They found that this software was able to better capture the formulation of natural convection in a porous media due to the purely equation-based modelling approach. In addition, the authors noted that Comsol had the option to implement a pressure boundary. While these were the limitations of the modelling environments at the time, it is likely that both software packages have advanced and should be reassessed at the time of future modelling.

3 Model Development

Likely due to limitations of GeoStudio identified by Arenson and Sego (2006) and Wicky and Hauck (2017), and the benefits of COMSOL Multiphysics® (Comsol) mentioned in Section 2.12, Pham (2013) employed the use of the Comsol environment to capture the field conditions at this Site. Wicky and Hauck (2020) found that this software was able to better capture the formulation of natural convection cells due to the purely equation-based modelling approach at the time. The base simulation reference section presents the findings by Pham (2013) and explains the decision behind the selected soil cover. This modelling approach was also utilized in the current research and key differences, assumptions, and limitations are discussed. As identified in the objectives, this model was updated to a more recent version for this research which warrants a benchmark comparison to ensure results are as expected.

3.1 Model Software

The modelling environment chosen for the use of this research was Comsol, version 5.4 (Comsol 2018b, 2018a). The program is a simulation software that allows for the coupling of any number of related physical applications using Finite Element Method (FEM) to solve complex problems (Comsol 2018b). The program interface is also developed in a user-friendly way that allows for those to take advantage of complex problems without being an expert on the mathematics or numerical analysis of a solution. In addition, the support team for Comsol includes technical experts who are able to understand and recommend solutions for a user's specific simulation requirements, rather than just aid in program troubleshooting. This support has been an indispensable tool for this research.

3.2 Base Simulation Reference

The original model was built by Pham (2013) and is described thoroughly in the referenced thesis. This research aims to rebuild the simulation that Pham (2013) developed for the modelling of the Diavik test piles (Section 2.9) and the full-scale waste rock storage area called the North Country Rock Pile (WRSA-NCRP, Section 2.7.4). This research would not have been possible without the extensive work conducted by Pham (2013) as well as the follow up personal communication and guidance they provided.

This research employs most of the formulae and methodology established by Pham (2013) to represent key field conditions and processes within the Comsol environment. Benchmarking of the recreated model will be conducted to ensure agreement, and then any changes to Pham (2013)'s original settings will be highlighted. The main purpose of this research is to recreate the

model environment in the more recent version of the software (version 5.4, (Comsol 2018b)) and conduct further sensitivity on parameters that were not originally explored by Pham (2013). Pham (2013) also included an engineered material to the design in order to enable a convective cover system for the WRSA-NCRP which will be used as the base case moving forward. Finally, the original, (non-engineered) material which was a part of the original closure concept for the WRSA-NCRP (as per Diavik Diamond Mines Inc. (DDMI 2018)) will be explored in order to offer multiple soil cover options.

3.2.1 Cover Designs

Material types for this research are defined based on their sulfur content as described in Section 2.9 (Table 2-5). To reiterate, the Type I material (T1) is classified is non acid generating (NAG) and the Type III material (T3) is considering potentially acid generating (PAG). There is also a material classified as Type II (T2) which falls in the middle of T1 and T3 in terms of sulfur content and is considered a material with low acid-generating potential. T2 material is much less abundant and negligible in comparison to the T3 material and therefore this research does not consider it in the simulation. The areas of the WRSA-NCRP which contain T2 and T3 materials at the surface of the structure are displayed in Figure 2-10. These areas were identified early on to require some sort of system to manage the reactive material. The chosen mitigation method from DDMI (2018) was a two-layer soil cover system that was designed to maintain the PAG T3 material in frozen conditions year-round through conductive heat-transfer. This cover design is one of the case studies that was evaluated by Pham (2013). It includes a lower layer of till followed by an upper layer of T1 waste rock as shown as Case 2 in Figure 3-1. The scenario (Case 2) was proposed by the mine operators and has proportions based on material availability (Langman et al. 2017). Both the T1 and till material are considered NAG. T1 waste rock is described as a high permeability material with a low moisture content due to its quick-draining nature. The cover, and particularly the T1 layer, is intended to contain the active layer during the cyclic freeze-thaw conditions in order to maintain the underlying T3 material (PAG, WRSA-NCRP) in frozen conditions. Situated between the T1 and T3 materials, the till layer is designed to remain saturated and form a latent heat layer due to its low permeability and high moisture content. An alternative to this design is an engineered material cover system. This system intends to take advantage of convective cooling and contains a modification to the original T1 material, provided as Case 3 in Figure 3-1. This altered material was originally proposed by Pham (2013). The engineered material is called T1 (coarse), and it represents the T1 waste rock which has been filtered to remove the fine fraction (≤3 cm) particles.

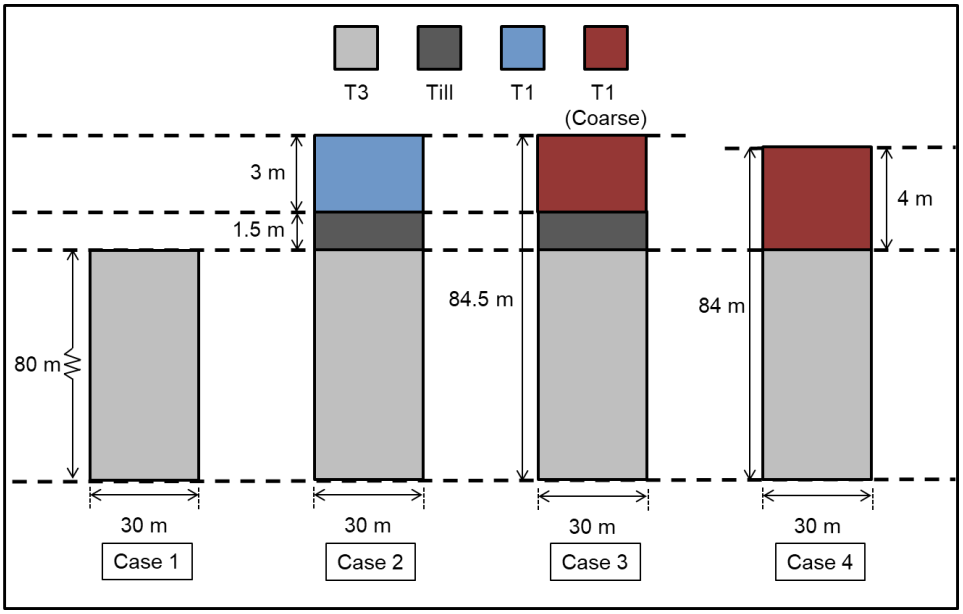

Figure 3-1: Simulation cases as described and analyzed by Pham (2013)

Pham (2013) conducted an analysis on four scenarios of thermal cooling for the 80 m WRSA-NCRP. These scenarios accounted for the increase in annual temperatures due to climate change (formulae discussed in Section 3.6.2.1) over a period of 100 years (July 2010 to July 2110). The assumed climate change increase brought the mean annual surface temperature (MAST) from -6.3°C (Equation 3-5) to -0.7°C. The four scenarios (Cases 1-4) are outlined in Table 3-1. In this table, N/A indicates that the results were not included in the writeup by Pham (2013). As the author ran the simulations from 2010 onward it allowed for validation between model results and field conditions. A summary of the results found by Pham (2013) are presented in Table 3-1.

Table 3-1: Pham (2013) summary for the full-scale pile after 100 years

Case	Desc.	Cover design	Heat transfer	2110 Result		Permeability of T1/T1 (coarse) (m^2)
				Depth of 0°C Isotherm	Maximum temperature at top of till*	
1	Baseline case	No Cover, 80 m T3	1D, Conduction	7.0 m	N/A	N/A
2	Closure concept for mitigation	1.5 m till, 3.0 T1	1D, Conduction	3.9 m (0.9 m into till)	+1.9°C	2×10^{-9}
3	Air convective cover (ACC)	1.5 m till, 3.0 T1 (coarse)	2D, Conduction + Convection	2.5 m	~0°C	9×10^{-8}
				NA	-0.3°C	2×10^{-7}
				NA	-2.4°C	4×10^{-7}
				NA	-3.1°C	6×10^{-7}
4	ACC, no till	4.0 T1 (coarse)	2D, Conduction + Convection	5.1 m (1.1 m into T3)	+0.7°C (*Top of T3)	9×10^{-8}
				3.4 m	-1.8°C	2×10^{-7}
				2.7 m	-5.3°C	4×10^{-7}
				2.5 m	-6.3°C	6×10^{-7}

3.2.2 Model Validation Conducted by Pham (2013)

Model validation was conducted for Case 1, which represents the default field conditions of the WRSA-NCRP. The temperature profile of the WRSA-NCRP was able to be determined according to three installed thermistors within the pile (see Section 2.9.2 for a description of installed thermistors). Thermistors were placed into boreholes FD1, FD2, and FD3 (Figure 2-10). Case 1 temperature profile results were comparable to field conditions (at three depths) with a few slight discrepancies. Pham (2013) explains these discrepancies were likely due to the heterogeneity of the waste rock pile in the field as well as excess water which was introduced in the drilling of the boreholes in May 2010. The author was satisfied with these results and confirmed the modelling environment captured field conditions well. The initial active layer depth (assumed as the 0°C isotherm) was 11 m which was likely a result of the structure not yet at equilibrium with its surroundings (amplified due to introduced water from borehole drilling, which may have presented a deeper active layer).

3.2.3 Case 1 Simulation (Pham 2013)

In the Case 1 simulation (no cover, Figure 3-1) the active layer (assumed up to the 0°C isotherm) began at a depth of 11 m. Initial rapid cooling of the structure occurred during the first four years which reduced the active layer thickness to 3.9 m in 2014. This cooling was a result of the large temperature difference between the structure and the cold winter temperatures. This condition is present in all four case studies. Further cooling brought the active layer to its shallowest point in 2020 (3.7 m). The remaining 90 years saw the active layer increase in depth as the surface temperature increased. The active layer reached 7.0 m in 2110 (Table 3-1). This would mean that a NAG cover with similar thermal properties of the T3 rock would need to be at least 7.0 m to maintain the T3 rock in frozen conditions. Results found that the effects of seasonal temperature changes at surface became negligible (with seasonal amplitudes of ~0°C) at a depth of 20 m.

3.2.4 Case 2 Simulation (Pham 2013)

Case 2 included the closure concept as described in DDMI (2018). This soil cover design has a total depth of 4.5 m (1.5 m of till overlain by 3.0 m of T1 material) as seen in Figure 3-1. Although the results of Case 1 indicated the potential need of a 7.0 m cover layer, the till and T1 materials have different thermal properties than T3 and the required overall cover thickness may be less. The total structure becomes 84.5 m with the Case 2 cover. The active layer in Case 2 started at 11 m in 2010 and decreased to 3.0 m at the top of the till surface (i.e., the entire T1 layer was thawed) by 2015 where it remained stationary for a total of 25 years. The latent heat layer (till)

delayed the active layer penetration into the PAG T3 material due to the large amount of latent heat required to thaw the till. Once the layer eventually thawed in 2040, the active layer gradually increased to 3.9 m in 2110 (penetrating 0.9 m into the 1.5 m layer of till material). This means that in 2110 the temperature at the top of the till layer was greater than zero (1.9°C, Table 3-1). Similar to Case 1, the seasonal temperature changes no longer impacted the soil at a depth of 20 m, despite the change in material of the upper 4.5 m of the system. While the T3 material was still frozen after 100 years, the thawing of the till layer indicates that the latent heat protection had already been mostly overcame and thus the thawing of the PAG material is imminent. While the surface temperature increase initiated by climate change is unable to be prevented, the temperature of the till material at the beginning of this simulation can impact the end results. A system which transfers the cold winter temperatures down into the pile more effectively during the initial rapid cooling phase may find better results and further delay thawing. This was the purpose of the Case 3 investigation, described below.

3.2.5 Case 3 Simulation (Pham 2013)

The Case 3 simulation introduced an engineered material in order to initiate convective heat transfer to cool the PAG structure further. If colder temperatures can be reached within the pile earlier on in the simulation, it would take longer for the till and underlying T3 to begin to thaw. Air convective covers (ACCs) and their purpose are described in Section 2.6.2. Case 3 used the same layer prescription as Case 2, however, the T1 layer was changed to a higher permeability material (T1 (coarse)) as seen in Figure 3-1. While a material's permeability (K) can be calculated according to Hazen's formula ($K \geq 3 \times 10^{-7}$ m^2, see Section 3.6.6.5) a range of permeabilities were tested by Pham (2013). As described in Section 2.5.4.1, the permeability is tied to cooling effects as an increased permeability may allow for a greater Rayleigh value (Ra) to be produced in the T1 (coarse) material layer, thus preventing the thaw of the T3 material. The critical Rayleigh value (Ra_c) for this simulation was 27.1, which was exceeded in all four tested permeabilities ($K = 9 \times 10^{-8}$ m^2, 2×10^{-7} m^2, 4×10^{-7} m^2, and 6×10^{-7} m^2). This means that all four permeabilities allowed for convective cooling. The Rayleigh value of each simulation changed during the year with seasonal changes. Looking at a period of June 2015 to April 2016, it was found that convection was initiated between mid October to mid March, allowing for roughly 4.5 months of convective cooling within the T1 (coarse) material. It was also noted that at a depth of 30 m the impact of the seasonal temperature changes from the surface were visible for $K = 9 \times 10^{-8}$ m^2 and $K = 2 \times 10^{-7}$ m^2 but they were not present for $K = 4 \times 10^{-7}$ m^2 and $K = 6 \times 10^{-7}$ m^2. This resulted in a chosen

ideal permeability for the T1 (coarse) material to be 4 x 10^{-7} m^2 which is comparable to the calculated permeability from Hazen's formula (K ≥ 3 x 10^{-7} m^2, see Section 3.6.6.5).

3.2.6 Case 4 Simulation (Pham 2013)

Case 4 built on the Case 3 simulation and adds a contingency option should there not be sufficient till material on-site. The cover design for this case included only T1 (coarse) material which was increased to 4.0 m in an attempt to account for the missing latent heat till layer. The total structure then reaches 84.0 m, as shown in Figure 3-1. The same range of permeabilities for the T1 (coarse) material shown in Case 3 were used for Case 4. The required critical Rayleigh value is also 27.1 as the boundary conditions remain the same as in Case 3. As expected, Equation 2-29 demonstrates that an increase in the convective layer thickness (H) (3 m to 4 m for Case 3 and 4, respectively) results in an increase in the Rayleigh value. As a result, all four permeabilities initiated convective cooling. As shown in Table 3-1 the 0°C isotherm of the lowest permeability case (9 x 10^{-8} m^2) reaches the T3 material at a depth of 4 m in 2090 and continues to increase in depth until 2110. At this point the isotherm is at a depth of 5.1 m which means that the upper 1.1 m of the PAG T3 material is thawed. The remaining three permeabilities (K = 2 x 10^{-7} m^2, K = 4 x 10^{-7} m^2, and K = 6 x 10^{-7} m^2) tested were able to keep the material frozen while the active layer remained in the cover.

3.2.7 Simulation Summary as per Pham (2013)

Pham (2013) identified the Case 3 simulation to be the favoured mitigation technique since less material is required to keep the T3 material frozen for the same permeabilities when comparing Case 3 and Case 4. In both cases, the minimum permeability to maintain the material below the T1 (coarse) cover in frozen conditions was K ≥ 2 x 10^{-7} m^2. In addition, a permeability of K ≥ 4 x 10^{-7} m^2 did not show indications of the cyclic surface temperature at a depth of 30 m. Finally, initial calculations of T1 (coarse) showed an expected permeability of K ≥ 3 x 10^{-7} m^2 according to the assumed particle size distribution. As a result, future modelling will use K = 4 x 10^{-7} m^2 as a base case assumption for the permeability of T1 (coarse).

3.3 Assumptions and Limitations

3.3.1 Immobile Water

In lieu of a three-phase system (air, water, soil) this model simplifies the field conditions of the WRSA-NCRP to a two-phase system (air and soil) in order to apply Darcy's Law. As a result, the model does not account for the movement of water within the waste rock pile but rather how the

heat transfer methods (convection and conduction) may cool the pile over time. The water content is considered for the T1, T3, and till materials as it will impact their respective thermal conductivities and heat capacity values. As a result, any water is considered immobile, and the fluid material used for convection in the T1 structure is air. While the till material is considered to have a high degree of saturation and a low permeability it is also assumed that this water is captured and remains in the till. With a low degree of saturation for the T1 and T3 materials being defined by present field conditions (described later in Section 3.6.6.3) it is assumed that this water is also contained within their respective layers. The water does not move between different material types thus resulting it immobile. These assumptions are in line with those assumed by Pham (2013).

3.3.2 Wind-induced Advection

Previous research (Pham 2013) took into account wind-induced advection and natural air convection on an uncovered test pile which was found to make a significant impact on the internal temperatures. While examining the Covered test pile however, it was found that wind-induced advection and natural air convection were eliminated due to the presence of the low permeability till layer. In addition, the narrow orientation of the uncovered test piles (small width to height ratio) allowed for wind to easily penetrate through the test piles which may have overestimated the wind effects. Pham (2013) points out that the full-scale WRSA has a much higher width to height ratio (~1 km:80 m) along with embedded low permeability layers created as a result of pile construction methods which would inhibit most, if not all, wind-induced advection. The impact of wind is likely only to be seen in small areas at the edge of the WRSA. As a result of these findings this research does not take account wind-induced advection during long term thermal modelling.

3.3.3 Heat Release by Oxidation

The heat release by oxidation of the sulfide minerals is a concern when managing a reactive waste rock structure such as this. Pham (2013) performed a heat budget analysis of the test piles. The measured internal temperature of the T3 test pile displayed temperature variations that were distributed uniformly within the structure. Heat generated due to sulfide oxidation can often show local warm or hot spots which were not present in this field study. The heat balance showed that there is negligible heat release in this structure. Pham (2013) calculated the temperature change as a result of sulfide oxidation for the T3 test pile by assuming an estimated oxidation rate of T3 rock and a known bulk volumetric heat capacity of the material. This yielded a temperature increase of +0.0061°C annually. This temperature change would be negligible considering the annual temperature increase due climate change was +0.056°C (presented in Section 3.6.2.1).

Amos et al. (2009) confirmed that the airflow (wind-induced and temperature-induced) within the pile was large enough to allow for adequate oxidation of the pyrite material, so that was not the reasoning for the low value. As a result, the heat released by oxidation was considered negligible due to the low oxidation rate of the T3 waste rock (Amos et al. 2009, Pham 2013).

3.3.4 Climate Change

An air temperature increase as a result of climate change is introduced into the simulation via a surface temperature boundary condition. It is noted that climate change will impact many parameters other than just air temperatures such as seasonal precipitation levels, cloud cover, and wind speed (Esch and Osterkamp 1990). The author acknowledges this limitation. One of the sensitivity analyses varies the climate change temperature to ensure the suggested design can potentially account for the unknowns associated with global climate change which may create harsher conditions than anticipated.

3.3.5 Radiative Heat Transfer

As described in Section 2.5.3.2, radiative heat transfer can be a large contributor to the total heat transfer equation should the material be adequately coarse and dry (Johansen 1975, Côté et al. 2011). It was found that the material that was used in this research was not within these bounds and therefore it was assumed that the radiative heat transfer within the waste rock structures was negligible compared to convective and conductive cooling (Pham 2013).

While not modelled specifically in the simulation, radiation does impact the surface heat flux which in turn influences the temperature changes within the pile. Pham (2013) produced a detailed calculation behind the calibration of the surface temperature (Equation 3-5) which accounts for a number of different site-specific parameters such as net radiation. The calculation of net radiation is a key parameter which involves the short-wave and long-wave radiation produced by the sun and atmosphere and the surface which reflects short-wave radiation and emits long-wave radiation (Weeks and Wilson 2006, Pham 2013). Pham (2013) notes that net radiation at the surface is the key term in the surface energy balance equation as it can control other transport processes such as evaporation. Further details on this calculation can be found in Pham (2013) with key theoretical analyses summarized by Weeks and Wilson (2006).

3.3.6 Snow Cover

The relationship between air and ground temperatures is correlated linearly in Northern Canada, though there is a large amount of scatter due to the number of sites included. A statistical relationship provided by Smith and Burgess (2000) indicates a 0°C MAST correlates to -4.3°C

mean annual air temperature (MAAT), with data compiled by Pham (2013). Pham (2013) calculated the site-specific correlation of 0°C surface temperature correlating to -4.9°C air temperature for the test piles which fits with the trend provided by Smith and Burgess (2000). One of the site conditions that can alter this air-surface relationship is snow cover due to its insulative properties and albedo. These factors can greatly impact solar radiation reflection. Snow cover is a good insulator and Pham (2013) mentions that a snow cover kept the surface temperature of the test piles warmer than air temperatures, opposite of the typical relationship. This measurement correlated to a measured snow thickness of 25 cm which was measured at nearby Ekati Mine during the 2006-2007 winter period (October – April) with 60% of precipitation occurring as snow at site (Neuner et al. 2013). The net radiation and surface heat flux calculation considered the presence or lack of snow during the summer or winter months which was used to form Pham (2013)'s annual surface temperature formula (presented later on in Equation 3-5).

3.3.7 Material Heterogeneity

Heterogeneity is an important consideration when modelling any sort of structure that is built from earth materials. One limitation for the materials used in this simulation is that they are classified according to their sulfur content rather than based on their particle sizes. While there are values that are chosen to represent the average particle sizes and resulting properties of each material type these can vary considerably at local levels of a structure.

The heterogeneity that is found within WRSAs, particularly material segregation during deposition, will present itself as an uncertainty in the permeability. The deconstruction of a test pile at Site and the associated material variability and segregation is described in Barsi (2017). The way waste piles are commonly built in the mining industry introduces the concept of tip faces. This is when equipment such as a dozer will push material over the side of a waste rock pile. As the material falls over the edge, a tip face is created, and the material may separate according to particle size. It is common for coarser material to be found near the bottom of the tip face and the finer materials resting at the top. As WRSAs are built, many tip faces are built laterally throughout the pile. Depending on building preferences, these waste dumps can also change construction direction or lift heights throughout the structure. These interbedded layers of permeability are not represented distinctly in the simulation though the variability of permeability is considered.

3.4 Geometry

The 80 m WRSA-NCRP is recreated as a 2D column simulation with the soil cover of choice added on top. Pham (2013) suggests a 2D model width of at least 10 times the thickness of the

initial coarse rock layer (i.e. 30 m) in order to make the T1 (coarse) domain equivalent to an infinite horizontal layer. The base case model is designed as a 2D column with three layers as seen in Figure 3-2.

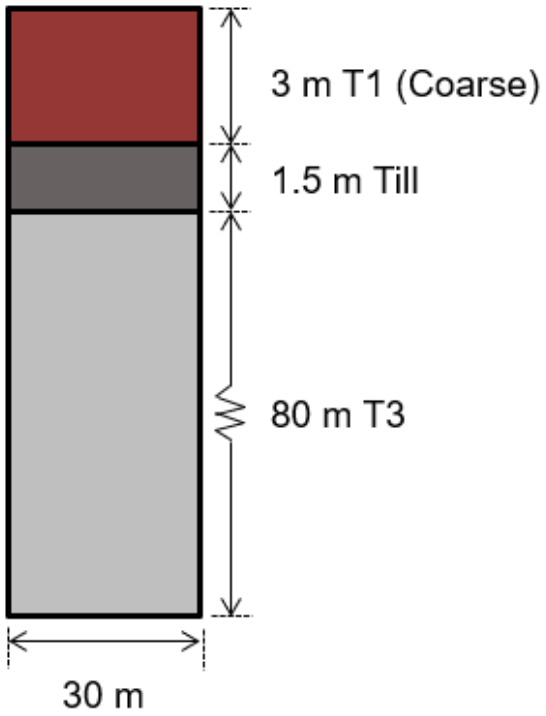

Figure 3-2: Schematic of base case 2D simulation of the WRSA-NCRP

3.5 Governing Equations

The model consists of a porous media (waste rock) and permeant (air). Initially outlined by Pham (2013), the following governing equations and principles are to be observed:

1. Conservation of Mass (continuity) of Air (Equation 3-1)
2. Conservation of Momentum (Darcy's law) (Equation 3-2)
3. Conservation of Heat (Thermal equilibrium) (Equation 3-3)
4. Ideal gas law of air (Equation 3-4)

Where η, K, C, and λ are the porosity, permeability, specific heat, and effective thermal conductivity of the porous media, respectively. The remaining variables ρ_f, $\mathbf{u}$, ν_f, p, T, c_f, M, and R are defined as the density, velocity vector, dynamic viscosity, pressure, temperature, specific heat capacity, molar mass, and gas content of the permeant fluid, respectively.

$$\eta \frac{\partial \rho_f}{\partial t} + \nabla \cdot (\rho_f \boldsymbol{u}) = 0 \quad \text{3-1}$$

$$\boldsymbol{u} = -\frac{K}{\nu_f}(\nabla \mathrm{p} + \rho_f g) \quad \text{3-2}$$

$$C \frac{\partial T}{\partial t} + \nabla \cdot (-\lambda \nabla \mathrm{T} + \rho_f c_f \boldsymbol{u} T) = 0 \quad \text{3-3}$$

$$\rho_f = \frac{pM}{RT} \quad \text{3-4}$$

3.6 Physics Modules

There are two physics modules defined and coupled in this model. They include Darcy's Law (dl) (Comsol 2018b) for the fluid flow mechanics and the Heat Transfer in Porous Media (ht) (Comsol 2018a) for the heat transfer mechanics. Darcy's law is used to relate pressure and interstitial air velocity.

3.6.1 Physics Coupling

Comsol offers two options for physics coupling with the two modules. The options are called **Temperature Coupling** and **Flow Coupling**. As outlined in Comsol (2018a) these features implement a one-way coupling (one in each direction). It is possible to only use **Flow Coupling** if the fluid properties are not temperature dependent, however in this physical model that is not the case. The temperature cooling effect depends on the density change of air as temperature changes and as a result both coupling options are required.

3.6.2 Boundary Conditions

Boundary conditions for this simulation are based off the findings and conditions outlined by Pham (2013). A schematic of the boundary conditions for the 2D simulation is displayed in Figure 3-3, with details outlined in Section 3.6.2.1, Section 3.6.2.2, and Section 3.6.3.

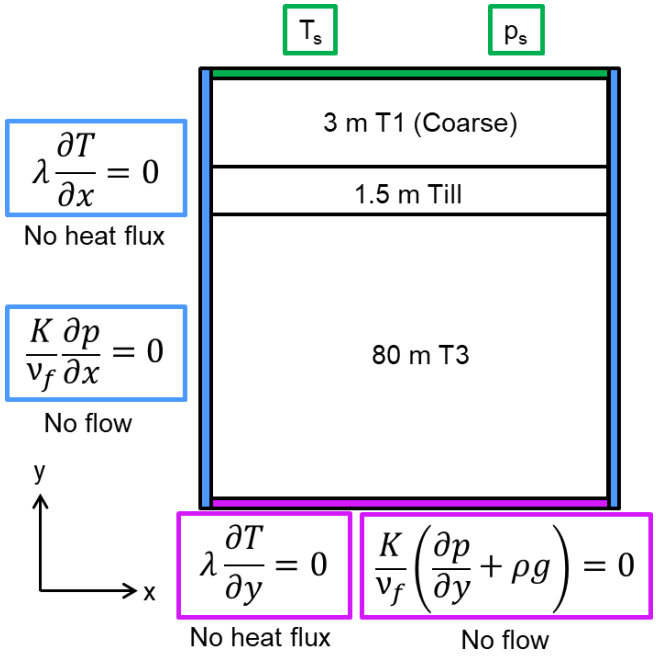

Figure 3-3: Boundary conditions of model simulation

3.6.2.1 Temperature

Boundary conditions of the model include a no heat flux boundary condition (thermal insulation) along the bottom and sides as shown in Figure 3-3. This assumption of no heat flux at the bedrock boundary is supported due to a low thermal conductivity geomembrane liner which was placed at this interface prior to construction. Often a geothermal gradient would be included at the base of a WRSA that sits on bedrock, however, as the structure is 80 m in height, the temperature at the surface is not greatly impacted by this gradient. As a result, this boundary is kept as a no heat flux boundary. Synonymously, it was shown during simulations by Pham (2013) that surface temperatures did not impact temperatures at depths of 30 m, so the 80 m structure would see negligible temperature changes at the base.

There is also a no flow boundary at the base of the model as the bedrock below the structure is assumed to be impermeable. The no heat flux and no flow boundary at the sides of the model are chosen as this simulation width is adequately large to represent an infinitely horizontal plane as described in Section 3.4. The model allows for 2D heat transfer and fluid flow and the geometry is chosen to be independent of edge-effects at the center of the simulation domain.

The surface temperature of the simulation is defined as T_s. This temperature is critical as it defines both seasonal fluctuations as well as an annual increase to the temperatures due to climate change. An introduction to the amplified issue of climate change in permafrost regions is included in Section 2.11, with acknowledged limitations of the simulation in Section 3.3.4. A study into the

potential climate change scenarios was conducted specifically for this Site by Environmental Modelling and Prediction P/L Australia (EMAP 2008). This study included future long-term modelling scenarios of air temperatures for the period between 1970 and 2060. Pham (2013) also validated the data with site temperatures for the years 2000 to 2010 and found that the predictions correlated well with the known site conditions. The mean temperature increase found by EMAP (2008) was +0.056°C/year, which is what Pham (2013) implemented into their model simulations.

The resulting formula to capture both the sinusoidal nature of seasonal temperature changes as well as the annual increase as a result of climate change is demonstrated in Equation 3-5 (Pham 2013). This equation presents the surface temperature of the model versus time (t) in days.

$$T_s = -6.3 + 20.4 \sin\left(\frac{2\pi}{365} t\right) + \frac{0.056}{365}(t) \quad \textbf{3-5}$$

3.6.2.2 Pressure

Initial pressure conditions of the model include a no flow boundary condition on the sides and bottom of the 2D column. This assumption was justified by Pham (2013) due to the low permeability of the bedrock. The pressure on the surface of the simulation (p_s) is defined in Equation 3-6. Ground pressure is set at atmospheric pressure (p_{atm} = 101.3 kPa) as per Pham (2013), with pressure decreasing linearly with the factor of height (y), gravity (g), and air density (ρ_a). Air density will change with temperature as defined by the ideal gas law (Equation 3-4).

$$p_s = p_{atm} - \rho_a g y \quad \textbf{3-6}$$

3.6.3 Initial Temperature Profile

The initial temperature with depth is extrapolated from data found in historical temperature data of the full-scale pile. The full-scale pile was instrumented with three deep boreholes (FD1, FD2, and FD3) as described previously in Section 2.9.2 (location seen in Figure 2-10). The most recent complete set of data that was able to be extracted from the thermistors was seen in FD3 up to May 2016. Average monthly temperatures were determined between April 2015 and May 2016 and the resulting temperature variations are shown in Figure 3-4 with locations of temperature spacing marked. The shallowest thermistor reading is at 4.5 m, with 5 m spacing to a depth of 39.5 m. Analyses of varying initial temperature profiles demonstrated that the initial temperature profile does alter the maximum temperatures after 100 years, however, as field work is likely to be conducted in the summer months the temperature profile of July 2015 is chosen to represent

the initial temperature of the simulation. A ground surface temperature is calculated according to Equation 3-5 and this profile is extrapolated upwards for a total simulation height of 84.5 m (shown as a depth of -4.5 m). At a depth below 39.5 m the temperature profile is extended downwards for the full depth of the model. This profile is presented in Figure 3-5, along with a schematic of the material prescriptions that were outlined in Section 3.2.1.

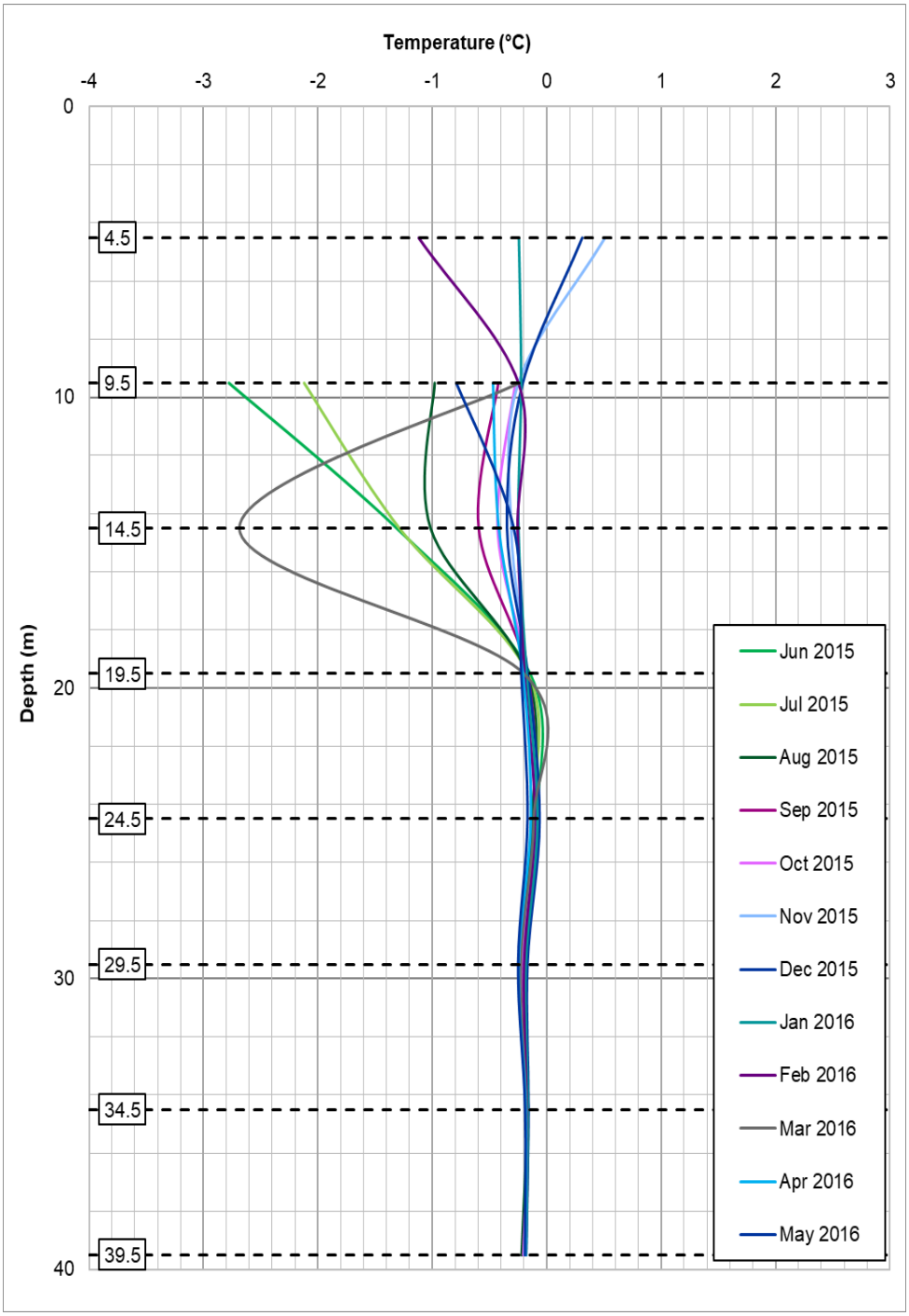

Figure 3-4: Average monthly temperatures of borehole FD3 (June 2015 to May 2016)

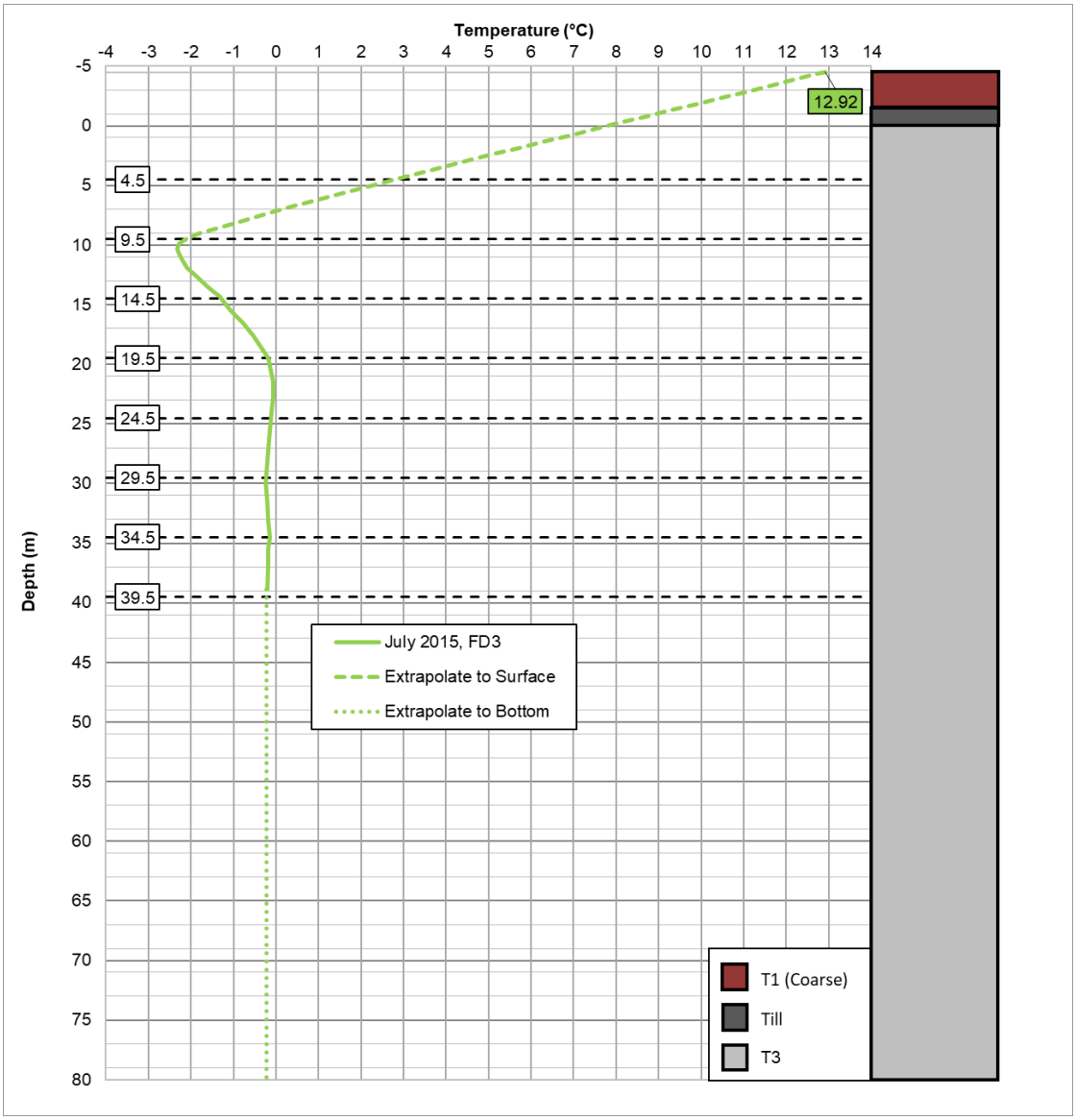

Figure 3-5: July 2015 average temperature profile (FD3) with soil cover prescription overlay

3.6.4 Material Descriptions

3.6.4.1 Type III (T3) Rock

T3 waste rock is the dominant PAG material at Site. It is the material which makes up the largest extents of the WRSA-NCRP as outlined in Section 2.7.4. The simulation of this structure contains the base 80 m thick layer of the T3 waste rock as depicted in Figure 3-2.

3.6.4.2 Till

The till material geology is described in Section 2.7.3. Till material at Site has a low permeability and is used as the latent heat layer in the cover system. This layer also has the added benefit of preventing oxygen and water infiltration (outlined in Section 2.6.2) in to the PAG T3 material. The

base case model simulation contains a 1.5 m layer of till as demonstrated in Figure 3-2. The till that would be used in this structure is primarily from the development of the A21 kimberlite pipe.

3.6.4.3 Type I (T1) Rock

T1 material is the waste rock which is classified as NAG (Table 2-5). The original closure concept of the cover for the WRSA-NCRP included T1 material as the top layer (DDMI 2018). As summarized in Section 3.2, Pham (2013) demonstrated that the initial closure concept may not maintain the T3 material in frozen conditions after 100 years due to increasing surface temperatures. If the heat transfer mechanism can be adjusted to initiate a convective heat transfer system in the T1 layer it could improve these results. As described in Section 2.6.2, the T1 material may be filtered to remove some of the finer particles. Pham (2013) suggests the removal of particles that are ≤3 cm in order to create an engineered T1 (coarse) material. T1 (coarse) has a low thermal conductivity, high porosity, and a high permeability which has shown successful simulation results of keeping the T3 material frozen after 100 years despite the increasing surface temperatures.

3.6.5 Grain Size Distributions and Soil Classifications

Pham (2013) analyzed and classified the material used in the construction of the Covered pile (see Section 2.9.1) at Site according to ASTM D2487 (2017). Table 3-2 outlines the size classification of T1, T3, and till materials with their particle size distributions shown in Figure 3-6. The materials are classified as a well-graded gravel, a well-graded gravel with silt, and a poorly graded sand with silt for T1, T3, and till, respectively.

Table 3-2: Particle size and soil classification of T1, T3, and till properties as per Pham (2013)

Property	Type I	Type III	Till
Sample Location	*Type I Pile*	*Covered Pile Layer*	*Covered Pile Layer*
Size Classification (D_x size passing x%)			
D_{10} (mm)	0.37	0.19	0.08
D_{30} (mm)	3.08	2.22	0.33
D_{50} (mm)	10.24	8.41	1.11
D_{60} (mm)	15.48	13.16	2.79
Coefficients			
C_u	56.70	80.57	35.91
C_c	1.71	1.60	0.52
Soil Classification			
Group Symbol	GW	GW-GM	SP-SM
Group Name	Well-graded gravel	Well-graded gravel with silt	Poorly graded sand with silt

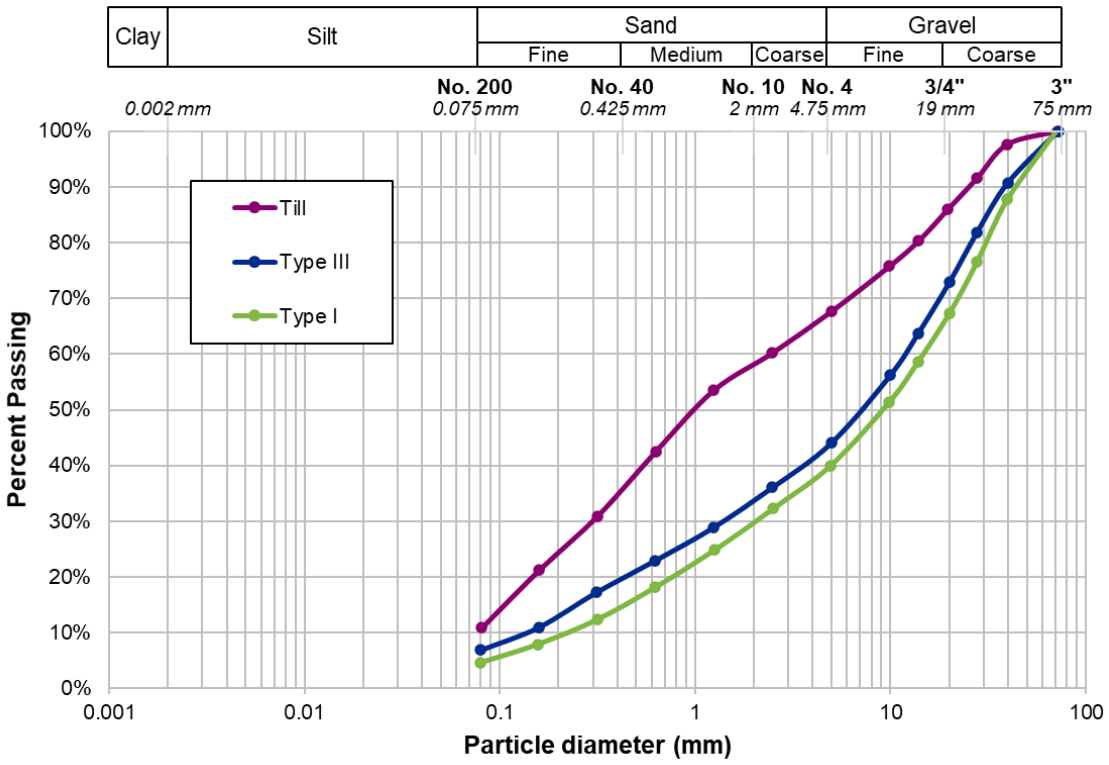

Figure 3-6: Particle size distribution of T1, T3, and till materials (Adapted from Pham (2013))

3.6.6 Material Properties

The various material properties used in this research are summarized in Table 3-3. Most of the parameters are based on the same parameters listed by Pham (2013) with the remaining assumptions made for this research outlined in the following sections.

3.6.6.1 Solid Density

The material density input into the simulation requires the solids density even though the module is for porous media. Previous modelling (Pham 2013) used a solids material density of 2700 kg/m^3 for the T1 (and therefore T1 (coarse) material) and T3 waste rock. These values correspond with quoted bulk density, porosity, and moisture content values described by Neuner (2009) and Bailey (2013) for these materials. The till material had fewer on-site classifications from the Diavik Waste Rock Project and the material properties were historically defined from literature for modelling purposes (Pham 2013). Terzaghi et al. (1996) indicates a solids density of 2650 kg/m^3 for material classified as “glacial till, very-mixed grained”. Reports from the classification of till material from the development of the kimberlite pipes have values in the same range as above (EBA 2004, BGC 2014). The till material uses a solids density of 2650 kg/m^3 as seen in Table 3-3.

3.6.6.2 Porosity

The large-scale porosity of "blasted material" at the Site was estimated by Neuner et al. (2013) as 0.25 from the hydraulic testing of a 16 m^3 waste rock sample. This porosity is applied to both the T1 and T3 material. The T1 (coarse) material achieves a larger porosity value with the removal of the smaller fraction (≤3 cm) of material. The updated porosity is calculated using either Hazen's or the Kozeny-Carman equation as outlined by Bear (1972) through grain-size curve analysis. The resulting porosity of T1 (coarse) material is calculated to be ≥ 0.30 (Neuner et al. 2013). This model will use the conservative porosity of 0.30. During the construction of the Covered test pile, on-site measurements of the moisture content and the degree of saturation of the till material yielded a porosity of 0.20 (Pham 2013) which is the same as the porosity reported by Terzaghi et al. (1996) of a "glacial till, very-mixed grained".

3.6.6.3 Volumetric Moisture Content

The estimated field volumetric moisture content for waste rock at the Site was 0.06 according to Neuner et al. (2013). This moisture content is applied to the T1 and the T3 material. The T1 (coarse) material is assumed to be free-draining and can be approximated to be dry (Pham 2013). On-site measurements by Neuner et al. (2013) found that the capillary water maintained a degree of saturation of 90% in the till portion of the Covered pile. Given the known porosity of 0.20, this degree of saturation yields a till volumetric moisture content of 0.18.

3.6.6.4 Thermal Properties

Type 1 (Coarse)

Assuming the coarse fraction of the T1 material is dry (as by design), the bulk thermal conductivity and (volumetric) heat capacity were calculated according to the geometric and volumetric mean approach as outlined by Farouki (1981). This results in a heat capacity of 1.57 x 10^6 J/(m^3·K) and a bulk thermal conductivity of 0.71 W/(m·K) for the T1 (coarse) material (Pham 2013).

Till

For materials that are not dry, such as the till material, there are values representing both the frozen and unfrozen portions of the thermal conductivities and bulk heat capacities as these have different values depending on the thermal conditions.

The till material has a calculated frozen and unfrozen bulk heat capacity (see Equations 2-25, 2-26, and 2-27) based on the weight fraction of the mixture (at a volumetric moisture content of 0.18) according to Farouki (1981). Pham (2013) calculated these values to be 2.13 x 10^6 J/(m^3·K) and 2.51 x 10^6 J/(m^3·K) for the frozen and unfrozen volumetric heat capacities of till, respectively.

In-situ line heat source probes within the Covered test pile were able to provide an estimated thermal diffusivity of frozen till material (Pham 2013). The frozen thermal conductivity of till can be calculated using the thermal diffusivity (Equation 2-28) and the frozen volumetric heat capacity defined above. This results in a frozen thermal conductivity of 3.2 W/(m·K) and an unfrozen thermal conductivity of 2.9 W/(m·K) (Pham 2013).

T1 and T3

The thermal conductivities of the T1 and T3 rock were also calculated using in-situ line heat source probes. These thermal conductivity measurements were averaged over 5 years and calculated for each of the test piles. The thermal conductivities for the T1 and T3 test piles were 1.65 and 1.8 W/(m·K), respectively (Pham 2013). These probes were also able to provide an estimated unfrozen thermal diffusivity of the respective materials as detailed in Pham (2013). The unfrozen heat capacities of T1 and T3 materials were able to be calculated according to Equations 2-25, 2-26, and 2-27 using the unfrozen thermal conductivities above. The difference in the heat capacity of frozen and unfrozen water (and known volumetric moisture contents of 0.06) allows for a calculation of the frozen heat capacities as well. Pham (2013) calculated the frozen and unfrozen heat capacities for T1 to be 2.38 x 10^6 J/(m^3·K) and 2.40 x 10^6 J/(m^3·K), respectively. The T3 frozen and unfrozen volumetric heat capacities were calculated as slightly lower than the T1 values at 2.13 x 10^6 J/(m^3·K) and 2.15 x 10^6 J/(m^3·K), respectively.

3.6.6.5 Permeability

The permeability of both T1 and T3 waste rock was measured using air permeability probes at depths of up to 6 m as reported by Amos et al. (2009). The T1 and T3 materials had the same measured average permeability value of K = 2.0 x 10^{-9} m^2.

The permeability of the T1 (coarse) material is also estimated using either the either Hazen or Kozeny-Carman equations as outlined by Bear (1972). The value is estimated to be K $\geq$ 3 x 10^{-7} m^2 (Pham 2013). As the permeability can vary significantly depending on the heterogeneity of a material this parameter will be included in a sensitivity analysis. As described in Section 3.2, previous modelling by Pham (2013) used a range of permeabilities from K = 9 x 10^{-8} to K = 6 x 10^{-7} m^2 in the sensitivity analysis. A base value of K = 4 x 10^{-7} m^2 was chosen in previous modelling to be the optimum permeability (Pham 2013) and will be used for this model as a base case.

The till material was originally modelled with an assumed hydraulic conductivity (k) value of k = 5.0 x 10^{-9} m/s from values quoted from Hendry (1982) for small-scale fractures in a weathered till. This coordinates to a permeability of 5.0 x 10^{-16} m^2 according to Equation 2-13.

Table 3-3: Material property summary table (adapted from Pham (2013))

	Property	Value	Description	Source
	Type I (Coarse)			
ρ_s	Solids Density	2700 kg/m^3	Section 3.6.6.1	(Neuner 2009, Bailey 2013, Pham 2013)
η	Porosity	0.30	Section 3.6.6.2	(Bear 1972, Neuner et al. 2013)
ω_v	Volumetric Moisture Content	0.00 (Dry)	Section 3.6.6.3	(Pham 2013)
λ	Thermal conductivity	0.71 W/(m·K)	Section 3.6.6.4	(Farouki 1981, Pham 2013)
c_v	Volumetric heat capacity	1.57 x 10^6 J/(m^3·K)	Section 3.6.6.4	(Farouki 1981, Pham 2013)
K	Permeability	4 x 10^{-7} m^2 (to vary)	Section 3.6.6.5	(Pham 2013)
	Till			
ρ_s	Solids Density	2650 kg/m^3	Section 3.6.6.1	(Terzaghi et al. 1996, EBA 2004, BGC 2014)
η	Porosity	0.20	Section 3.6.6.2	(Terzaghi et al. 1996, Pham 2013)
ω_v	Volumetric Moisture Content	0.18 (at a S_r of 90%)	Section 3.6.6.3	(Neuner et al. 2013, Pham 2013)
λ_{fr}	Frozen thermal conductivity	3.2 W/(m·K)	Section 3.6.6.4	(Pham 2013)
λ_{uf}	Unfrozen thermal conductivity	2.9 W/(m·K)	Section 3.6.6.4	(Pham 2013)
c_v	Frozen volumetric heat capacity	2.13 x 10^6 J/(m^3·K)	Section 3.6.6.4	(Farouki 1981, Pham 2013)
c_v	Unfrozen volumetric heat capacity	2.51 x 10^6 J/(m^3·K)	Section 3.6.6.4	(Farouki 1981, Pham 2013)
K	Permeability	5 x 10^{-16} m^2	Section 3.6.6.5	Hendry (1982)
	Type III			
ρ_s	Solids Density	2700 kg/m^3	Section 3.6.6.1	(Neuner 2009, Bailey 2013, Pham 2013)
η	Porosity	0.25	Section 3.6.6.2	(Neuner et al. 2013)
ω_v	Volumetric Moisture Content	0.06	Section 3.6.6.3	(Neuner et al. 2013)
λ	Thermal conductivity	1.8 W/(m·K)	Section 3.6.6.4	(Pham 2013)
c_v	Frozen volumetric heat capacity	2.13 x 10^6 J/(m^3·K)	Section 3.6.6.4	(Pham 2013)
c_v	Unfrozen volumetric heat capacity	2.15 x 10^6 J/(m^3·K)	Section 3.6.6.4	(Pham 2013)
K	Permeability	2 x 10^{-9} m^2	Section 3.6.6.5	Amos et al. (2009)
	Type I (All Fractions)			
ρ_s	Solids Density	2700 kg/m^3	Section 3.6.6.1	(Neuner 2009, Bailey 2013, Pham 2013)
η	Porosity	0.25	Section 3.6.6.2	(Neuner et al. 2013)
ω_v	Volumetric Moisture Content	0.06	Section 3.6.6.3	(Neuner et al. 2013)
λ	Thermal conductivity	1.65 W/(m·K)	Section 3.6.6.4	(Pham 2013)
c_v	Frozen volumetric heat capacity	2.38 x 10^6 J/(m^3·K)	Section 3.6.6.4	(Pham 2013)
c_v	Unfrozen volumetric heat capacity	2.40 x 10^6 J/(m^3·K)	Section 3.6.6.4	(Pham 2013)
K	Permeability	2 x 10^{-9} m^2	Section 3.6.6.5	Amos et al. (2009)

3.7 Finite Element Analysis (FEA)

FEM is a numerical technique that uses Finite Element Analysis (FEA) to solve complex mathematical and engineering problems. For example, a given problem that has static and dynamic properties can be broken up into a known number (finite) of pieces (elements). Each individual element can then have its own properties that may still be dynamic but will have a smaller possible range of values. Through partial differentiation these elements can be solved over a given time step. As each element is surrounded by other elements, the boundary conditions of each are linked to their adjacent elements. Through this process a complex problem can be solved more accurately than if the entire object was defined as a single element with averaged properties. The group of elements for a given simulation is called a mesh, with the length of an element representing a mesh size.

3.7.1 Mesh Size

As it may be expected, as a problem is broken down into smaller and smaller elements (i.e., a smaller mesh size) a solution would become more and more accurate as the intricacies of a simulation can be captured more effectively. The downside to this is that is becomes computationally expensive, taking longer and longer to run a simulation. This is an important factor to consider and ideally a given problem should be broken down into enough elements such that an accurate solution can be found but not so many such that computational time is wasted. A recommended way to determine this optimum mesh size is to conduct a mesh refinement study, where a mesh size is gradually decreased for a simulation to determine the point where the solution is no-longer mesh dependent, i.e., the results no longer change as the mesh size decreases. Something to note is that a mesh is often not consistent within a given domain and subdomains that are expected to be more complex may require smaller mesh sizes.

3.7.1.1 Mesh Refinement Study

A mesh refinement study (or mesh convergence study) was conducted in order to determine the optimum mesh sizing. The chosen controlling mesh parameter is the number of mesh nodes along the upper surface of the model which may also be defined as the mesh distribution. This value directly correlates to the mesh sizing as more nodes along the surface will result in a smaller mesh size for the upper layer. In addition to the number of nodes, an input of a maximum and minimum mesh size is required which will further limit the mesh design.

Prior to performing a mesh refinement study, it is good practice to consider the computations and accuracy that are required within different regions of the model. Setting the entire mesh size to

be the same across the entire domain may result in unnecessary computational time should only one subdomain require such a precise mesh. For this simulation, most of the heat transfer and fluid flow interactions occur in the T1 (coarse) layer, particularly during the generation of convection cells. The mesh should be the finest in this region to capture this. The latent heat layer would not require as fine of a mesh as the T1 (coarse) material and therefore the number of nodes could decrease. Finally, the T3 material could have even larger elements than the till material and therefore the node distribution can be decreased further. Following this process, this model defines the number of nodes of the upper boundary of the T1 (coarse) material as 2 times and 4 times larger than the nodes in the upper boundaries of the till and T3 areas, respectively. The mesh refinement study can then focus on adjusting the number of nodes at the top of the structure and the rest of the mesh will adjust accordingly.

The number of nodes for the upper boundary is varied between 5 and 400. The maximum annual temperature from each iteration is measured at the same location (top of the till layer) over 100 years as presented in Figure 3-7. As seen in this figure a node value of 125 or greater does not significantly alter the resulting temperatures and the values are overlapping. The computational time summary for each iteration is presented in Table 3-4. While a mesh distribution of 125 nodes is sufficient, further simulations will use a mesh distribution of 200 instead. This is because the computational time between 125 nodes (18m 06s) and 200 nodes (31m 40s) is not too large and an increase in nodes allows further flexibility during the sensitivity analyses (Section 4.1). Should the geometry be changed in the sensitivity analysis the mesh distribution of 125 nodes may no longer be sufficient. In this way a chosen node value of 200 may act as a buffer for this process.

The maximum and minimum mesh sizes for each subdomain were then analyzed to further refine the mesh. This process also focused on balancing computational time and accuracy and followed the same process as the node optimization. The resulting maximum and minimum mesh sizes for each subdomain are shown in Table 3-5. The T1 subdomain resulted in a maximum and minimum value of 3 m and 0.1 m, respectively. The till and T3 subdomain optimization resulted in 5 m and 0.5 m for maximum and minimum sizes, respectively. The resulting visual representation of these mesh parameters is seen in Figure 3-8.

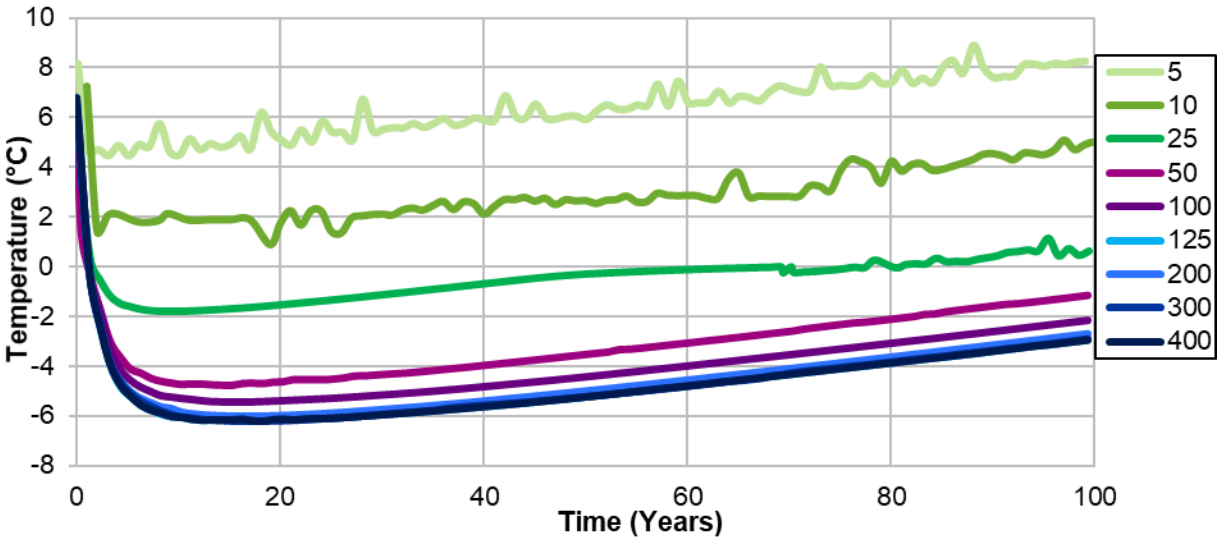

Figure 3-7: Mesh refinement analysis for distribution between 5 and 400 nodes

Table 3-4: Mesh node (distribution) optimization results

Mesh Interval (# of nodes)	Node Spacing (Model Width = 30 m)	Computation Time (hh:mm:ss)	Adequate Mesh Interval?
5	6 m	00:05:33	No
10	3 m	00:05:40	No
25	1.2 m	00:05:52	No
50	0.6 m	00:10:04	No
100	0.3 m	00:16:12	No
125	0.24 m	00:18:06	Yes
150	0.20 m	00:23:14	Yes
175	0.17 m	00:30:55	Yes
200	0.15 m	00:31:40	Yes
300	0.10 m	00:50:00	Yes
400	0.075 m	01:08:23	Yes

Table 3-5: Mesh maximum and minimum element size optimization

Number of Nodes (Upper boundary)	Maximum Mesh Size	Minimum Mesh Size
T1 Subdomain		
200 nodes	3 m	0.1 m
Till Subdomain		
100 nodes	5 m	0.5 m
T3 Subdomain		
50 nodes	5 m	0.5 m

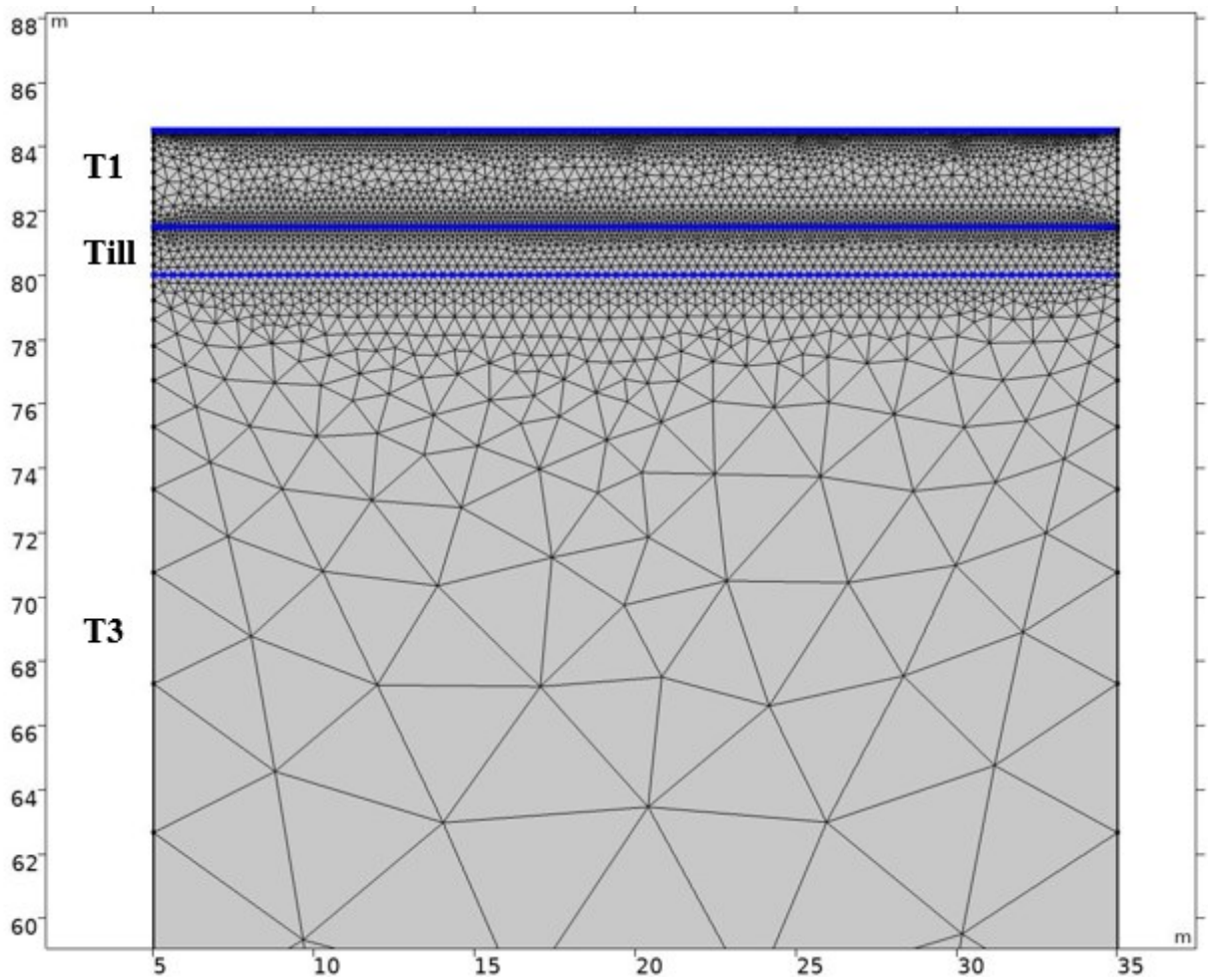

Figure 3-8: Mesh schematic design as per mesh refinement analysis (upper boundary mesh nodes = 200)

3.8 Model Width Sensitivity

A sensitivity analysis of the model width is run to ensure that the chosen width of 30 m is sufficient for modelling purposes. Model widths between 5 and 60 m are analyzed to determine the minimum width required to capture the convective-cooling effects. In order to assess the impacts of solely changes in model width, the mesh sizing (technically defined according to the number of nodes across the upper boundary) will be adjusted to maintain the same sizing for each analysis. This alters the number of nodes to maintain the same mesh sizes chosen in Section 3.7.1.1 (200 nodes/30 m).

The results of this analysis are presented in Figure 3-9 which demonstrates the maximum annual temperature calculated at the top of the till over 100 years. As seen in this figure a mesh size of 10 m and above is sufficient to ensure the results are not width dependent. The resulting model width of 30 m is therefore sufficient and will be used for remaining analyses.

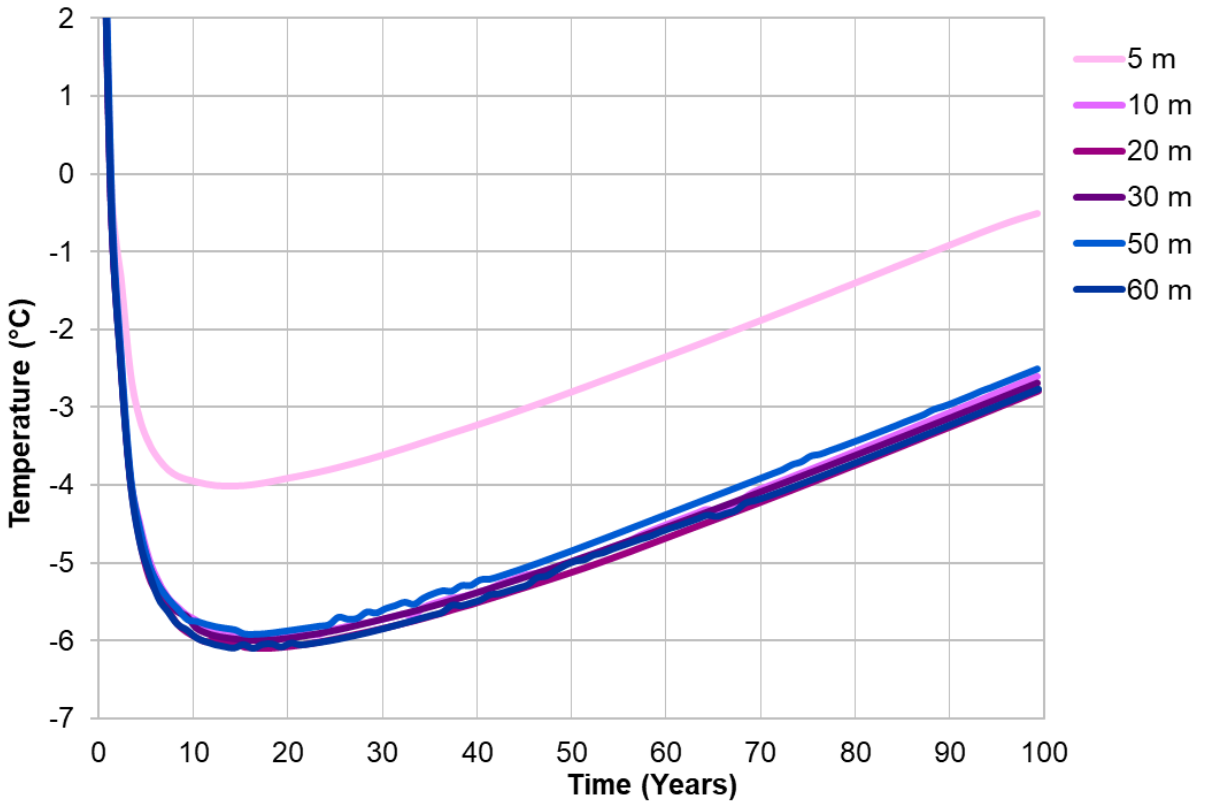

Figure 3-9: Model width sensitivity over 100 years

3.9 Step Size

The step size for a simulation is the time that is calculated for and displayed in the results. If a step size is too large the time-dependent variables such as surface temperature (Equation 3-5) may not capture the key time steps that represent the maximum and minimum temperatures on an annual basis. In addition, if the step size is not adequately small, the results may result in too much scatter within the data. The step size iterations range between 0.001 years (0.4 days) and 1 day. The maximum annual temperature from each iteration is measured at the same location (top of the till layer) over 100 years as presented in Figure 3-10. The corresponding computational times are listed in Table 3-6.

As seen in this figure, a step size of 0.01 years (3.7 days) or smaller all produce the same results without scatter. This makes 0.01 years the optimum step size as it is the least computationally expense without compromising results.

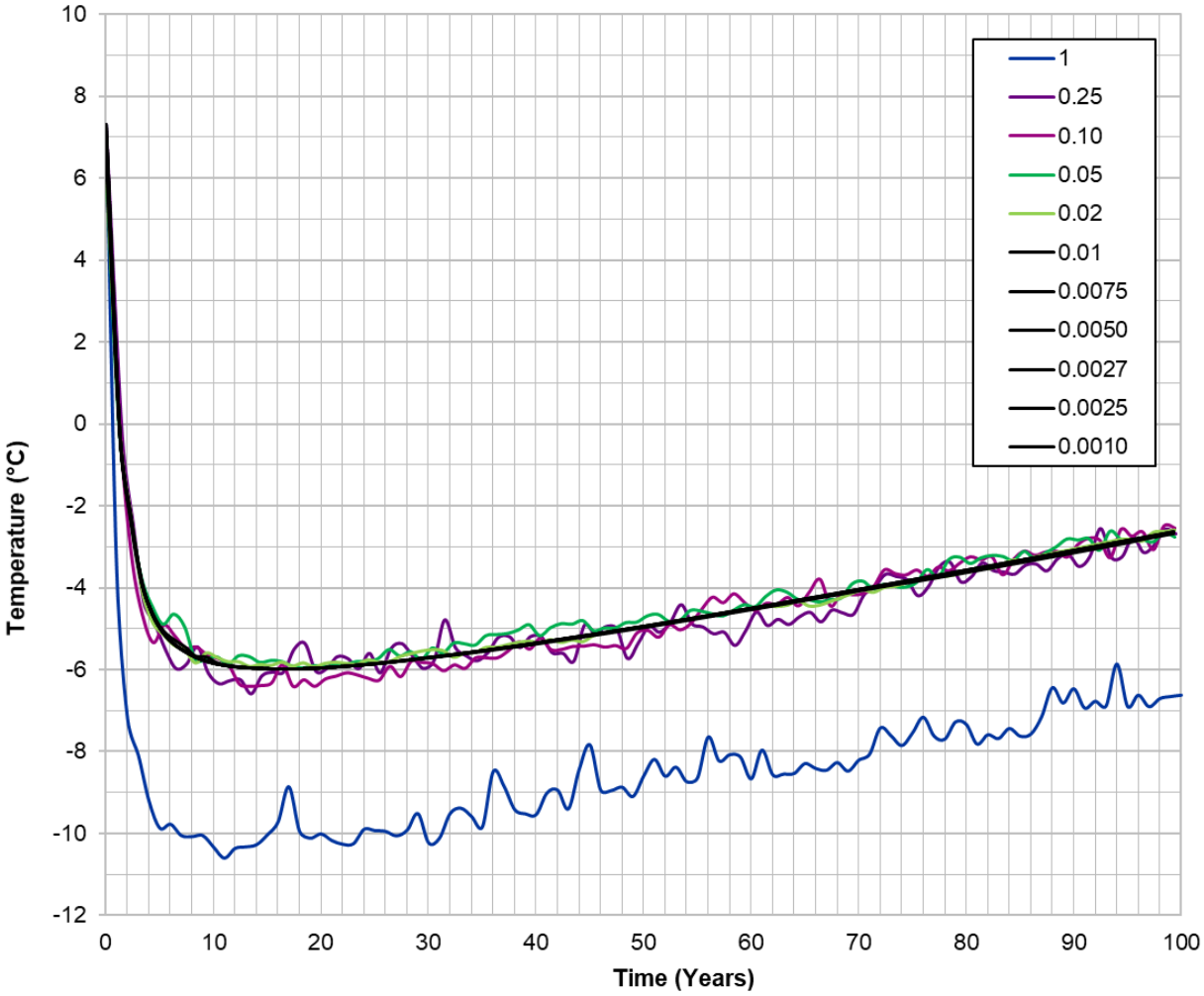

Figure 3-10: Step size sensitivity over 100 years

Table 3-6: Step size study summary

Step Size (years)	Step Size (days)	Computation Time (hh:mm:ss)	Adequate Step Size?
1	365.25	00:19:31	No
0.25	91.3	00:19:46	No
0.1	36.5	00:19:46	No
0.05	18.3	00:21:11	No
0.02	7.3	00:24:06	No
0.01	3.7	00:31:17	Yes
0.0075	2.7	00:41:02	Yes
0.0050	1.8	01:01:16	Yes
0.0027	1	01:48:38	Yes
0.0025	0.9	01:59:38	Yes
0.0010	0.4	04:46:07	Yes

3.10 Model Benchmarking

Before moving forward with the current model settings, they must be verified against previous modelling cases. This comparison is also known as benchmarking. Case 3, as described in Section 3.2.5 for Pham (2013)'s work, is used as the comparison case for this benchmark study.

A preliminary verification of correct model functionality is to visually inspect the temperature gradient throughout the simulation. The simulation mesh outline is presented in Figure 3-11a for reference purposes. Temperature profiles for the rebuilt benchmark study are presented at the beginning (time = 0 years, Figure 3-11b) and at the end of the simulation (time = 100 years, (Figure 3-11c). The profiles demonstrate the lower 80 m of PAG material which begins at approximately 0°C or warmer and ends at temperatures below freezing at the end of the simulation. This figure also demonstrates how the temperatures at depth of the model are unchanging which verify the boundary conditions outlined in Section 3.6.2.

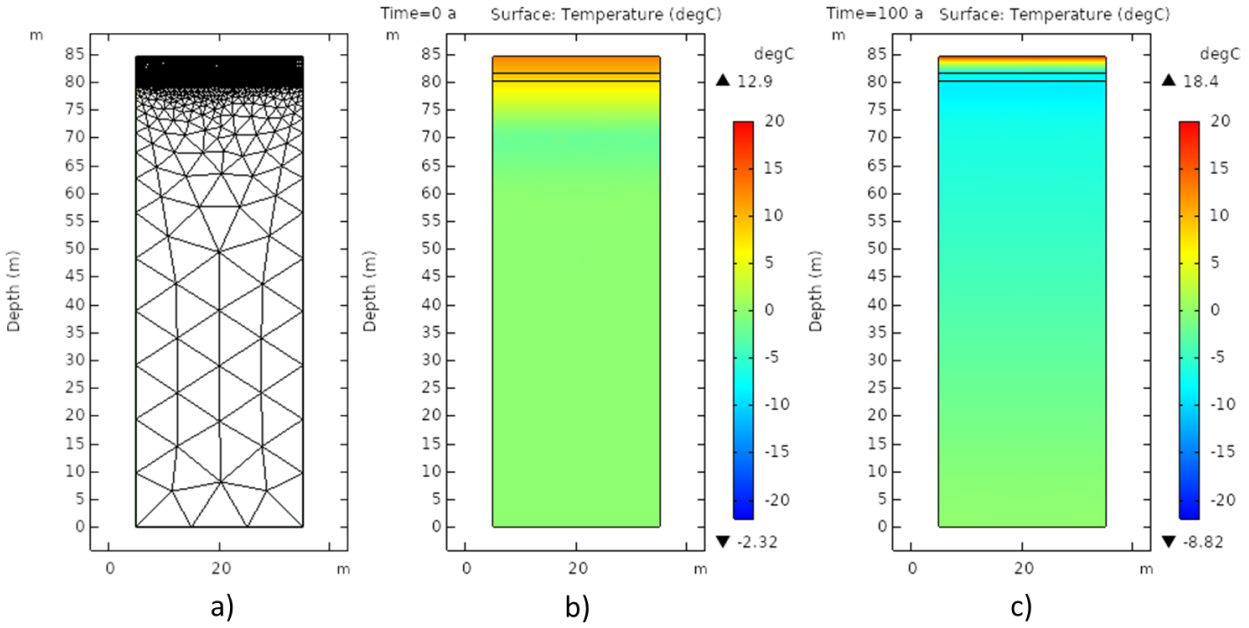

Figure 3-11: Model Benchmarking Visualization (Temperature Change)
(a) Mesh diagram for reference, (b) Temperature gradient at beginning of the study (time = 0 years), (c) Temperature gradient at end of the study (time = 100 years)

The benchmark results also demonstrate the heat transport processes that would occur during each season. The cross-section focuses on the upper layers only (T1 (coarse) and till)) with the mesh distribution presented in Figure 3-12a for reference. Figure 3-12b presents the winter temperature gradient after 10 years (time = 10.52 years ~January. This figure includes stream lines of velocity coordinating to fluid flow of established natural convection cells. Figure 3-12c presents a summer temperature gradient after 10 years (time = 10.02 years, ~July). Stream lines

are less organized and no longer present convection cells, but rather a more linear heat transfer due to conduction. These results demonstrate that this model recreation is able to capture the key thermal processes of the convective model.

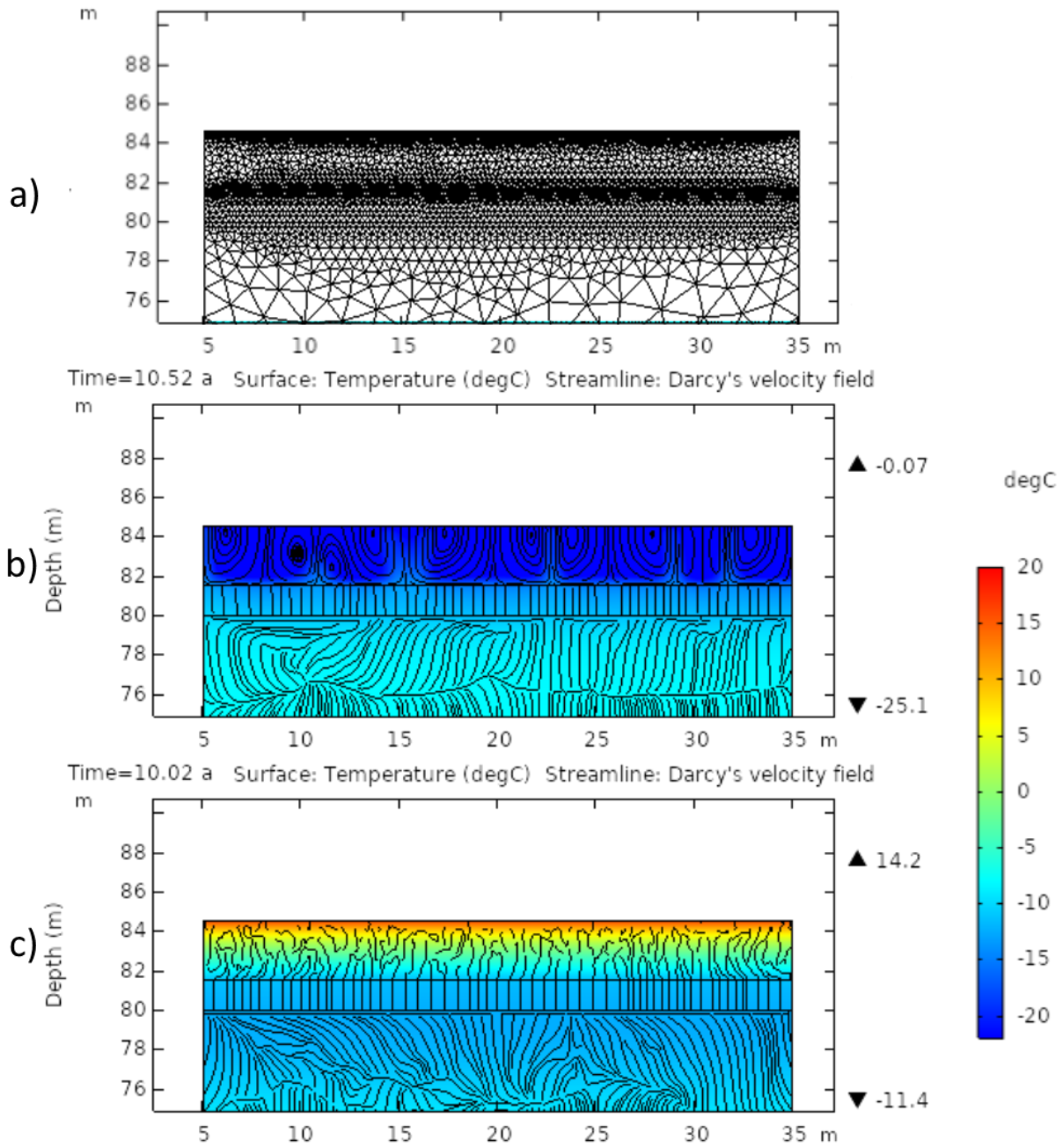

Figure 3-12: Model Benchmarking Visualization (Convection Cells)
(a) Mesh diagram for reference, (b) Winter convection cells, (c) Summer conduction only

Pham (2013) plotted the maximum and minimum temperatures that were seen at the top of till and top of T3 layer over 100 years (July 2010 to July 2110). The two temperature locations are

illustrated in Figure 3-13 with the corresponding benchmark prescription of 1.5 m of till overlain by 3.0 m of T1 (coarse) material.

The modelling environment and inputs defined in Section 3.3 to 3.9 are used to produce the benchmark case. These results are compared to Pham (2013)'s results at the top of the till and the top of T3 in Figure 3-14 and Figure 3-15, respectively. For both figures the difference between the maximum values for both the benchmark simulation and the data provided from Pham (2013) is minimal. The minimum temperature lines however show a larger discrepancy of temperatures, the largest of which happens at around year 11 (2021, $\Delta T = 1.3°C$) for the top of till and year 15 (2025, $\Delta T = 0.9°C$) for the top of T3. These discrepancies then decrease over time and by year 100 (2110) the top of till has a $\Delta T = 0.2°C$ and the top of T3 has a $\Delta T = 0.6°C$. The discrepancies may be a result of the assumptions for initial temperature of this case as well as some material properties were required as described in Sections 3.6.3 and 3.6.4, respectively.

The resulting trends and overall maximum temperatures provided in Figure 3-14 and Figure 3-15 show that the key components of the original simulations described by Pham (2013) have been adequately reproduced and will serve as a functional basis for future analysis.

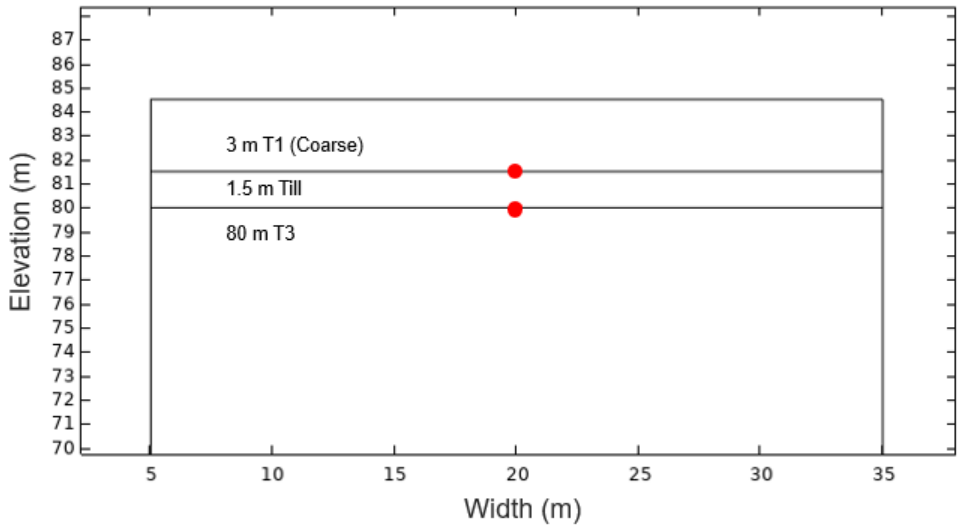

Figure 3-13: Modelling temperature locations for benchmarking study

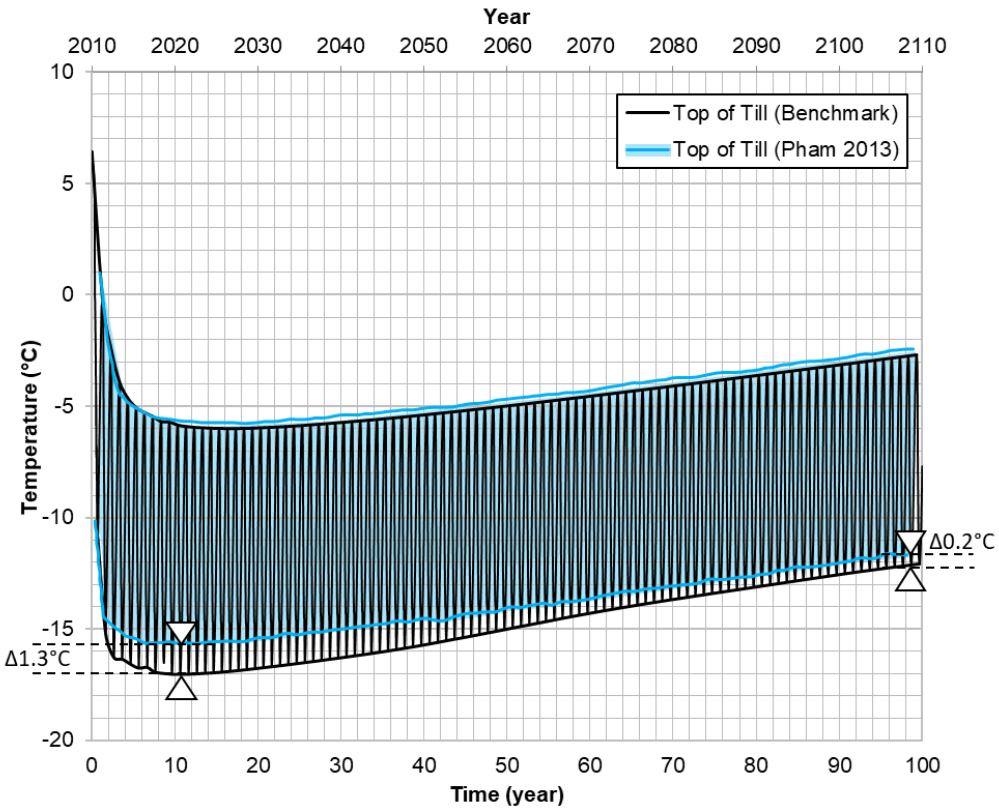

Figure 3-14: Till benchmark temperatures against Pham (2013)

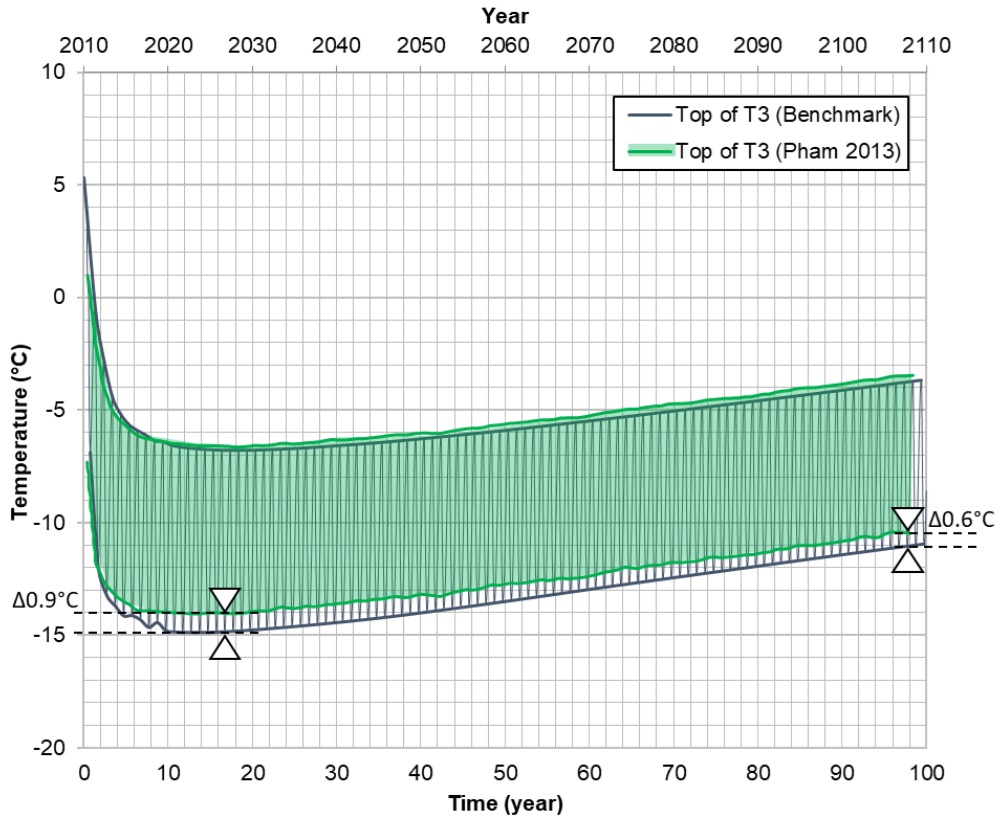

Figure 3-15: T3 benchmark temperatures against Pham (2013)

4 Model Analysis

This chapter will focus on the analysis of the model given the successful benchmarking conducted against Pham (2013)'s results in Section 3.10. The baseline condition for the sensitivity of this model will include the same soil prescription as above: 3.0 m of T1 (coarse) and 1.5 m of till material overlying the 80 m of T3 waste rock. In addition, the alternative soil cover options of using only T1 (coarse) material or only T1 material will be investigated.

4.1 Sensitivity Analysis

A sensitivity analysis can demonstrate how changing a model input parameter may impact model results. This has a few different purposes, such as demonstrating the robustness of a model as well as to show the functional range of a given parameter that will maintain acceptable results. The simplest form of a sensitivity analysis is to change one parameter while keeping all other model definitions the same. By running multiple simulations while adjusting one parameter the results will demonstrate the impact of these parameter changes. For this research there are a few parameters that have the largest uncertainty due to their heterogeneity in the field (volumetric moisture content of till, permeability of T1 (coarse) material) or possible range of values (annual temperature increase due to climate change). These parameters will be the focus of this sensitivity analysis.

A successful soil cover system will maintain the potentially acid-generating (PAG) T3 material under frozen conditions for 100 years. In lieu of measuring the top of the T3 layer, this study will focus on the temperature of the latent heat layer (i.e., top of till). One of the most uncertain points of the model framework is during the phase change of the till from frozen to unfrozen. In general, the physics surrounding water as it approaches a phase change can be complicated, and while this simulation does account for the expected transition behaviour between -1°C and +1°C it does bring in some uncertainty in temperatures between these bounds. With these considerations, the sensitivity analyses for the variables that follow will use a maximum temperature of -1°C for the top of the till (seen in Figure 3-13) after 100 years as the "successful" or "passing" condition of a sensitivity check.

4.1.1 Water Content

Pham (2013) notes that the moisture content of the waste rock has an impact on thermal conductivity – the higher the moisture content, the higher the thermal conductivity. The latent heat layer (the till layer) is an important part of the cover system. As its functionality is highly dependent

on maintaining a high moisture content it is important to run a sensitivity analysis on the cover system assuming a range of volumetric moisture contents for the till material.

Parameters for thermal conductivity and heat capacity for till were originally defined based on known measurements at one given degree of saturation and volumetric moisture content (S_r = 90%, ω_V = 0.18). Conducting a sensitivity analysis on the volumetric moisture content means that the inputs for both thermal conductivity and heat capacity must also be dynamic as this is how the volumetric moisture content is applied to this model.

The permeability of the till is not adjusted for this analysis. While a change in the moisture content of a soil will change the ability for air to flow through the till material the analysis of this moves into the realm of unsaturated soil mechanics. As material within the till layer is considered primarily fine-grained the heat transfer will be primarily conductive. The permeability changes associated with an increase or decrease in moisture content will not impact heat transfer through the system in a meaningful way and therefore this adjustment is unnecessary.

4.1.1.1 Thermal Conductivity

The unfrozen and frozen thermal conductivities of till can be defined according to their degree of saturation as outlined by Côté and Konrad (2005) in Section 2.5.1.1. Key parameters for these formulae are provided below in Table 4-1, with the thermal conductivity equations summarized in Table 4-2 established from the original source of Côté and Konrad (2005). The resulting combined formulae for the unfrozen (Equation 4-1) and frozen (Equation 4-2) thermal conductivity is a function of Equations 2-19, 2-20, and 2-22 and Equations 2-19, 2-21, and 2-23, respectively. The value used for the solid portion of the material, λ_s = 3.86 W/(m·K) , was back-calculated using the initial water content of 0.18 (Pham 2013). This thermal conductivity is within the reported range of granite, λ_s = 1.7 to 4.0 W/(m·K) (Andersland and Ladanyi 2004).

Table 4-1: Assumed values for estimating frozen and unfrozen thermal conductivities of till

Parameter	Symbol	Value	Unit	Source
Thermal conductivity of air	λ_a	0.026	W/(m·K)	(Andersland and Ladanyi 2004)
Thermal conductivity of water (at 0°C)	λ_w	0.56	W/(m·K)	(Andersland and Ladanyi 2004)
Thermal conductivity of ice (at 0°C)	λ_i	2.21	W/(m·K)	(Andersland and Ladanyi 2004)
Thermal conductivity of solid particles	λ_s	3.86	W/(m·K)	Assumed based on data from (Pham 2013)
Porosity of Till	η	0.20	1	(Terzaghi et al. 1996, Pham 2013)

Table 4-2: Recall thermal conductivity equations from Section 2.5.1.1

λ	Equation	#	Section
Dry	$\lambda_{dry} = \lambda_s^{(1-\eta)^{0.59}} \lambda_a^{\eta^{0.73}}$	2-19	2.5.1.1
Saturated, unfrozen	$\lambda_{sat} = {\lambda_s}^{1-\eta} {\lambda_w}^{\eta}$	2-20	2.5.1.1
Saturated, frozen	$\lambda_{sat} = {\lambda_s}^{1-\eta} {\lambda_i}^{\eta}$	2-21	2.5.1.1
Normalized, unfrozen	$\lambda_r = \frac{4.7 S_r}{1 + 3.7 S_r}$	2-22	2.5.1.1
Normalized, frozen	$\lambda_r = \frac{1.8 S_r}{1 + 0.8 S_r}$	2-23	2.5.1.1
Thermal Conductivity	$\lambda = (\lambda_{sat} - \lambda_{dry})\lambda_r + \lambda_{dry}$	2-24	2.5.1.1

Unfrozen $$\lambda_{till(uf)} = \left({\lambda_s}^{1-\eta} {\lambda_w}^{\eta} - \lambda_s^{(1-\eta)^{0.59}} \lambda_a^{\eta^{0.73}}\right) \frac{4.7 \frac{\omega_v}{\eta}}{1 + 3.7 \frac{\omega_v}{\eta}} + \lambda_s^{(1-\eta)^{0.59}} \lambda_a^{\eta^{0.73}} \quad \textbf{4-1}$$

Frozen $$\lambda_{till(fr)} = \left({\lambda_s}^{1-\eta} {\lambda_i}^{\eta} - \lambda_s^{(1-\eta)^{0.59}} \lambda_a^{\eta^{0.73}}\right) \frac{1.8 \frac{\omega_v}{\eta}}{1 + 0.8 \frac{\omega_v}{\eta}} + \lambda_s^{(1-\eta)^{0.59}} \lambda_a^{\eta^{0.73}} \quad \textbf{4-2}$$

4.1.1.2 Heat Capacity

The heat capacity of the till relies on a simpler formula than the thermal conductivity. Recall Equation 2-26 which defines the (volumetric) heat capacity (c_v) as a function of a materials volume fraction and soil volume of solids, water, ice, and air. The defined values of heat capacity are provided in Table 4-3.

Table 4-3: Heat capacity properties for till volumetric water content sensitivity

Value	Equation (or value)			#	Section
c_v	$c_v = c_{v,s} x_s + c_{v,w} x_w + c_{v,i} x_w + c_{v,a} x_a$			2-26	2.5.1.2
Parameter	**Symbol**	**Value**	**Unit**	**Reference**	
Volumetric heat capacity of air	$c_{v,a}$	1.25	(kJ/(m^3·K)	(Andersland and Ladanyi 2004)	
Volumetric heat capacity of water	$c_{v,w}$	4218	(kJ/(m^3·K)	Andersland and Ladanyi 2004)	
Volumetric heat capacity of ice	$c_{v,i}$	1881	(kJ/(m^3·K)	Andersland and Ladanyi 2004)	
Volumetric heat capacity of solid	$c_{v,s}$	2214	(kJ/(m^3·K)	Calculated based on Pham (2013)	

4.1.1.3 Results

The volumetric water content of till is adjusted between $\omega_v = 0.00$ and $\omega_v = 0.20$ which is equal to degrees of saturations of $S_r = 0$ and $S_r = 100\%$, respectively. The maximum annual temperatures of both the top of the till and top of the T3 layers are presented in Figure 4-1 and Figure 4-2, respectively. The time duration of interest is still 100 years, despite the fact that these figures include iterations which were extended to 200 years. The maximum temperatures recorded after 100, 150, and 200 years are recorded for the top of the till and top of the T3 layers in Table 4-4. This maximum temperature considers the timeframe between year 99 to year 100 (2114-2115), year 149 to year 150 (2164-2165), and year 199 to year 200 (2214-2215).

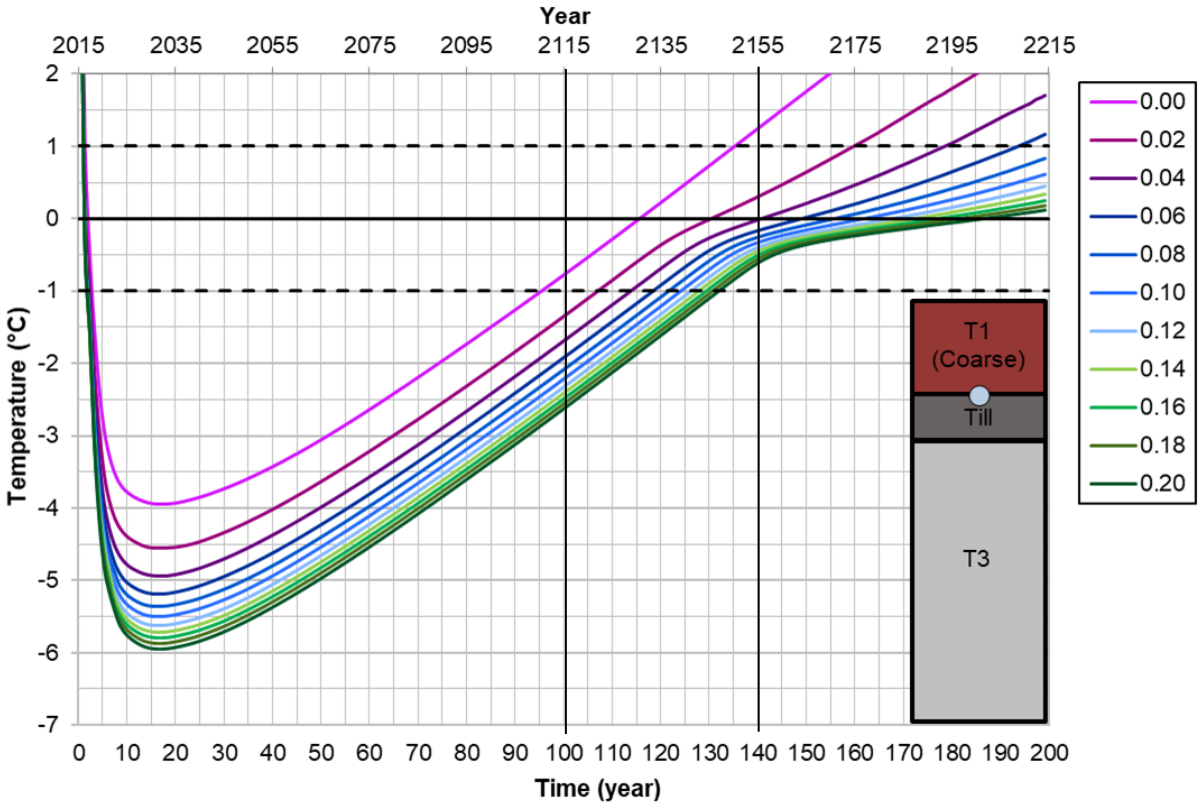

Figure 4-1: Maximum annual temperatures at the top of till at varying ω_v of till

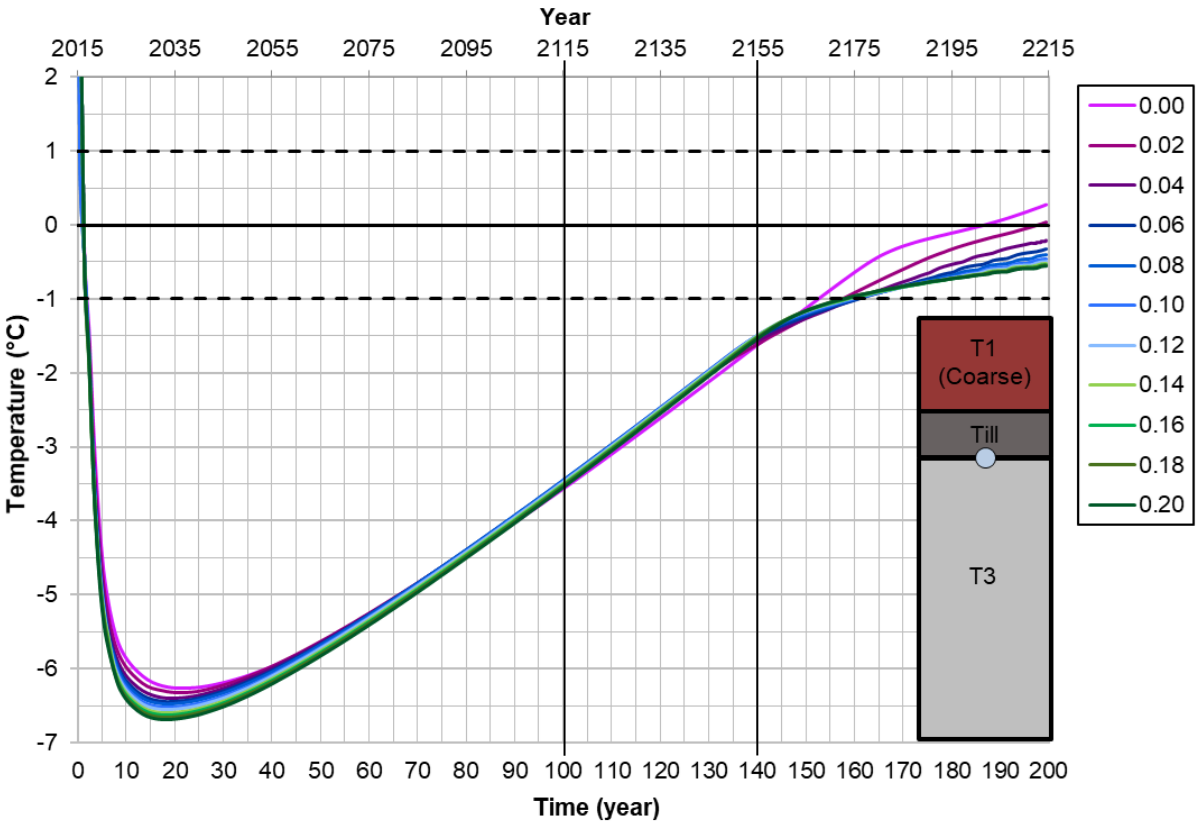

Figure 4-2: Maximum annual temperatures at the top of T3 at varying ω_v of till

Table 4-4: Temperatures at top of till and top of T3 after 100, 150, and 200 years

Legend	$T_{(max)}$	≤-1°C	-1°C to 0°C		≥0°C	
Top of	**t = 99 – 100 years (2114 – 2115)**		**t = 149 – 150 years (2214 – 2215)**		**t = 199 – 200 years (2214 – 2215)**	
$\omega_{v(till)}$	**Till**	**T3**	**Till**	**T3**	**Till**	**T3**
0.00	-0.82	-3.60	+1.72	-1.16	+4.11	+4.11
0.02	-1.39	-3.52	+0.62	-1.28	+2.66	+2.66
0.04	-1.72	-3.49	+0.20	-1.27	+1.71	+1.71
0.06	-1.95	-3.48	+0.01	-1.25	+1.17	+1.17
0.08	-2.12	-3.49	-0.10	-1.22	+0.83	+0.83
0.10	-2.25	-3.50	-0.17	-1.20	+0.61	+0.61
0.12	-2.36	-3.51	-0.22	-1.19	+0.45	+0.45
0.14	-2.45	-3.53	-0.27	-1.18	+0.34	+0.34
0.16	-2.53	-3.54	-0.30	-1.18	+0.25	+0.25
0.18	-2.60	-3.56	-0.33	-1.18	+0.18	+0.18
0.20	-2.66	-3.58	-0.36	-1.18	+0.12	+0.12

4.1.1.4 Discussion

At the top of the till (Figure 4-1), it is seen that increasing values of till volumetric moisture content results in a deeper frost aggradation effect within the first 15 years. After this point (around year 2030), the temperature at the top of the till increases roughly linearly in each case. Focusing on the temperature at the top of the till after 100 years, all volumetric moisture contents of till are able to maintain temperatures colder than -1°C except for the completely dry case (ω_v = 0.00, S_r = 0%). This case achieves a maximum temperature of -0.82°C at the top of the till during year 100.

At the top of the T3 material (Figure 4-2) the impact of the variations of till volumetric moisture content are much more diminished than at the top of the till. While this figure also presents the difference in frost aggradation around approximately year 15 these temperature variations are small. Furthermore, the temperature range between the sensitivity cases diminishes quickly, and the data maintains comparable temperatures until year 100 (2115). In fact, as demonstrated in Table 4-4, the variations in till are all within 0.2°C of each other. Extending the time frame sees the impacts of a variable till volumetric moisture content which presents as earlier thawing of the till layer, particularly for values of 0.00 and 0.02.

Initial inspection of these results may draw a conclusion that the volumetric moisture content of till must be at least 0.02 and the till and T3 material will remain frozen after 100 years. One consideration however is to analyze the temperatures past this point to observe what happens as the till material begins to thaw. When these iterations are extended until year 2215 (200 years total) the latent heat effect of the till is evident. With increasing values of till ω_v, the latent heat effect extends the thawing time and therefore maintains the till and T3 material frozen for longer. During the 149-150-year time frame a value of $\omega_v \geq 0.08$ maintains temperatures at the top of till below 0°C. This indicates that although a volumetric moisture content of 0.02 is satisfactory, a value of 0.08 or larger significantly postpones the thawing front. As a result, this research recommends a minimum till value of ω_v = 0.08. At a till ω_v = 0.08 the temperatures at the top of the till and top of the T3 materials are predicted to be -2.12°C and -3.49°C, -0.10°C and -1.22°C, and +0.83°C and -0.40°C, for years 100, 150, and 200 years, respectively.

The extension of the time frame past 100 years also allows for the verification of the temperature processes occurring near 0°C. As demonstrated in Figure 4-1, as the temperatures at the top of the till layer begins to increase and approach 0°C the linear trend that occurred from years 30 to 120 no longer exists. The temperatures presented are the maximum temperatures during each

year and therefore these represent the summer temperatures only. A more detailed look maximum and minimum values of a given moisture content is warranted, as presented below.

A look into the effects after an additional 100 years, up to the year 2315, is also evaluated for a till value of $\omega_v = 0.18$ as seen in Figure 4-3. This figure presents the temperature during the 300-year period at the top of the till and top of the T3 material. As seen in this figure, as the simulation approaches 0°C in the warmer (summer) months the linear trend described above begins to flatten as the temperatures increase. The warming temperatures in the summer are not enough to overcome the latent heat required to melt the frozen water content within the till. In addition, the conductive heat transfer that warms the T1 (coarse) layer in the summer is negated as a result of the much more efficient winter convective-cooling effects. Over time, as the temperatures in the winter (colder) months begin to approach 0°C and convective cooling no longer occurs, the latent heat required to thaw the till is reached. The temperatures then return to their linear increase over time with the annual temperature increase according to the input of climate change. This figure demonstrates how the model is able to successfully account and represent the generally complicated nature of thawing material.

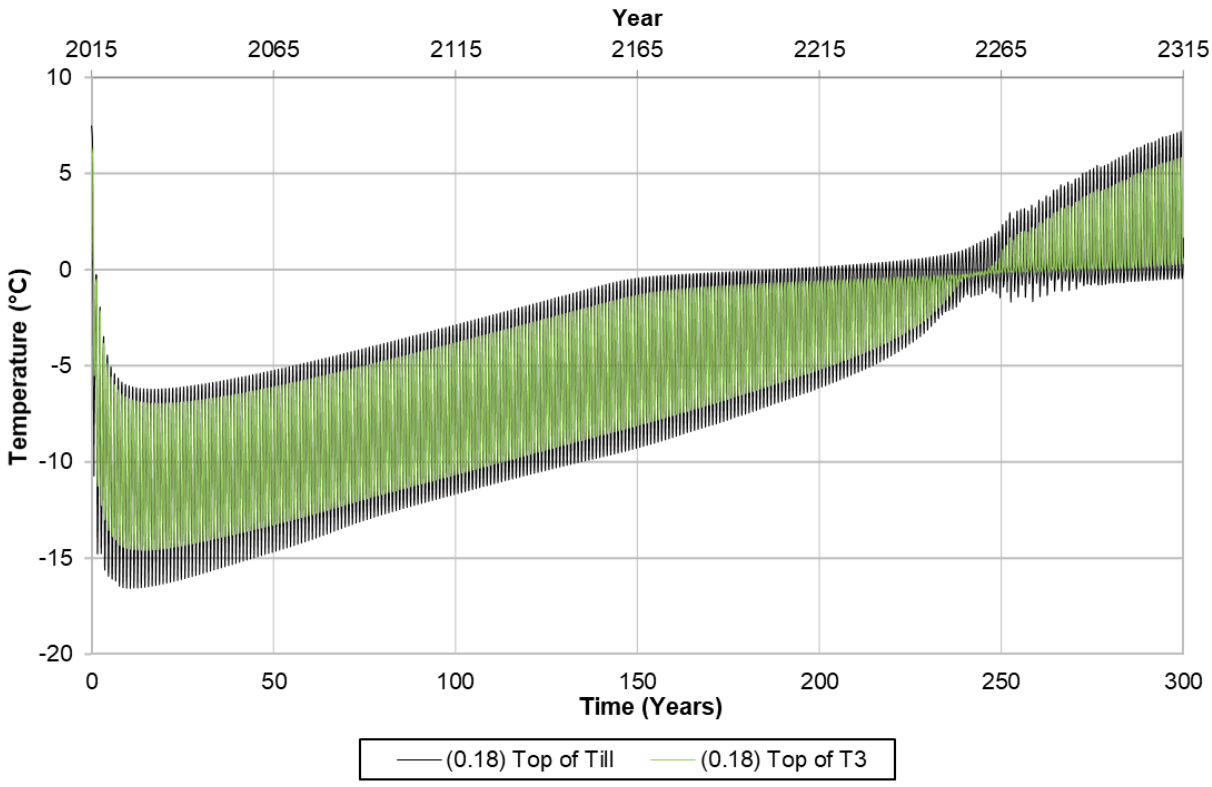

Figure 4-3: Long term analysis of various till ω_v over 100 years

4.1.2 Permeability of Upper Layer – Type 1 (Coarse) Material

As the T1 (coarse) material is engineered from a heterogeneous waste material there may be variations in the permeability. The limitations involved with modelling a heterogeneous material as homogeneous are described in Section 3.3.7. In addition, as convective cooling depends on the increased permeability that comes with the filtering of the T1 waste rock, the permeability can greatly alter the thermal regime and resulting success of a soil cover system. As mentioned in Section 3.2.5, Pham (2013) performed a sensitivity analysis on the T1 (coarse) permeability for the Case 3 Covered test pile design. This analysis used a range of permeabilities from K = 9 x 10^{-8} m^2 to K = 6 x 10^{-7} m^2 and found a permeability of K = 4 x 10^{-7} m^2 to be satisfactory for the T1 (coarse) material to induce convective cooling. This value was set as the base case for this research as well. This sensitivity analysis will further identify the range of values that can initiate convective cooling as the geometry has been updated to the full-scale WRSA-NCRP.

4.1.2.1 Critical Rayleigh Value

The critical Rayleigh value (Ra_c) plays an important role in confirming the success of induced natural convection. The term is defined in Section 2.5.3.3 and Nield and Bejan (2006) provide critical Rayleigh values according to their boundary conditions. The soil cover boundary conditions for this research are defined in Section 3.6.2 which have an upper boundary that is open to the atmosphere and the lower boundary set on impermeable bedrock. This scenario (permeable upper boundary, impermeable lower boundary, both conductive) aligns with a critical Rayleigh value of 27.1 (Nield and Bejan 2006). Results are therefore expected to show different thermal conditions at or near this value, with primarily conductive heat transfer occurring at values lower than 27.1 and primarily convective heat transfer above this. The sensitivity analysis for the permeability and corresponding Rayleigh values are analyzed in comparison to the critical value. An upper boundary for the Rayleigh value may also be found as discussed in Section 2.5.4.1.

4.1.2.2 Results

The permeability of the T1 (coarse) material is varied between K = 4 x 10^{-6} m^2 and K = 7 x 10^{-8} m^2 with results presented in Figure 4-4. This figure focuses on the maximum annual temperatures seen at the top of the till layer over a simulation duration of 100 years (2015 to 2115). The Rayleigh value over time for each of these permeabilities is also plotted, measured at the centre of the T1 (coarse) layer (Figure 4-5). The critical Rayleigh value of 27.1 is marked on this plot as well. A logarithmic plot is chosen to display the large range of Rayleigh values that accompany the data.

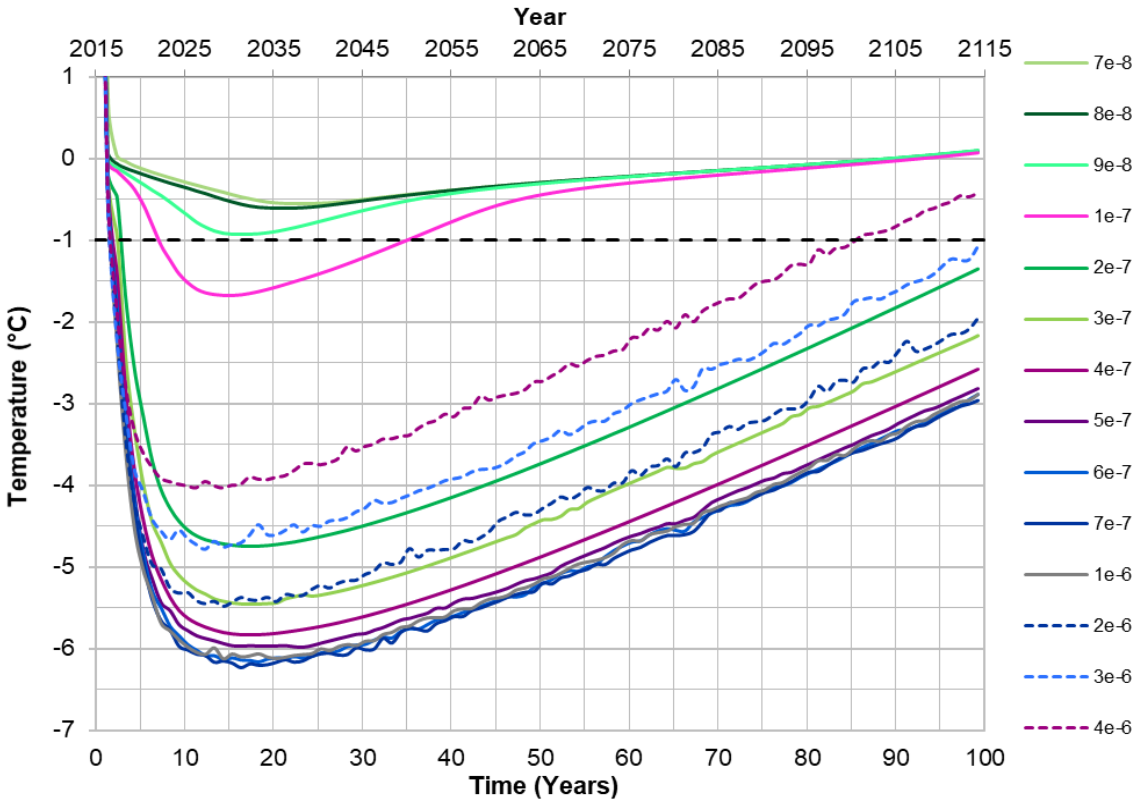

Figure 4-4: T1 (coarse) permeability (m^2) variations – Top of Till Temperatures (Maximum annual temperatures)

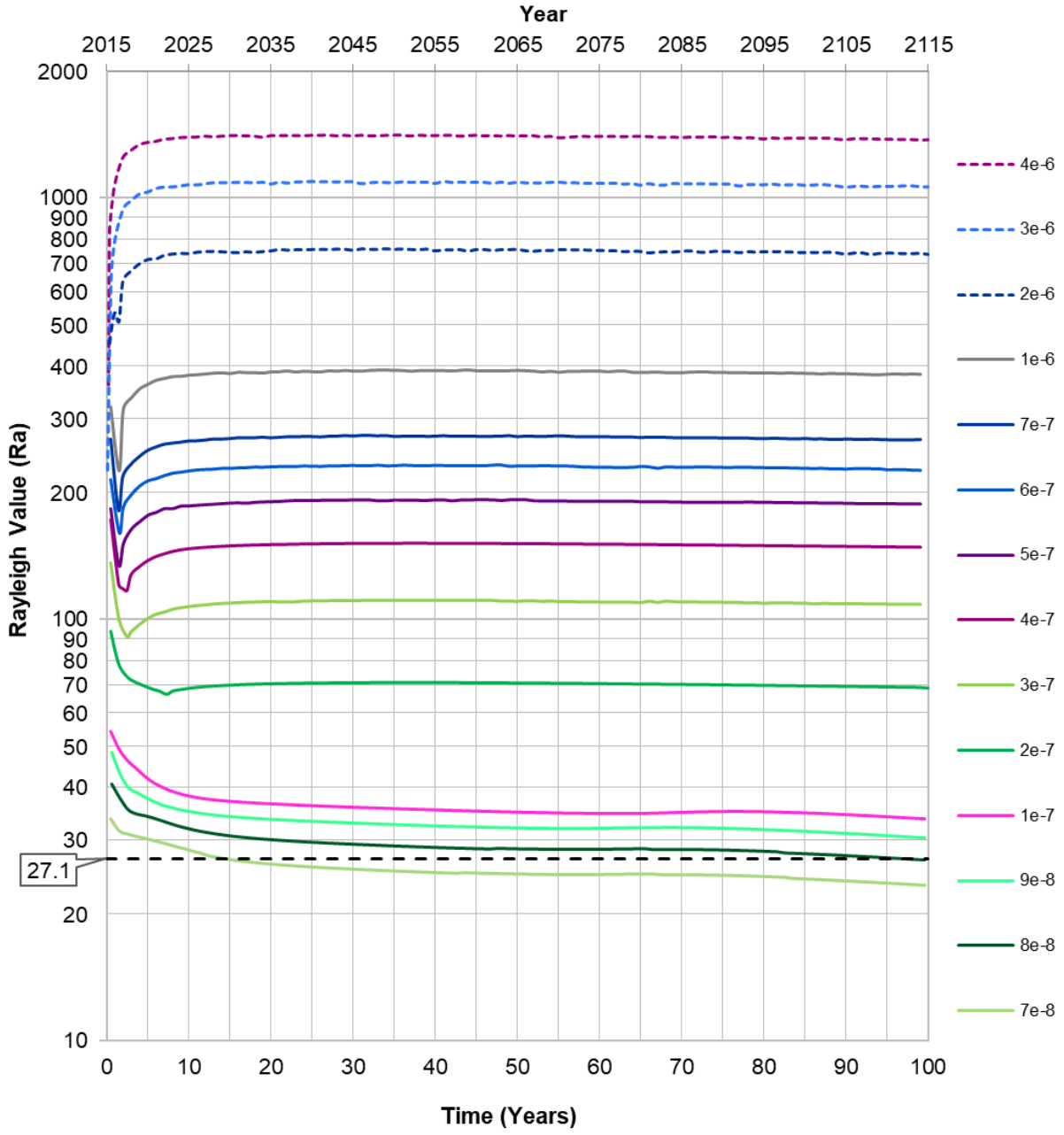

Figure 4-5: T1 (coarse) permeability (m^2) variations – Maximum Rayleigh Value (Maximum annual Rayleigh values of the convective T1 (coarse) layer)

4.1.2.3 Discussion

Figure 4-4 demonstrates the temperatures at the top of the till layer over 100 years with a black dashed line presenting the temperature of -1°C. As seen in this figure, the increase in T1 (coarse) permeability from K = 1 x 10^{-7} m^2 to K = 2 x 10^{-7} m^2 makes a significant drop in annual temperatures in the first 10 years. According to Figure 4-5, the critical Rayleigh value of 27.10 is

achieved for values of $K \geq 8 \times 10^{-8}$ m^2 as the T1 (coarse) permeability of $K = 7 \times 10^{-8}$ m^2 drops below 27.10 early on in the simulation timeline (around year 10). This means that even though permeabilities from $K = 8 \times 10^{-8}$ m^2 to $K = 1 \times 10^{-7}$ m^2 do undergo convective cooling during the winter months the temperature difference is not yet adequate to offset the conductive warming occurring during the summer months. Once the permeability of T1 (coarse) is increased to $K = 2 \times 10^{-7}$ m^2 or higher this barrier is breached, and the convective cooling can then rapidly cool down the pile. This permeability is also able to maintain temperatures at the top of the till below -1°C which means it will serve as the minimum permeability recommended for the engineered T1 (coarse) material.

As the T1 (coarse) material increases in permeability (Figure 4-4) the initial temperature drop increases as convective-cooling effects increase the permafrost aggradation into the materials. This trend is seen within the range of permeabilities from $K = 7 \times 10^{-8}$ m^2 to $K = 1 \times 10^{-6}$ m^2 whereas afterwards the initial temperature drop decreases as permeability increases. The explanation for this change in temperature and permeability relationship is hinted in Figure 4-5 which shows the Rayleigh values representing each permeability over time. As described previously (Section 2.5.4.1 and Section 4.1.2.1), there is an upper limit of the Rayleigh value where convective heat transfer no longer forms stable convection cells and therefore the benefits of a higher permeability is lost. Pham (2013) had compiled results finding this upper value to be between Ra = 280 and Ra = 400, though this was for the condition where $Ra_c = 4\pi^2$ (both boundaries impermeable, conductive). The T1 (coarse) permeability at $K = 1 \times 10^{-6}$ m^2 appears to be able to maintain adequately stable convection cells such as the temperatures are in line with the optimum lower permeabilities (Figure 4-4). Once the T1 (coarse) permeability is increased to $K = 2 \times 10^{-6}$ m^2 and above (denoted by a dashed line in both figures) the convection cells are likely no longer stable given the temperatures presented in Figure 4-4. For this simulation, the unstable regime begins sometime around Ra = 400. This value is on the upper range provided by Pham (2013) however this does represent different boundary conditions than those analyzed during this sensitivity analysis. An upper limit of Ra = 400 is within the same magnitude and as such it does coincide with the expecations of this model. Given these results, the recommended maximum permeability for the T1 (coarse) material would set at $K = 1 \times 10^{-6}$ m^2.

4.1.3 Climate Change

The initial annual temperature increase was set to the base case of +0.056°C/year as per previous research conducted by Pham (2013) and EMAP (2008). As the situation of climate change and global warming continues to worsen and change the model must be tested against the possibility

of an increased temperature range. The temperature increase is adjusted until the top of the till reaches T ≥0°C after 100 years.

4.1.3.1 Results

The annual maximum temperatures measured at the top of the till with increased annual climate change temperatures are presented in Figure 4-6. The temperature increases are based on increasing the base temperature by a given percentage. This percentage is evaluated between 2% and 110% which correspond to +0.057°C/year and +0.118°C/year, respectively.

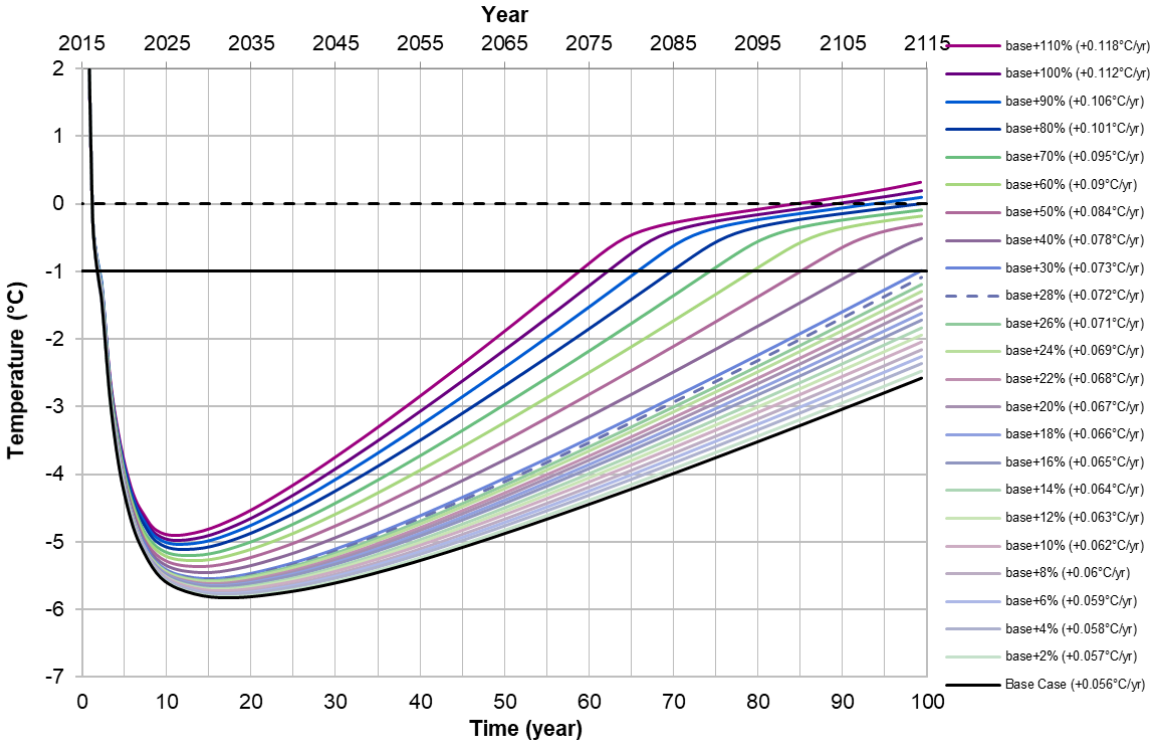

Figure 4-6: Climate change sensitivity analysis over 100 years

4.1.3.2 Discussion

In order to maintain the till material in frozen conditions after 100 years it can be seen that this simulation can handle a maximum temperature increase of +28% (+0.072°C/year) as denoted by the dashed line in Figure 4-6. Given the large range of uncertainty that is factored into climate change predictions (discussed in Section 3.3.4) this value can serve as a known limit as future climate change models become available.

4.2 Thickness Optimization of Soil Cover

The final design optimization is to determine the minimum thicknesses of each cover material that would be required to maintain the T3 material in frozen conditions. The intent of this analysis is to

provide multiple options for a successful soil cover system should certain materials be unavailable.

As discussed previously in this document, the cover design put forward by DDMI (2018) was 3.0 m of T1 material on top of 1.5 m of till. Pham (2013) adjusted this design to recommend an engineered material based on the coarse (>3 cm) fractions of the T1 material. The resulting 3.0 m overlying 1.5 m of T1 (coarse) material and till, respectively, then became the design basis for this research.

This section will consider differing combinations of materials for the cover system along with their optimized values based on multiple design criteria. Material thicknesses were varied in steps of 0.25 m in order to represent the likely maximum precision of heavy mining equipment that would be used to handle the material.

The T1 (coarse) and till cover system will vary combinations from 0.00 to 4.00 m of T1 (coarse) and 0.25 to 1.50 m of till material. The T1 material (denoted T1 (all) for “all fractions”) will be varied between 0.25 m and above for till combinations of till = 0.00 m and till = 1.50 m, only. The T1 (all) material optimization includes a variable upper limit in order to determine the maximum upper limit of a temperature.

4.2.1 Results – T1 (coarse)

The simulations demonstrating varying combinations of T1 (coarse) and till material layer thicknesses are presented here.

A summary of the resulting maximum temperatures seen in the final year of the simulation (July 2114 to June 2115) are presented for all combinations of T1 (coarse) and till at the top of the till layer (Table 4-5) and top of the T3 material (Table 4-6). Each table includes a legend which is presented in the first row. The legend includes colour coding according to where the temperature falls in relation to -1°C and 0°C. For simulations that were not modelled but their relative temperature ranges can be assumed a * is inserted. Results that are not applicable (N/A) may indicate a top of till temperature where no till is included in the simulation.

The temperature limit for the sensitivity analysis (Section 4.1) uses a contingency temperature of peak final temperatures of -1°C for the top of the till material. While this is a fair limit to consider for this design optimization, should this be the only requirement then the soil cover prescriptions without a till latent heat layer can not be directly compared. As a result, the range of design criteria in terms of maximum temperatures at a given location are presented in Section 4.2.3.

The corresponding figures for till thicknesses 0.00 m to 1.50 m are presented from Figure 4-7 to Figure 4-13, respectively. The figures present the maximum annual temperatures (summer) seen over a duration of 100 years (July 2015 to June 2115) at both top of the till and top of the T3 layers. Each of these figures has a set till thickness with a variable T1 (coarse) thickness. The results which are presented at the top of the till are presented with a solid line whereas the top of the T3 material is presented with a small dashed line. The temperature lines for 0°C (black, large dashed line) and -1°C (black, solid line) are also included for reference.

Table 4-5: T1 (coarse) and till layer Thickness Summary (top of till temperature)

Legend	$T_{(max)}$, t = 99 – 100 years	≤-1°C	*	-1°C to 0°C	*	≥0°C	*	N/A
Top of Till	**Till (m)**							
T1 (coarse) (m)	0.00	0.25	0.50	0.75	1.00	1.25	1.50	
0.00	N/A	*	*	*	*	*	*	
0.25	N/A	+14.91	+14.74	+14.54	+14.32	+13.97	+13.56	
0.50	N/A	+10.77	+10.42	+10.01	+9.47	+8.81	+8.38	
0.75	N/A	+8.04	+7.25	+6.66	+5.76	+4.72	+4.52	
1.00	N/A	+5.47	+4.49	+3.97	+2.76	+2.64	+2.73	
1.25	N/A	+3.66	+2.62	+1.77	+1.52	+1.44	+1.47	
1.50	N/A	+2.18	+1.28	+0.88	+0.79	+0.76	+0.73	
1.75	N/A	+0.97	+0.44	+0.39	+0.37	+0.31	+0.29	
2.00	N/A	+0.23	+0.10	+0.07	+0.02	+0.01	-0.01	
2.25	N/A	-0.07	-0.13	-0.15	-0.07	-0.20	-0.24	
2.50	N/A	-0.32	-0.36	-0.46	-0.59	-0.59	-0.86	
2.75	N/A	-0.98	-1.14	-1.12	-1.59	-1.613	-1.61	
3.00	N/A	-1.93	-2.10	-2.15	-2.40	-2.54	**-2.58**	

Table 4-6: T1 (coarse) and till layer Thickness Summary (top of T3 temperature)

Legend	$T_{(max)}$, t = 99 – 100 years	≤-1°C	*	-1°C to 0°C	*	≥0°C	*	N/A
Top of T3	**Till (m)**							
T1 (coarse) (m)	0.00	0.25	0.50	0.75	1.00	1.25	1.50	
0.00	+19.92	*	*	*	*	*	*	
0.25	+15.06	+13.91	+12.78	+11.65	+10.58	+9.33	+8.05	
0.50	+11.40	+9.93	+8.80	+7.66	+6.42	+5.15	+4.19	
0.75	+8.58	+7.36	+5.88	+4.73	+3.30	+1.85	+0.83	
1.00	+6.08	+4.87	+3.33	+2.36	+0.89	-0.06	-0.15	
1.25	+4.17	+3.13	+1.67	+0.56	-0.17	-0.32	-0.43	
1.50	+2.84	+1.72	+0.51	-0.13	-0.37	-0.49	-0.60	
1.75	+1.73	+0.60	-0.14	-0.35	-0.49	-0.63	-0.75	
2.00	+0.97	-0.03	-0.32	-0.51	-0.68	-0.81	-0.94	
2.25	+0.31	-0.28	-0.51	-0.69	-0.28	-1.05	-1.27	
2.50	-0.08	-0.53	-0.77	-1.08	-1.42	-1.42	-2.06	
2.75	-0.85	-1.20	-1.57	-1.74	-2.38	-2.55	-2.70	
3.00	-1.67	-2.14	-2.49	-2.71	-3.12	-3.41	**-3.58**	
4.00	-5.10	*	*	*	*	*	*	

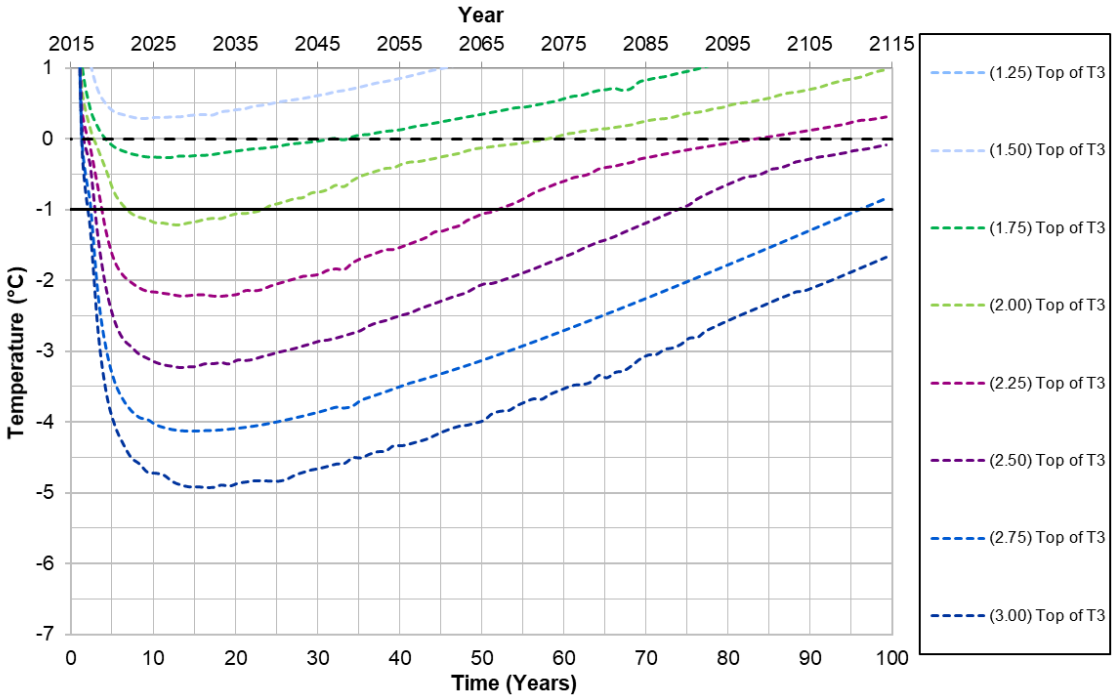

Figure 4-7: Cover thickness optimization (T1 (coarse) varied + 0.00 m Till)
(Maximum annual temperatures over 100 years)

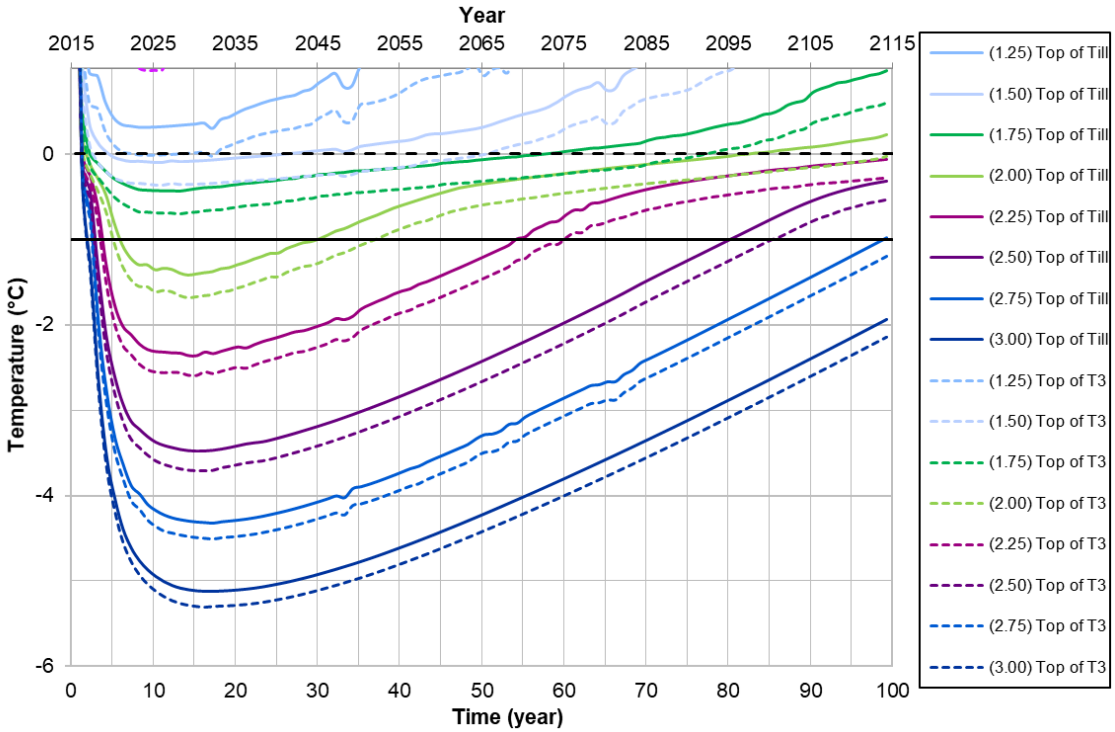

Figure 4-8: Cover thickness optimization (T1 (coarse) varied + 0.25 m Till)
(Maximum annual temperatures over 100 years)

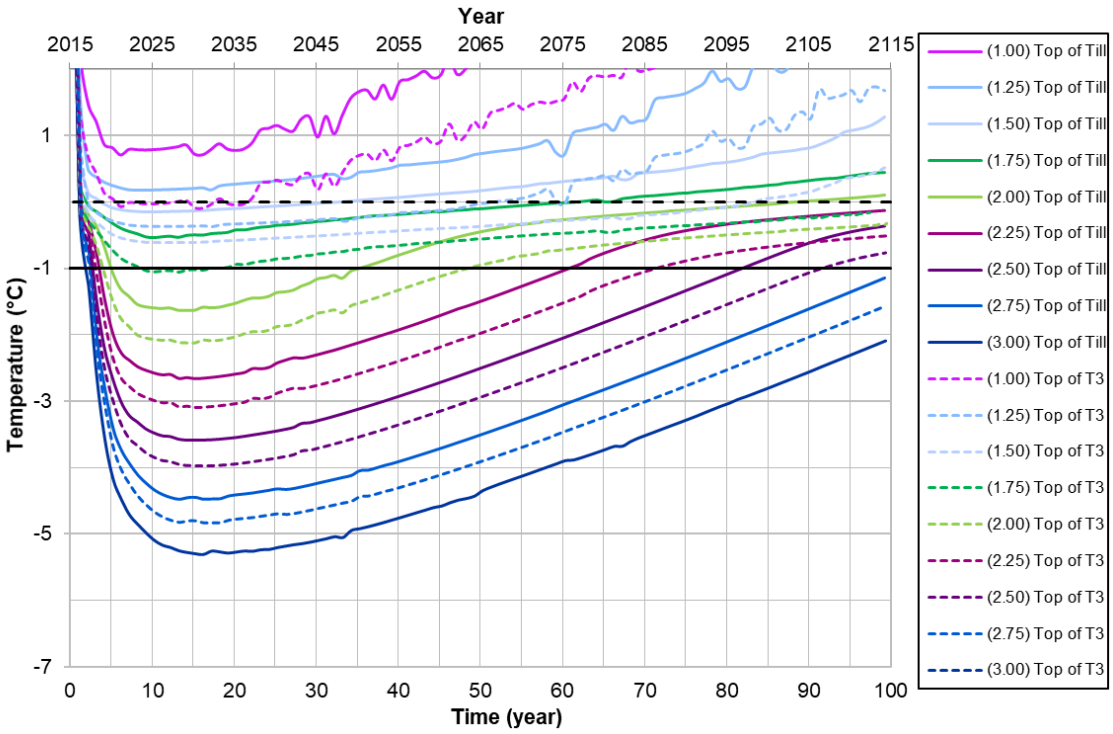

Figure 4-9: Cover thickness optimization (T1 (coarse) varied + 0.50 m Till)
(Maximum annual temperatures over 100 years)

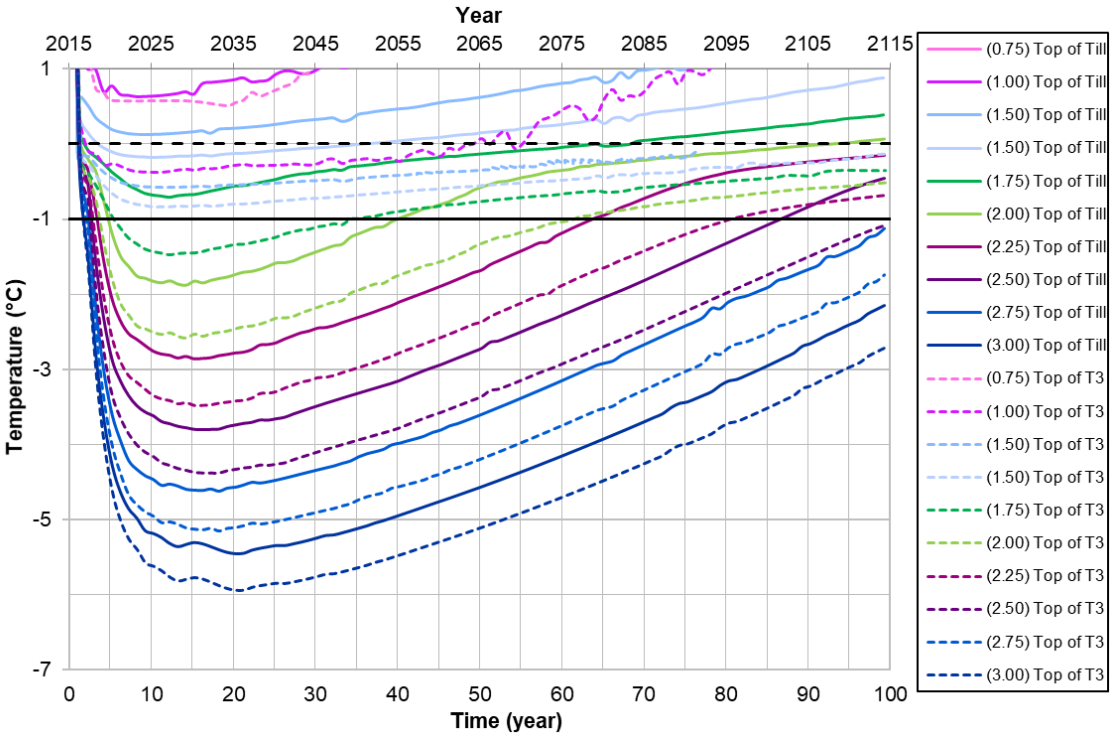

Figure 4-10: Cover thickness optimization (T1 (coarse) varied + 0.75 m Till)
(Maximum annual temperatures over 100 years)

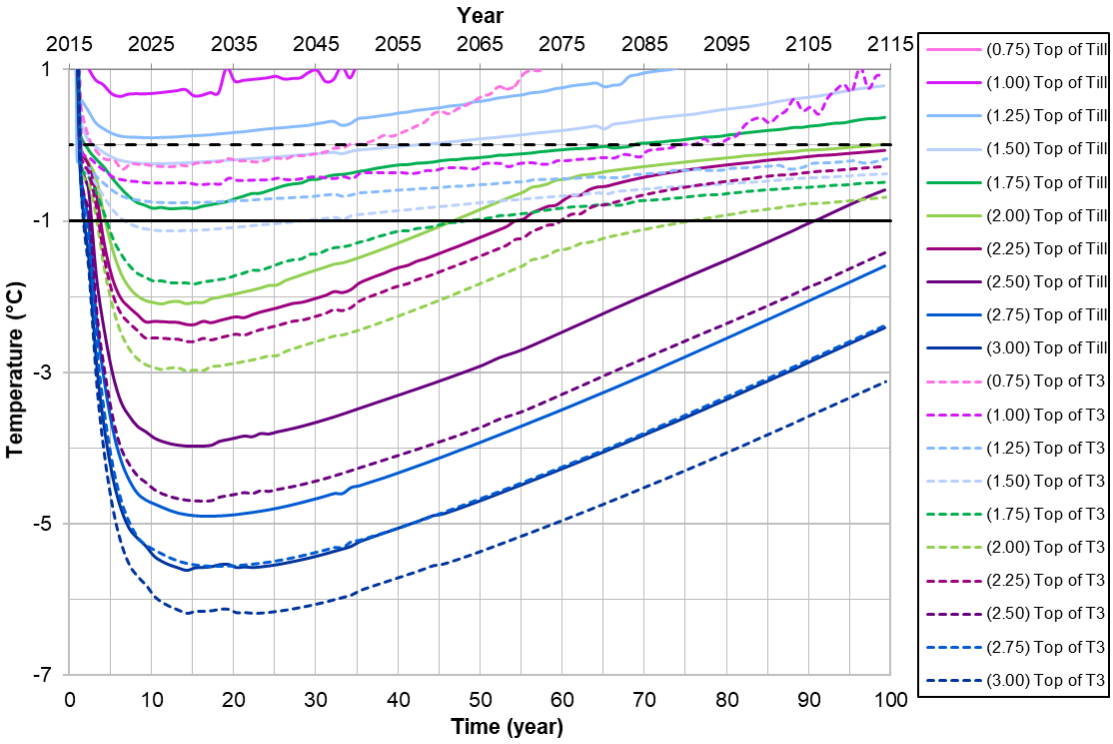

Figure 4-11: Cover thickness optimization (T1 (coarse) varied + 1.00 m Till) (Maximum annual temperatures over 100 years)

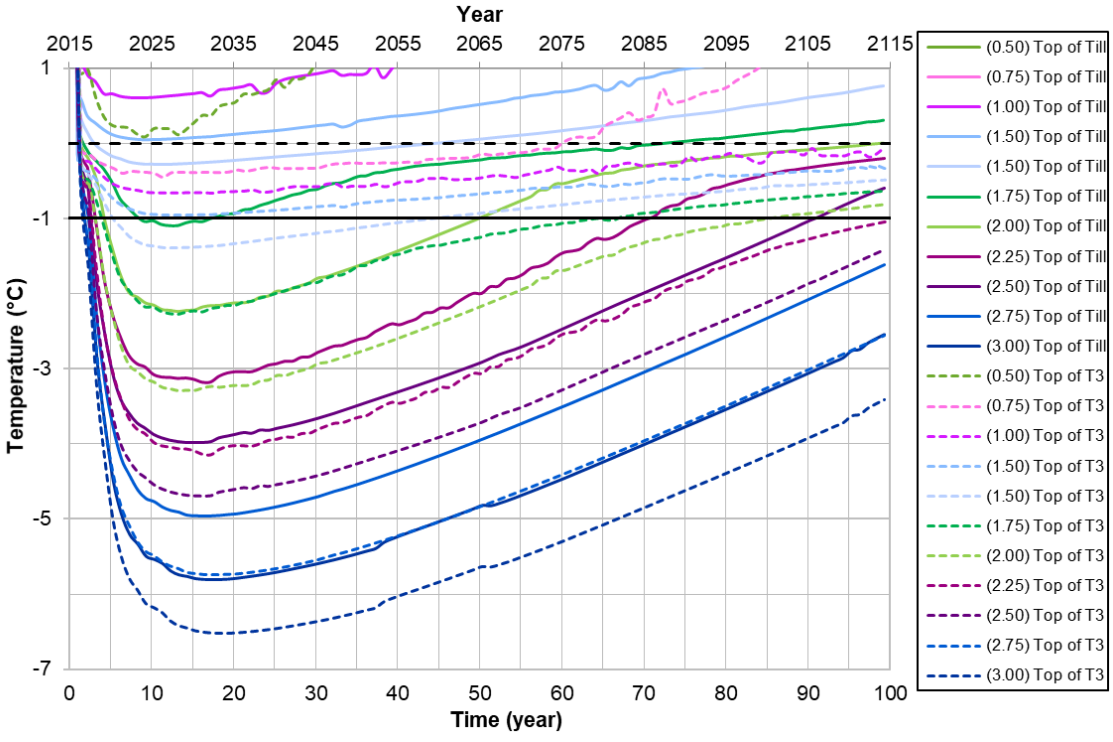

Figure 4-12: Cover thickness optimization (T1 (coarse) varied + 1.25 m Till) (Maximum annual temperatures over 100 years)

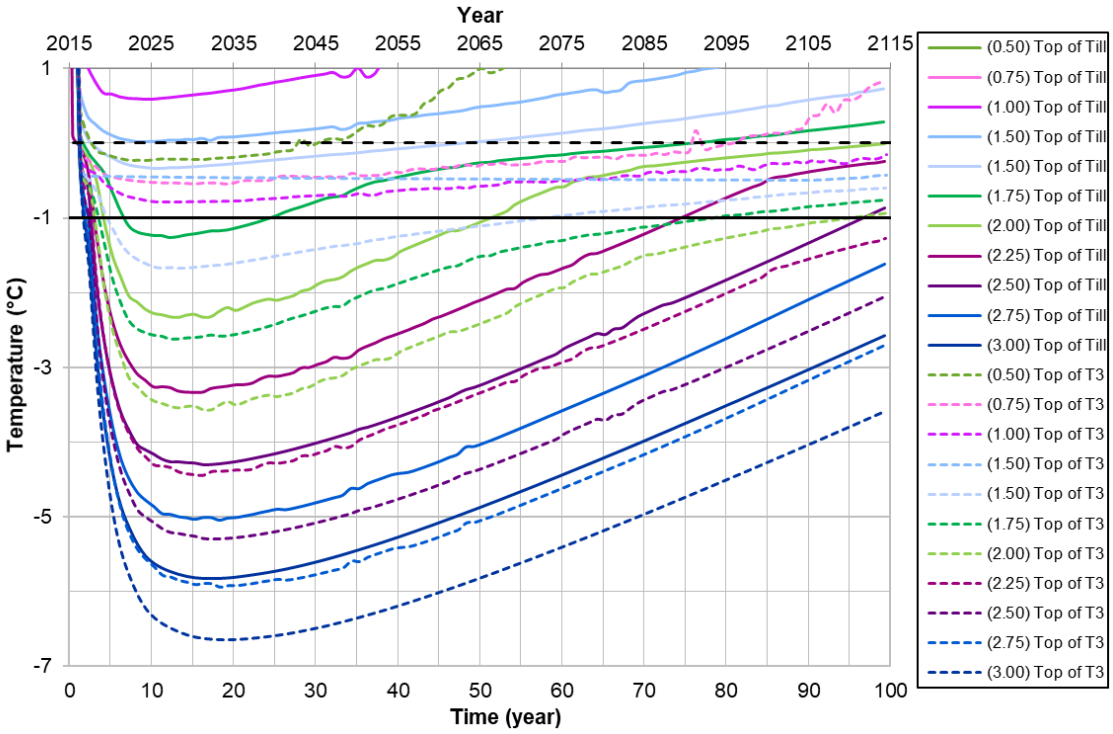

Figure 4-13: Cover thickness optimization (T1 (coarse) varied + 1.50 m Till) (Maximum annual temperatures over 100 years)

4.2.2 Results – T1 (all)

The simulations demonstrating combinations of T1 (all) and till material layer thicknesses are presented here.

A summary of the resulting maximum temperatures seen in the final year of the simulation (July 2114 to June 2115) are presented for all combinations of T1 (all) and till at the top of the till layer and top of the T3 material in Table 4-7. The table includes a legend which is presented in the first row. The legend includes colour coding according to where the temperature falls in relation to -1°C and 0°C. For simulations that were not modelled but their relative temperature ranges can be assumed, a * is inserted. Results that are not applicable (N/A) may indicate a top of till temperature where no till is included in the simulation.

The temperature limit for the sensitivity analysis (Section 4.1) uses a contingency temperature of peak final temperatures of -1°C for the top of the till material. While this is a fair limit to consider for this design optimization, should this be the only requirement then the soil cover prescriptions without a till latent heat layer can not be directly compared. As a result, the range of design criteria in terms of maximum temperatures at a given location are presented in Section 4.2.3.

The corresponding figures for till thicknesses 0.00 m and 1.50 m are presented in Figure 4-14 and Figure 4-15, respectively. The figures present the maximum (summer) annual temperatures seen over a duration of 100 years (July 2015 to June 2115) at both top of the till and top of the T3 layers. Each of these figures has a set till thickness with a variable T1 (all) thickness. The results which are presented at the top of the till are presented with a solid line whereas the top of the T3 material is presented with a small dashed line. The temperature lines for 0°C (black, large dashed line) and -1°C (black, solid line) are also included for reference.

Table 4-7: T1 (all) and till layer Thickness Summary table (top of till, top of T3 temperatures)

Legend	$T_{(max)}$, t = 99 – 100 years	≤-1°C	*	-1°C to 0°C	*	≥0°C	*	N/A
	Till (m)							
Measured at	**Top of Till**			**Top of T3**				
T1 (all) (m)	0.00	1.50		0.00		1.50		
0.25	N/A	+17.70		*		*		
0.50	N/A	+15.60		*		*		
0.75	N/A	+13.68		*		*		
1.00	N/A	+11.84		*		*		
1.25	N/A	+10.15		*		*		
1.50	N/A	+8.91		+5.24		1.65		
1.75	N/A	+7.58		+4.23		+0.76		
2.00	N/A	+6.36		+3.20		-0.04		
2.25	N/A	+5.38		+2.53		-0.14		
2.50	N/A	+4.15		*		*		
2.75	N/A	+3.45		+1.11		-0.33		
3.00	N/A	+2.84		+0.72		-0.37		
3.25	N/A	+1.93		+0.54		-0.35		
3.50	N/A	+1.26		+0.20		-0.41		
3.75	N/A	+0.70		-0.02		-0.46		
4.00	N/A	+0.25		-0.13		-0.46		
4.25	N/A	+0.01		*		*		
4.50	N/A	-0.18		-0.33		-0.54		
4.75	N/A	-0.30		*		*		
5.00	N/A	-0.36		-0.40		-0.56		
6.00	N/A	-0.49		-0.55		-0.64		
7.00	N/A	-0.60		*		*		
8.00	N/A	-0.68		-0.73		-0.78		
11.00	N/A	-0.78		-0.78		-0.80		

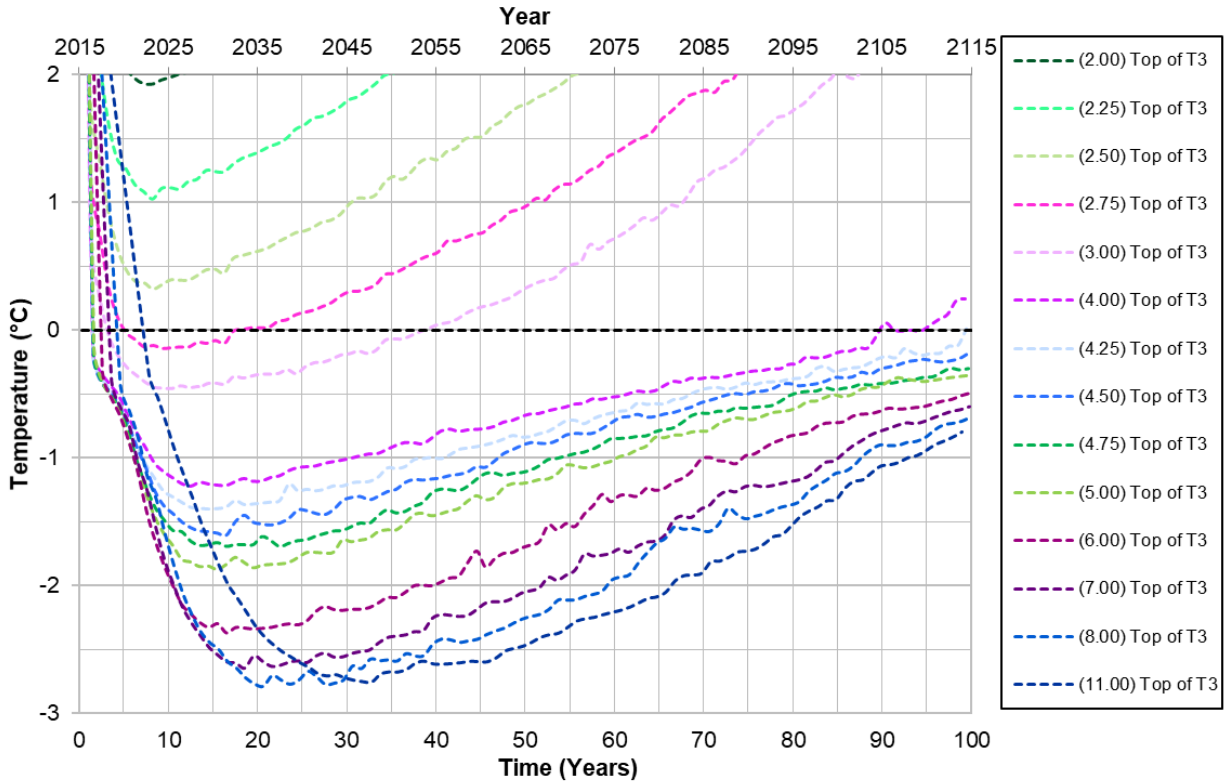

Figure 4-14: Cover thickness optimization (T1 (all) varied + 0.00 m Till)
(Maximum annual temperatures over 100 years)

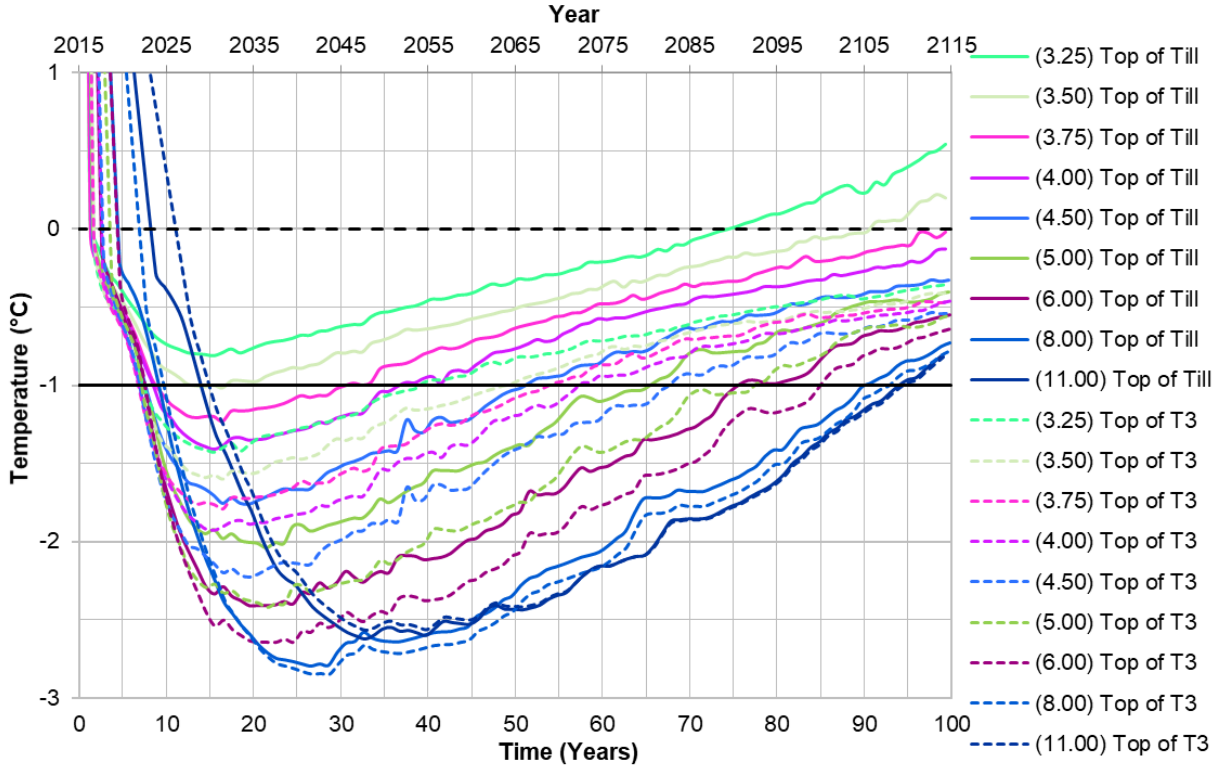

Figure 4-15: Cover thickness optimization (T1 (all) varied + 1.50 m Till)
(Maximum annual temperatures over 100 years)

4.2.3 Discussion

As presented in Figure 4-13 (and corresponding Table 4-5 and Table 4-6), the 3.00 m of T1 (coarse) material and 1.50 m of till material is able to maintain the T3 material frozen after 100 years. As presented in the T1 (coarse) figures and tables there are some optimization options that may find success with thinner cover thicknesses.

Depending on the level of contingency a client wants to incorporate there are a few different prescription recommendations that may be considered. Since the main goal of this cover is to maintain the T3 material in frozen conditions after 100 years a design criterion of T_{max} ≤0°C at the top of the T3 material would suffice. It was noted in the sensitivity analyses of this research (Section 4.1) that given the phase change processes and latent heat factors that occur between -1°C and +1°C and the importance of the latent heat layer it may be wise to focus on the top of the till material in lieu of the top of the T3 material. A second and third design criterion then can be set for the top of the till as T_{max} ≤0°C and T_{max} ≤-1°C, respectively. Finally, should a further contingency be required, a fourth design criterion can set the T_{max} ≤-1°C at the top of the T3 material. These 4 design criteria are thereby set in order of increasing contingency levels. A summary of the minimum material thicknesses required to satisfy the 4 design criteria is listed in Table 4-8. These specific cases correspond to bolded line weights in the results tables for T1 (coarse) top of till, T1 (coarse) top of T3, and both T1 (all) top of till and top of T3 (Table 4-5, Table 4-6, and Table 4-7, respectively. Table 4-8 follows the same legend descriptors as these three superseding tables, with an additional “CNM” indicating Condition Not Met. Some of the T1 (coarse) cover designs present multiple options depending on if the user would prefer to minimize the T1 (coarse) or till material.

These results also demonstrate that designs that use the T1 (all) material are unable to remain below -1°C for both top of till and top of T3 locations. Without removing the fine fractions of the material, the T1 (all) does not achieve convective heat transfer and as a result conduction occurs both in summer and winter months. Without the initial frost aggradation that is seen within convective cases of T1 (coarse) material the resulting temperatures after 100 years are also higher. These stay between -1°C and 0°C despite increasing material thicknesses of T1 (all). Even when the T1 (all) material is increased to 11.00 m, the temperatures at the top of the T3 material remain in this range. In fact, at this material thickness the two till conditions (1.50 m and 0.00 m of till) result in nearly the same temperatures (-0.78°C and -0.80°C, respectively) as the 11.0 m is

thick enough such that both top of the T3 locations sees minimal temperature fluctuations from the surface.

Table 4-8: Thickness optimization table summary given four target criteria conditions

	Column 1		Column 2					Column 3				
	T1 Material Type		**T1 (coarse)**					**T1 (all)**				
	Criteria		**No Till**		**With Till**			**No Till**		**With Till**		
#	Top of Target Layer	Temp ≤	Temp (°C)	T1 (m)	Temp (°C)	T1 (m)	Till (m)	Temp (°C)	T1 (m)	Temp (°C)	T1 (m)	Till (m)
1	**T3**	**0°C**	-0.08	2.50	-0.06 -0.03	1.00 2.00	1.25 0.25	-0.02	3.75	-0.04	2.00	1.50
2	**Till**	**0°C**	N/A		-0.01 -0.13	2.00 2.25	1.50 0.50	N/A		-0.18	4.50	1.50
3	**Till**	**-1°C**	N/A		-1.14	2.75	0.50	N/A		CNM		
4	**T3**	**-1°C**	-1.67	3.00	-1.05 -1.20	2.25 2.75	1.25 0.25	CNM		CNM		

To determine a recommended soil cover thickness a user may follow the following steps in accordance with Table 4-8:

1. Decide whether the top (or only) layer of material in the cover will be T1 (coarse) (Column 2) or T1 (all) (Column 3).
2. Determine the temperature and location for the design criterion (Column 1). The focus can either be on the temperature of the top of the T3 material (criterion 1 or 4) or of the top of the till material (criterion 2 or 3). The focus temperature can then be either T ≤0°C (criterion 1 or 2) or T ≤-1°C (criterion 3 or 4).
3. The intersection between the selected criterion and columns will then present the optimized material prescription. There are two options for both criterion 2 and criterion 4 as they present a minimized T1 (coarse) thickness followed by a minimized till thickness. The user may select a combination based on material availability.

The success of incorporating the till latent heat layer or changing the T1 (all) material to T1 (coarse) can be demonstrated by comparing one of the above criteria. Using criterion 1, where the top of the T3 material is ≤0°C after 100 years, using only T1 (all) material requires a material

thickness of 3.75 m. When adding a 1.50 m layer of till to act as a latent heat layer, the T1 (all) material reduces to a required thickness of 2.00 m. If using only T1 (coarse) material, the required thickness changed from 3.75 m to 2.50 m. Further optimizing this condition and using both T1 (coarse) and a 1.50 m latent heat layer of till material brings the thickness to 1.00 m. These four comparative cases demonstrate the resulting benefits of incorporating engineered materials or a latent heat layer into the design.

5 Conclusions and Recommendations

The four key objectives for this research were:

1. Demonstrate a successful model benchmark analysis between this research and Pham (2013)'s model
2. Conduct a sensitivity analysis to determine the model robustness and uncertainty in assumed parameters
3. Optimize the soil cover thicknesses that will be sufficient to maintain frozen conditions after 100 years
4. Provide future suggestions for construction of test cells and potential soil cover prescriptions to be constructed on top of the full-scale waste rock pile

The follow-through on reclamation objectives is critical for current operator, stakeholder, and community relationships and will set the tone for future projects of this nature. Achieving a reclamation objective requires adequate forethought and tested designs which this research supports.

The optimization of an ACC soil cover in this research further refines recommendations and increases the confidence in the ARD-mitigating closure design at Site. These research results offer the flexibility of material requirements should there be limited availability while also accounting for future scenarios of global climate change temperature increases.

A reduced material volume requirement will also realize savings associated with material transport and placing costs which can be astronomical for volumes of this magnitude. Cost-savings may also increase the viability of sites which had previously been unable to employ the use of an air convective cover at larger required volumes.

The research is in line with the social, environmental, and economical stewardship that is vital for the success of current and future projects in Canada's Northern landscapes. Detailed research conclusions are presented below.

5.1 Model Benchmarking

Model benchmarking demonstrated that the updated simulation intended to carry forward the work conducted by Pham (2013) was able to successfully initiate natural convective cooling in the winter seasons and only conductive cooling in the summer seasons. This was confirmed upon visual inspection of the temperature gradient profile. Further results compared maximum and

minimum temperatures observed at both the top of till and top of T3 layers over 100 years. These plots included both original results by Pham (2013) and results from the recreated modelling environment for this research. While the results were not completely aligned, the disparities were acceptable and the model benchmarking and set up of this modelling environment was considered a success.

5.2 Sensitivity Analysis Limits and Recommendations

A sensitivity analysis was conducted for the moisture content of the till material, the permeability of the T1 (coarse) material, and the annual climate change value increase added to the surface temperatures of the structure. These sensitivities considered a soil cover of 3.0 m T1 (coarse) material on top of 1.50 m of till material as recommended by previous research (Pham 2013). The recommended range of conditions determined during each sensitivity analysis is dependent on the given design and may not be applicable for other soil cover combinations. Their relevant trends however may serve as a basis for alternative design considerations.

This author recommends a minimum volumetric moisture content of the till material to be 0.08 (equivalent degree of saturation of 40%) to take advantage of the latent heat effects of water within the till material.

When considering the engineered T1 (coarse) material it is recommended that the permeability be within the range of 1.0×10^{-6} m^2 and 2.0×10^{-7} m^2 to maintain the till (and therefore T3 potentially acid-generating (PAG) material) frozen after 100 years.

The climatic warming sensitivity demonstrated that the modelled annual temperature increase of +0.056°C/year can withstand an increase by 28% to a maximum of +0.072°C/year while still maintaining the till and T3 materials in frozen conditions.

5.3 Soil Cover Thickness Optimization

The materials which were considered for the soil cover included T1, T1 (coarse), and till on top of the T3 PAG material. Based on different targeted design criteria, multiple combinations of material prescriptions are provided (Table 5-1). The targeted design criteria are arranged in order of increasing contingency and focus on temperatures after 100 years at the top of specified locations (till or T3 material, ≤0°C or ≤-1°C). The provided table allows a user to balance material availability, contingency level comfort, and confidence in the simulation results.

Table 5-1: Cover design optimization summary

	T1 Material Type		T1 (coarse)					T1 (all)				
	Criteria		No Till		With Till			No Till		With Till		
#	Top of Target Layer	Temp ≤	Temp (°C)	T1 (m)	Temp (°C)	T1 (m)	Till (m)	Temp (°C)	T1 (m)	Temp (°C)	T1 (m)	Till (m)
1	T3	0°C	-0.08	2.50	-0.06	1.00	1.25	-0.02	3.75	-0.04	2.00	1.50
					-0.03	2.00	0.25					
2	Till	0°C	N/A		-0.01	2.00	1.50	N/A		-0.18	4.50	1.50
					-0.13	2.25	0.50					
3	Till	-1°C	N/A		-1.14	2.75	0.50	N/A		CNM		
4	T3	-1°C	-1.67	3.00	-1.05	2.25	1.25	CNM		CNM		
					-1.20	2.75	0.25					

5.4 Proposed field testing

5.4.1 Sampling

Further proposed field testing would aim to verify material properties of the T1, T3, and till materials. Key parameters that could be determined through grab samples would be density, in-situ volumetric moisture content, particle size distribution, and porosity. These parameters would be helpful in confirming assumptions that were made for this simulation particularly for the till material which had fewer site-specific values. This may also provide information on the field condition of material if it has been stockpiled or relocated which can further adjust material values.

5.4.2 Field Separation and the Removal of Fine Particles

Should an engineered material such as T1 (coarse) be considered then the process of completing the sieving should be tested in field to appropriately account for both minimum and maximum particle sizes, equipment sizes, and the available technology.

5.4.3 Field Testing Plots

The recommended material combinations presented in Table 5-1 should be investigated and tested in the field. These should be adequately large to ensure that the edge effects are small. Pham (2013) recommended 10 times the thickness of the T1 layer to reduce the chance of edge effects. Each area should have a trio of vertical thermistors installed in the center of the plot,

penetrating roughly 5.0 m into the T3 material. Three thermistors should allow for data calibration for each test and thermistor beads need be planned to capture the temperatures at any material interfaces (T1-Till, T1-T3, or Till-T3). The recommended soil cover combinations for these plots are listed below, organized based on material availability design considerations.

Base condition

- No cover

Design Target: No till material

- 2.50 m T1 (coarse) material, no till
    - Minimum plot 25 m x 25 m
- 3.00 m T1 (coarse) material, no till
    - Minimum plot 30 m x 30 m
- 3.75 m T1 (all) material, no till
    - Minimum plot 37.5 m x 37.5 m

Design Target: Limit Till Material

- 1.00 m T1 (coarse) material, 1.25 m till
    - Minimum plot 22.5 m x 22.5 m
- 2.00 m T1 (coarse) material, 0.25 m till
    - Minimum plot 22.5 m x 22.5 m
- 4.50 m T1 (all) material, 1.50 m till
    - Minimum plot 60 m x 60 m

Design Target: Limit T1 (coarse) material

- 2.00 m T1 (coarse) material, 0.25 m till
    - Minimum plot 22.5 m x 22.5 m
- 2.25 m T1 (coarse) material, 0.50 m till
    - Minimum plot 27.5 m x 27.5 m
- 2.25 m T1 (coarse) material, 1.25 m till
    - Minimum plot 35 m x 35 m
- 2.75 m T1 (coarse) material, 0.25 m till
    - Minimum plot 30 m x 30 m

- 2.00 m T1 (all) material, 1.50 m till
    - Minimum plot 35 m x 35 m

5.4.4 Future research

Updated climatic models and the resulting surface temperature equation would allow for a more accurate temperature prediction. Climate change research is ongoing, and models and assumptions are always being updated. In addition, the application of multi-phase flow within a porous media in the latest version of Comsol may allow for further refinement and understanding of impacts of unsaturated soil mechanics within this structure. As more modules are released by Comsol the modelling capabilities can be increased.

Material heterogeneity can be further accounted for within the model by dividing the defined subdomains further and adjusting permeabilities. As described by the permeability limitation in Section 3.3.7, the particle sizing within the T3 structure may increase in size with depth. Discussions with the mining operations group on a given site can provide a more detailed description of the structure construction and associated bench heights which can further aide in subdomain definition.

References

Adu-Wusu, C., and Yanful, E.K. 2006. Performance of engineered test covers on acid-generating waste rock at Whistle Mine, Ontario. Canadian Geotechnical Journal, **43**(1): 1–18. doi:10.1139/t05-088.

Adu-Wusu, C., and Yanful, E.K. 2007. Post-closure investigation of engineered test covers on acid-generating waste rock at Whistle Mine, Ontario. Canadian Geotechnical Journal, **44**(4): 496–506. doi:10.1139/t06-132.

Amos, R.T., Blowes, D.W., Bailey, B.L., Sego, D.C., Smith, L., and Ritchie, A.I.M. 2015. Waste-rock hydrogeology and geochemistry. Applied Geochemistry, **57**(1): 140–156. doi:10.1016/j.apgeochem.2014.06.020.

Amos, R.T., Blowes, D.W., Smith, L., and Sego, D.C. 2009. Measurement of Wind-Induced Pressure Gradients in a Waste Rock Pile. Vadose Zone Journal, **8**(4): 953–962. John Wiley & Sons, Ltd. doi:https://doi.org/10.2136/vzj2009.0002.

Andersland, O.B., and Ladanyi, B. 2004. Frozen ground engineering. John Wiley & Sons, Inc., Hoboken, New Jersey.

Arenson, L., and Sego, D.C. 2006. Considering convective air fluxes in the design of engineered structures in cold regions. *In* Proceedings of the 59th Canadian geotechnical conference and the seventh joint CGS/IAH-CNC groundwater specialty conference. Vancouver, British Columbia. p. 8.

Arenson, L., Sego, D.C., and Newman, G. 2006. The use of a convective heat flow model in road designs for Northern regions. *In* 2006 IEEE EIC Climate Change Conference. IEEE, Ottawa, Ontario. pp. 1–8.

ASTM. 2017. Standard practice for classification of soils for engineering purposes (Unified Soil Classification System). ASTM D2487-17. ASTM International, West Conshohocken, Pennsylvania.

Azam, S., Wilson, G.W., Herasymuik, G., Nichol, C., and Barbour, L.S. 2007. Hydrogeological behaviour of an unsaturated waste rock pile: A case study at the Golden Sunlight Mine, Montana, USA. Bulletin of Engineering Geology and the Environment, **66**(3): 259–268. doi:10.1007/s10064-006-0077-7.

Bailey, B.L. 2013. Geochemical and microbiological characterization of effluent and pore water from low-sulfide content waste rock. Ph.D thesis, Department of Earth and Environmental Sciences, University of Waterloo, Waterloo, Ontario.

Bailey, B.L., Blowes, D.W., Smith, L., and Sego, D.C. 2016. The Diavik Waste Rock Project: Geochemical and microbiological characterization of low sulfide content large-scale waste rock test piles. Applied Geochemistry, **65**(1): 54–72. doi:10.1016/j.apgeochem.2015.10.010.

Barsi, D. 2017. Spatial variability of particles in waste rock piles. M.Sc. thesis, Department of Civil and Environmental Engineering, University of Alberta, Edmonton, Alberta.

Barsi, D., Beier, N.A., Sego, D.C., Atherton, C., Blowes, D.W., Smith, L., and Amos, R.T. 2019. Classifying variability of material properties in mine waste rock. CIM Journal, **10**(2): 77–93. doi:10.15834/cimj.2019.8.

Bates, R.E., and Bilello, M.A. 1966. Defining the cold regions of the Northern Hemisphere. Technical Report 178, US Army Corps of Engineers, Cold Regions Research and Engineering Laboratory. Hanover, New Hampshire.

Bear, J. 1972. Dynamics of fluids in porous media. Dover Publications, New York, New York.

Benzaazoua, M., Bouzahzah, H., Taha, Y., Kormos, L., Kabombo, D., Lessard, F., Bussière, B., Demers, I., and Kongolo, M. 2017. Integrated environmental management of pyrrhotite tailings at Raglan Mine: Part 1 challenges of desulphurization process and reactivity prediction. Journal of Cleaner Production, **162**(1): 86–95. doi:10.1016/j.jclepro.2017.05.161.

BGC. 2014. A21 Dike 2014 Design Report Update. Vancouver, British Columbia.

Blowes, D.W., Ptacek, C.J., Jambor, J.L., Weisener, C.G., Paktunc, D., Gould, W.D., and Johnson, D.B. 2014. The Geochemistry of Acid Mine Drainage. *In* Treatise on Geochemistry, 2nd edition. *Edited by* H.D. Holland and K.K. Turekian. Elsevier, Oxford, United Kingdom. pp. 131–190.

Boulanger-Martel, V., Bussière, B., and Côté, J. 2021. Thermal Behaviour and performance of two field experimental insulation covers to control sulfide oxidation at Meadowbank mine, Nunavut. Canadian

Geotechnical Journal, **58**(3): 427–440. Canadian Science Publishing. doi:10.1139/cgj-2019-0616.

Brigham, L.W., and Nelson, F.E. 2003. Climate change, permafrost, and impacts on civil infrastructure. U.S. Arctic Research Commission, Arlington, Virginia.

Brown, R.J.E. 1970. Permafrost in Canada: Its influence on northern development. University of Toronto Press, Toronto, Ontario.

Brown, R.J.E., and Péwé, T.L. 1973. Distribution of permafrost in North America and its relationship to the environment: a review, 1963-1973. *In* Permafrost: The North American Contribution to the Second International Conference. National Academy of Sciences, Washington, D.C. pp. 71–100.

Brown, W.G. 1963. Graphical determination of temperature under heated or cooled areas on the ground surface. National Research Council Canada, Ottawa, Ontario.

Bush, E., and Lemmen, D.S. 2019. Canada's Changing Climate Report. Government of Canada, Ottawa, Ontario.

CIRNAC, Government of Nunavut, NTI, and CNGO. 2018. Overview 2018 - Nunavut: Mineral exploration, mining, and geoscience. Crown-Indigenous Relations and Northern Affairs Canada, Gatineau, Quebec.

Collette, L. 2017. Cryohydrogeology of a Covered Waste Rock Pile in Permafrost Environment: Large Scale Field Experiment and Freeze-Thaw Numerical Investigations. M.Sc. thesis, Department of Geological Engineering, University of British Columbia, Vancouver, British Columbia.

Comsol. 2018a. Heat Transfer Module. Comsol, Inc., Los Altos, California.

Comsol. 2018b. Introduction to Comsol Multiphysics. Version 5.4. Comsol, Inc., Los Altos, California.

Côté, J., Fillion, M.-H., and Konrad, J.-M. 2011. Intrinsic permeability of materials ranging from sand to rock-fill using natural air convection tests. Canadian Geotechnical Journal, **48**(5): 679–690. NRC Research Press. doi:10.1139/t10-097.

Côté, J., and Konrad, J.-M. 2005. Thermal conductivity of base-course materials. Canadian Geotechnical

Journal, **42**(1): 61–78. Canadian Science Publishing NRC Research Press, Ottawa, Ontario.

Coulombe, V., Bussière, B., Côté, J., and Garneau, P. 2012. Performance of insulation covers to control acid mine drainage in cold environment. *In* Proceedings of the 15th International Specialty Conference on Cold Regions Engineering. *Edited by* B. Morse and G. Doré. American Society of Civil Engineers, Quebec City, Quebec. pp. 789–799.

Das, B.M. 2013. Fundamentals of geotechnical engineering. *In* 4th edition. Cengage Learning, Stamford, Conneticut.

Davis, T.N. 2001. Permafrost: A guide to frozen ground in transition. University of Alaska Press, Fairbanks, Alaska.

DDMI. 2018. Interim Closure and Reclamation Plan – Waste Rock Storage Area – North Country Rock Pile – Version 1.2. DDMI, Yellowknife, Northwest Territories.

DDMI. 2021. Diavik Type A Water License Report - 2020. Yellowknife, Northwest Territories.

EBA. 2004. 2003 A154 Pit Lakebed Subsurface Investigation. Yellowknife, Northwest Territories.

Elberling, B. 2001. Environmental controls of the seasonal variation in oxygen uptake in sulfidic tailings deposited in a permafrost-affected area. Water Resources Research, **37**(1): 99–107. John Wiley & Sons, Inc. doi:https://doi.org/10.1029/2000WR900259.

Elberling, B. 2005. Temperature and oxygen control on pyrite oxidation in frozen mine tailings. Cold Regions Science and Technology, **41**(2): 121–133. Elsevier. doi:10.1016/j.coldregions.2004.09.004.

Elghali, A., Benzaazoua, M., Bouzahzah, H., Bussière, B., and Villarraga-Gómez, H. 2018. Determination of the available acid-generating potential of waste rock, Part I: Mineralogical approach. Applied Geochemistry, **99**(1): 31–41. doi:https://doi-org.login.ezproxy.library.ualberta.ca/10.1016/j.apgeochem.2018.10.021.

Elghali, A., Benzaazoua, M., Bussière, B., and Bouzahzah, H. 2019. Determination of the available acid-generating potential of waste rock, part II: Waste management involvement. Applied Geochemistry,

100(1): 316–325. doi:https://doi-org.login.ezproxy.library.ualberta.ca/10.1016/j.apgeochem.2018.12.010.

Environment Canada. 2018. Daily Data Report for Ekati A, Northwest Territories, Bulk Data 1998-2015. Available from http://climate.weather.gc.ca/historical_data/search_historic_data_e.html. [accessed 9 April 2018].

Environmental Modelling and Prediction P/L Australia (EMAP). 2008. Climate Change Impacts in the Diavik Region of Northern Canada.

Esch, D.C., and Osterkamp, T.E. 1990. Cold regions engineering: Climatic warming concerns for Alaska. Journal of Cold Regions Engineering, **4**(1): 6–14.

Farouki, O.T. 1981. Thermal Properties of Soils. Cold Regions Science and Technology, **5**(1): 67–75. United States Army Corps of Engineers, Hanover, New Hampshire.

Getling, A. V. 1998. Rayleigh-Bénard Convection: Structures and Dynamics. *In* Advanced Series in Nonlinear Dynamics. World Scientific Publishing Co., Singapore.

Godwaldt, R.C., Biggar, K.W., Sego, D.C., and Foght, J. 2000. AMD generation at sub-zero temperatures. *In* Proceedings of the Sixth International Conference on Environmental Issues and Management of Waste in Energy and Mineral Production. Balkema Publishers, Calgary, Alberta. pp. 557–563.

Goering, D.J., and Kumar, P. 1996. Winter-time convection in open-graded embankments. Cold Regions Science and Technology, **24**(1): 57–74. doi://doi.org/10.1016/0165-232X(95)00011-Y.

Golder. 2006. Report on - A21 Dike and Pit Geotechnical and Hydrogeological data interpretation - Diavik Diamond Mine. Vancouver, British Columbia.

Golder. 2017. Diavik Diamond Mine North Country Rock Pile Closure Design. Vancouver, British Columbia.

Government of Canada. 2019. Nominal GDP in the minerals sector. Available from https://www.nrcan.gc.ca/science-data/science-research/earth-sciences/earth-sciences-resources/earth-sciences-federal-programs/minerals-and-economy/20529#GDP. [accessed 29

December 2020].

Gruber, S., Burn, C., Harris, S., Smith, S.L., Bonnaventure, P., Arenson, L., Geertsema, M., and Benkert, B. 2015. Permafrost in mountainous regions of Canada. *In* 7th Canadian Permafrost Conference. Canadian Geotechnical Society, Richmond, British Columbia. p. 8.

Hartman, H.L., and Mutmansky, J.M. 2002. Introductory Mining Engineering. John Wiley & Sons, Inc., Hoboken, New Jersey.

Hawley, P.M., and Cunning, J. 2017. Guidelines for Mine Waste Dump and Stockpile Design. CSIRO Publishing, Clayton, Australia.

Heginbottom, J.A. 2002. Permafrost mapping: A review. Progress in Physical Geography, **26**(4): 623–642. doi:10.1191/0309133302pp355ra.

Heginbottom, J.A., Dubreuil, M.A., and Harker, P.T. 1995. Canada, Permafrost, MCR Series no. 4177, scale 1:7,500,000. *In* The National Atlas of Canada, 5th edition. Natural Resources Canada, Geomatics Canada, Ottawa, Ontario. p. 1.

Hendry, M.J. 1982. Hydraulic Conductivity of a Glacial Till in Albertaa. Groundwater, **20**(2): 162–169. John Wiley & Sons, Ltd. doi:https://doi.org/10.1111/j.1745-6584.1982.tb02744.x.

Holtz, R.D., Kovacs, W.D., and Sheahan, T.C. 2011. An Introduction to Geotechnical Engineering. *In* 2nd edition. Pearson, Upper Saddle River, New Jersey.

Horton, C.W., and Rogers, F.T. 1945. Convection Currents in a Porous Medium. Journal of Applied Physics, **16**(6): 367–370. American Institute of Physics. doi:10.1063/1.1707601.

IAND, Fisheries and Oceans, and Natural Resources Canada. 1999. Comprehensive Study Report: Diavik Diamonds Project. Government of Canada, Ottawa, Ontario.

INAP. 2017. Global Cover System Design, Technical Guidance Document.

IPA. 1998. Multi-language glossary of permafrost and related ground-ice terms (revision - 2005). *Edited by* R.O. van Everdingen. National Research Council Canada, Ottawa, Ontario.

Jaynes, D.B., Rogowski, A.S., and Pionke, H.B. 1984. Acid Mine Drainage From Reclaimed Coal Strip Mines (1. Model Description). Water Resources Research, **20**(2): 233–242.

Jiji, L.M. 2009. Heat conduction. *In* 3rd edition. Springer, Berlin, Germany.

Johansen, O. 1975. Thermal conductivity of soils. Ph.D. thesis, University of Trondheim, Trondheim, Norway. CRREL Draft English Translation 637, US Army Corps of Engineers, Cold Regions Research and Engineering Laboratory, Hanover, New Hampshire.

Joseph, D.D. 1976. Stability of fluid motions. I, II. NASA STI/Recon Technical Report A, **28**: 12423. Minneapolis, Minnesota.

Kersten, M.S. 1949. Thermal Properties of Soil. Engineering Experiment Station, Bulletin No. 28, **52**(21): 233. Minneapolis, Minnesota.

Langman, J.B., Veeramani, H., Blowes, D.W., Bailey, B.L., Wilson, D., Smith, L., Sego, D.C., Amos, R.T., and Holland, S.P. 2017. Waste Rock Biogeochemistry in a Permafrost Environment: Examination of a Cover Design for a Low-Sulfide, Granitic Waste Rock. Geomicrobiology Journal, **34**(8): 656–669. Taylor & Francis. doi:10.1080/01490451.2016.1238978.

Lapwood, E.R. 1948. Convection of a fluid in a porous medium. Mathematical Proceedings of the Cambridge Philosophical Society, **44**(4): 508–521. Cambridge University Press. doi:DOI: 10.1017/S030500410002452X.

Lessard, F., Bussière, B., Côté, J., Benzaazoua, M., Boulanger-Martel, V., and Marcoux, L. 2018. Integrated environmental management of pyrrhotite tailings at Raglan Mine: Part 2 desulphurized tailings as cover material. Journal of Cleaner Production, **186**(1): 883–893. doi://doi.org/10.1016/j.jclepro.2018.03.132.

Lu, N. 2001. An analytical assessment on the impact of covers on the onset of air convection in mine wastes. International Journal for Numerical and Analytical Methods in Geomechanics, **25**(4): 347–364. John Wiley & Sons, Inc., Golden, Colorado.

Lunardini, V.J. 1981. Heat Transfer in Cold Climates. Van Nostrand Reinhold Company, New York, New

York.

MAC. 2009. Progress Report - Towards Sustainable Mining. MAC, Ottawa, Ontario.

MEND. 2017. About Us. Available from http://mend-nedem.org/default/. [accessed 4 May 2018].

MEND1.20.1. 2009. Prediction Manual for Drainage Chemistry from Sulphidic Geologic Materials. Smithers, British Columbia.

MEND1.61.2. 1996. Acid Mine Drainage in permafrost regions: issues, control strategies and research requirements. Department of Indian and Northern Affairs Canada, Ottawa, Ontario.

MEND1.61.4. 2004. Covers for Reactive Tailings Located in Permafrost Regions Review. I. Holubec Consulting Inc., Oakville, Ontario.

MEND1.61.7. 2011. Climate Change and Acid Rock Drainage - Risks for the Canadian Mining Sector. Stratos Inc., Ottawa, Ontario.

MEND5.8.1. 1995. Economic Evaluation of Acid Mine Drainage Technologies. GEOCON, Willowdale, Ontario.

Neuner, M. 2009. Water flow through unsaturated mine waste rock in a region of permafrost. M.Sc. thesis, Department of Earth, Ocean and Atmospheric Sciences, University of British Columbia, Vancouver, British Columbia.

Neuner, M., Smith, L., Blowes, D.W., Sego, D.C., Smith, L.J.D., Fretz, N., and Gupton, M. 2013. The Diavik waste rock project: Water flow through mine waste rock in a permafrost terrain. Applied Geochemistry, **36**(1): 222–233. doi:10.1016/j.apgeochem.2012.03.011.

Nield, D.A., and Bejan, A. 2006. Convection in porous media. *In* 3rd edition. Springer Science+Business Media, New York, New York.

Nordstrom, D., and Alpers, C.N. 1999. Negative pH, efflorescent mineralogy, and consequences for environmental restoration at the Iron Mountain Superfund site, California. Proceedings of the National Academy of Sciences of the United States of America, **96**(7): 3455–3462. The National Academy of

Sciences. doi:10.1073/pnas.96.7.3455.

Nordstrom, D., and Southam, G. 1997. Geomicrobiology of sulfide mineral oxidation. *In* Geomicrobiology: interactions between microbes and minerals. *Edited by* J.F. Banfield and K.H. Nealson. Mineralogical Society of America, Washington, D.C. pp. 361–390.

Pham, N.H. 2013. Heat transfer in waste-rock piles constructed in a continuous permafrost region. Ph.D. thesis, Department of Civil and Environmental Engineering, University of Alberta, Edmonton, Alberta.

Pham, N.H., and Sego, D.C. 2013. Numerical simulations of air convection cover for mine tailings of Lupin Mine. *In* Proceedings of the International Conference on Tailings and Mine Waste 2013. University of Alberta, Banff, Alberta. pp. 569–577.

Rayleigh, Lord. 1916. LIX. On convection currents in a horizontal layer of fluid, when the higher temperature is on the under side. The London, Edinburgh, and Dublin Philosophical Magazine and Journal of Science, **32**(192): 529–546. Taylor & Francis. doi:10.1080/14786441608635602.

Robertson, A.M. 1987. Alternative acid mine drainage abatement measures. *In* Proceedings of the 11th Annual British Columbia Mine Reclamation Symposium. Robertson GeoConsultants, Campbell River, British Columbia. pp. 71–101.

Shigley, J.E., Shor, R., Padua, P., Breeding, C.M., Shirey, S.B., and Ashbury, D. 2016. Mining Diamonds in the Canadian Arctic: The Diavik Mine. Gems & Gemology, **52**(2): 104–131. doi:10.5741/fgems.52.2.104.

Smith, L.J.D., Blowes, D.W., Jambor, J.L., Smith, L., Sego, D.C., and Neuner, M. 2013a. The Diavik Waste Rock Project: Particle size distribution and sulfur characteristics of low-sulfide waste rock. Applied Geochemistry, **36**(1): 200–209. doi:10.1016/j.apgeochem.2013.05.006.

Smith, L.J.D., Moncur, M.C., Neuner, M., Gupton, M., Blowes, D.W., Smith, L., and Sego, D.C. 2013b. The Diavik Waste Rock Project: Design, construction, and instrumentation of field-scale experimental waste-rock piles. Applied Geochemistry, **36**: 187–199. doi:10.1016/j.apgeochem.2011.12.026.

Smith, L.J.D., Neuner, M., Gupton, M., Moore, M., Bailey, B.L., Blowes, D.W., Smith, L., and Sego, D.C.

2009. Diavik waste rock research project: From the Laboratory to the Canadian Arctic. *In* 8th International Conference on Acid Rock Drainage (ICARD) and Securing the Future: Mining, Metals and the Environment in a Sustainable Society. Curran Associates, Inc., Skelleftea, Sweden. pp. 40–50.

Smith, S.L. 2011. Trends in permafrost conditions and ecology in northern Canada. *In* Canadian Biodiversity: Ecosystem Status and Trends 2010. Canadian Council of Resource Ministers, Ottawa, Ontario.

Smith, S.L., and Burgess, M.M. 2000. Ground temperature database for northern Canada. Government of Canada.

Smith, S.L., and Burgess, M.M. 2004. Sensitivity of permafrost to climate warming in Canada. Geological Survey of Canada, Ottawa, Ontario.

Stockwell, J., Smith, L., Jambor, J.L., and Beckie, R. 2006. The relationship between fluid flow and mineral weathering in heterogeneous unsaturated porous media: A physical and geochemical characterization of a waste-rock pile. Applied Geochemistry, **21**(8): 1347–1361. doi:10.1016/j.apgeochem.2006.03.015.

Terzaghi, K., Peck, R.B., and Mesri, G. 1996. Soil Mechanics in Engineering Practice. *In* 3rd edition. John Wiley & Sons, Inc., New York, New York.

Tetra Tech Canada Inc. 2017. Thermal evaluation of Type III Rock Closure Cover at North Country Rock Pile, Diavik Diamond Mine, NT, Canada. Edmonton, Alberta.

Vick, S.G. 1990. Planning, Design, and Analysis of Tailings Dams. BiTech Publishers Ltd, Vancouver, British Columbia.

Wagner, D. 2008. Microbial communities and processes in arctic permafrost environments. *In* Microbiology of Extreme Soils. *Edited by* P. Dion and C.S. Nautiyal. Springer Science+Business Media, Berlin, Germany. pp. 133–154.

Walker, D.A., Jia, G.J., Epstein, H.E., Raynolds, M.K., Chapin Iii, F.S., Copass, C., Hinzman, L.D.,

Knudson, J.A., Maier, H.A., and Michaelson, G.J. 2003. Vegetation-soil-thaw-depth relationships along a low-arctic bioclimate gradient, Alaska: Synthesis of information from the ATLAS studies. Permafrost and Periglacial Processes, **14**(2): 103–123. John Wiley & Sons, Inc. doi:10.1002/ppp.452.

Weeks, B., and Wilson, G.W. 2006. Prediction of evaporation from soil slopes. Canadian Geotechnical Journal, **43**(8): 815–829. NRC Research Press. doi:10.1139/t06-049.

Wicky, J., and Hauck, C. 2017. Numerical modelling of convective heat transport by air flow in permafrost talus slopes. Cryosphere, **11**(3): 1311–1325. doi:10.5194/tc-11-1311-2017.

Wicky, J., and Hauck, C. 2020. Air Convection in the Active Layer of Rock Glaciers. Frontiers in Earth Science, **8**(August): 1–17. doi:10.3389/feart.2020.00335.

Wilson, G.W. 2008. Why Are We Still Struggling Acid Rock Drainage? Geotechnical News,: 51–56. BiTech Publishers Ltd, Richmond, British Columbia.

WLWB. 2015. W2015L2-0001 Water Use and Waste Disposal Licence, A, Northwest Territories 05, Lac de Gras, NT. Yellowknife, Northwest Territories.

Yanhu, M., Wei, M., Fujun, N., Yongzhi, L., Richard, F., and Yunchen, M. 2018. Long-Term Thermal Effects of Air Convection Embankments in Permafrost Zones: Case Study of the Qinghai–Tibet Railway, China. Journal of Cold Regions Engineering, **32**(4): 5018004. American Society of Civil Engineers. doi:10.1061/(ASCE)CR.1943-5495.0000166.

Yi, X., Su, D., Bussière, B., and Mayer, K.U. 2021. Thermal-hydrological-chemical modeling of a covered waste rock pile in a permafrost region. Minerals, **11**(6). MDPI AG. doi:10.3390/min11060565.

Younger, P.L., Banwart, S.A., and Hedin, R.S. 2002. Mine Water - Hydrology, Pollution, Remediation. *In* Environmental Pollution Book Series, Volume 5. Springer Science+Business Media, Dordrecht, Netherlands.

Zhang, T. 2005. Influence of the seasonal snow cover on the ground thermal regime: An overview. Reviews of Geophysics, **43**(4): 1–23. doi:10.1029/2004RG000157.

Appendix A Model Set-up Guide

Guide format legend:

Italicized → Open to select (drop-down or click)

Bold → Text to input

Underlined → Action (copy and paste)

- Open and Startup
- Open COMSOL Multiphysics 5.4
- New → Select *Model Wizard*
- Space Dimension → *2D*
- Select *Physics*
  - *Fluid Flow/Porous Media and Subsurface Flow/Darcy's Law (dl), Add*
  - *Heat Transfer/Heat Transfer in Porous Media (ht), Add*
- Select *Study*
  - *General Studies/Time Dependent*, *Add*

A.1 Global Definitions

A.1.1 Parameters 1

- Parameters 1 → Copy and paste parameters from Appendix Table A - 1

A.1.2 Interpolation

- See Appendix Figure A - 1
- *Functions/Variables, Utilities, Interpolation*
  - Label = **Interpolation 1 - FD3, July 2015**
    - Note: interpolated data set for initial temperature
  - Data Source = *Local Table*
  - Function Name = **int1**
  - Interpolation 1 → Copy and paste parameters from Appendix Table A - 2
  - Interpolation and Extrapolation
    - Interpolation = *Piecewise cubic*
    - Extrapolation = *Linear*

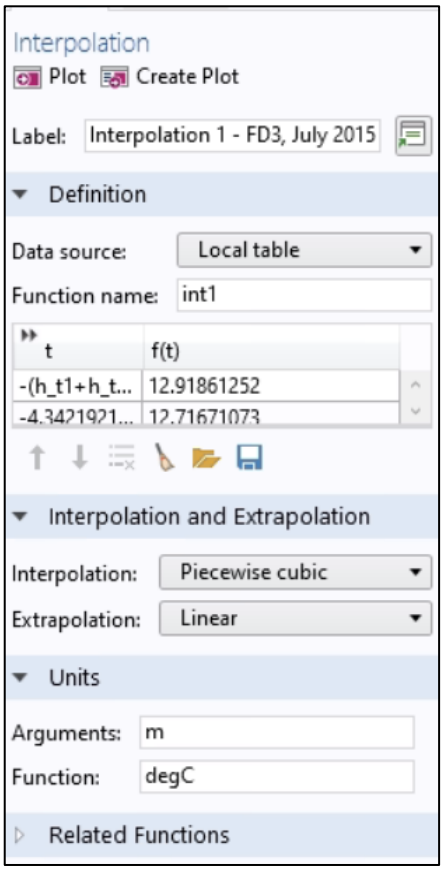

Appendix Figure A - 1: Interpolation 1 Inputs

- Units
  - Arguments = **m**
  - Function = **degC**

A.2 Component 1 (comp 1)

A.2.1 Geometry 1

A.2.1.1 Rectangle 1

- See Appendix Figure A - 2
- *Geometry, Rectangle*
- Label = **Rectangle 1**
- Object Type
  - Type = *Solid*
- Size and Shape
  - Width = **model_width**
  - Height = **h_t3**
- Position
  - Base = *Corner*
  - x = **base_x-(model_width)/2**
  - y = **h_t3**
- Rotation Angle
  - Rotation = **0**

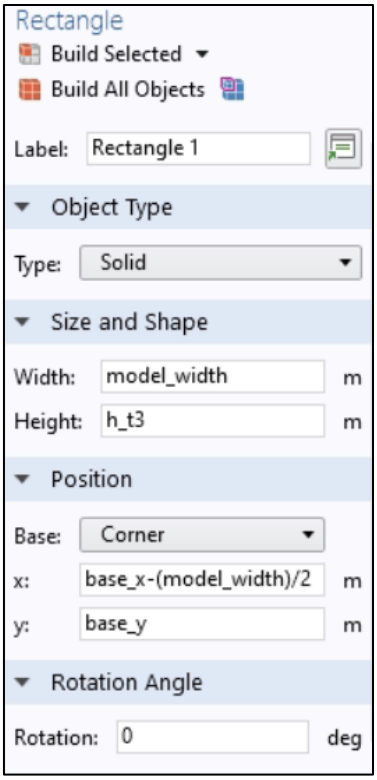

Appendix Figure A - 2: Rectangle 1 Inputs

A.2.1.2 Rectangle 2

- See Appendix Figure A - 3
- *Geometry, Rectangle*
- Label = **Rectangle 2**
- Object Type
  - Type = *Solid*
- Size and Shape
  - Width = **model_width**
  - Height = **h_till**
- Position
  - Base = *Corner*
  - x = **base_x-(model_width)/2**

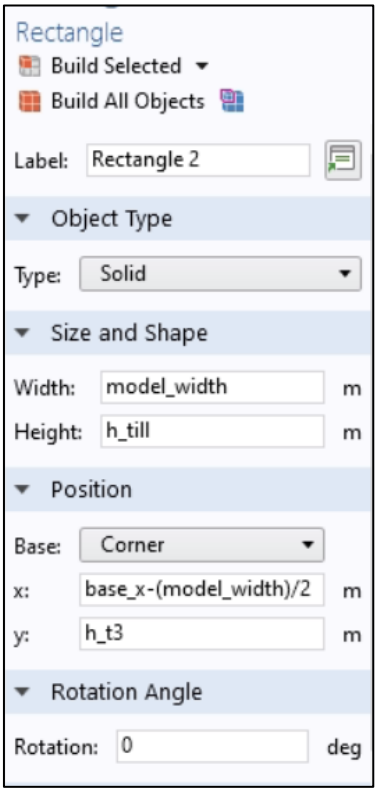

Appendix Figure A - 3: Rectangle 2 Inputs

    - y = **h_t3**
- Rotation Angle
    - Rotation = **0**

A.2.1.3 Rectangle 3

- See Appendix Figure A - 4
- *Geometry, Rectangle*
- Label = **Rectangle 3**
- Object Type
    - Type = *Solid*
- Size and Shape
    - Width = **model_width**
    - Height = **h_t1**
- Position
    - Base = *Corner*
    - x = **base_x-(model_width)/2**
    - y = **h_t3+h_till**

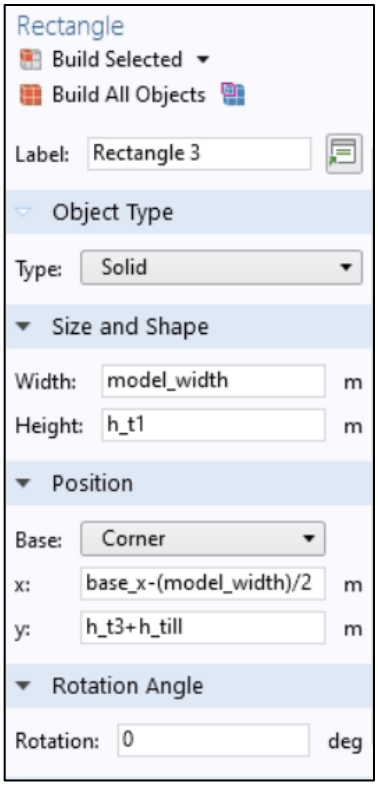

Appendix Figure A - 4: Rectangle 3 Inputs

A.2.1.4 Point 1

- See Appendix Figure A - 5
- *Geometry, Point*
- Label = **Point 1**
- Point
    - x = **base_x**
    - y = **h_t3+h_till+h_t1**

A.2.1.5 Point 2

- See Appendix Figure A - 6
- *Geometry, Point*
- Label = **Point 2**
- Point
    - x = **base_x**
    - y = **h_t3+h_till**

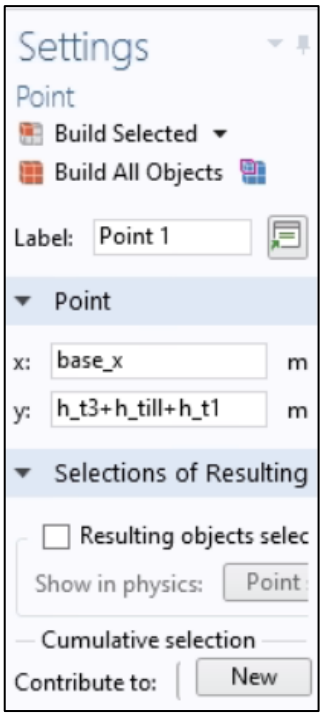

Appendix Figure A - 5: Point 1 Inputs

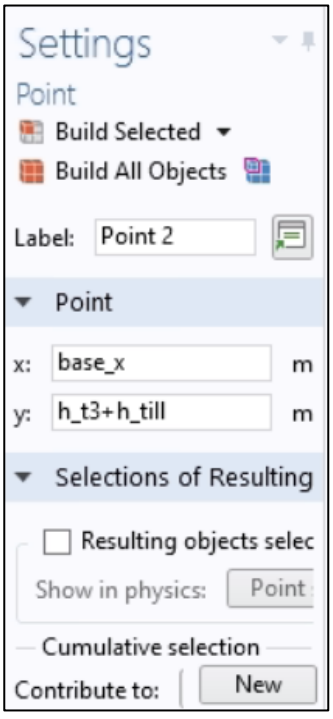

Appendix Figure A - 6: Point 2 Inputs

A.2.1.6 Point 3

- See Appendix Figure A - 7
- *Geometry, Point*
- Label = **Point 3**
- Point
  - x = **base_x**
  - y = **h_t3+h_till+h_t1*(0.5)**

A.2.1.7 Point 4

- See Appendix Figure A - 8
- *Geometry, Point*
- Label = **Point 4**
- Point
  - x = **base_x**
  - y = **h_t3**

Build All Selected

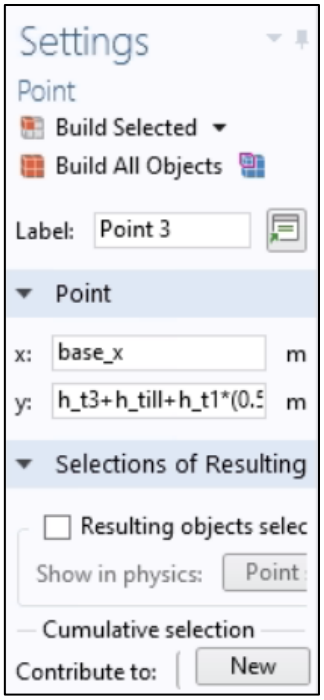

Appendix Figure A - 7: Point 3 Inputs

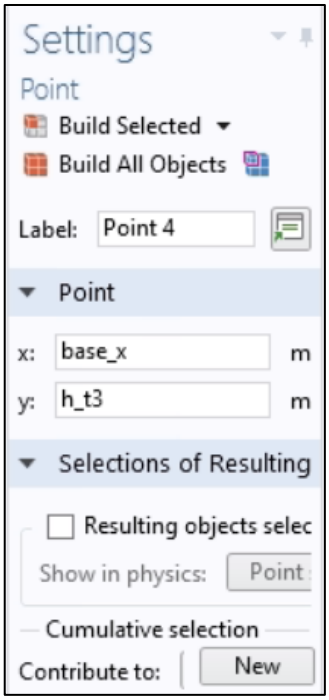

Appendix Figure A - 8: Point 4 Inputs

A.2.2 Definitions

A.2.2.1 Variables 1

- *Definition, Variables 1*
  - Copy and paste variables from Appendix Table A - 3

A.2.2.2 Convection_Top

- *Definition, Variables 2*
  - Label = **Convection_Top**
  - Geometric Entity Selection
    - Geometric entity level = *Point*
    - Selection = *Manual*
    - Point 8 (Appendix Figure A - 9)
  - Variables
    - Name = **temp_top**
    - Expression = **T**

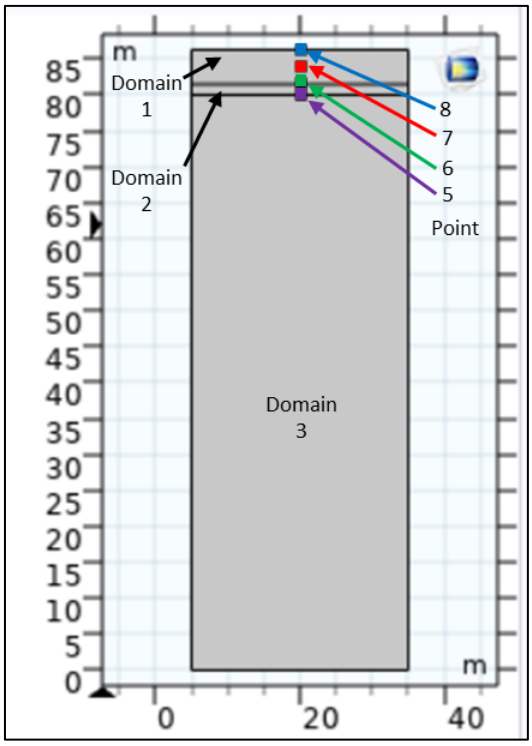

Appendix Figure A - 9: Domain and Points of Geometry

        - Description = **Temperature at top of convection layer**

A.2.2.3 Convection_Bot

- *Definition, Variables 3*
    - Label = **Convection_Bot**
    - Geometric Entity Selection
        - Geometric entity level = *Point*
        - Selection = *Manual*
        - Point 6 (Appendix Figure A - 9)
    - Variables
        - Name = **temp_bot**
        - Expression = **T**
        - Description = **Temperature at bottom of convection layer**

A.2.2.4 Average 1

- *Definition, Component Couplings/Average 1*
    - Label = **Average 1**
    - Operator name: **opBot**
    - Source Selection
        - Geometric entity level = *Point*
        - Point 6 (Appendix Figure A - 9)

A.2.2.5 Average 2

- *Definition, Component Couplings/Average 2*
    - Label = **Average 2**
    - Operator name: **opTop**
    - Source Selection
        - Geometric entity level = *Point*
        - Point 8 (Appendix Figure A - 9)

A.2.2.6 Maximum 1

- *Definition, Component Couplings/Maximum*
    - Label = **Maximum 1**
    - Operator name: **maxop1**
    - Source Selection
        - Geometric entity level = *Point*

- Point 5 (Appendix Figure A - 9)

A.2.3 Materials

A.2.3.1 Type III (mat1)

- *Materials, Blank Material 1*
- Label = Type III
  - Geometric entity level = *Domain*
  - Selection = *Manual*
  - Domain = Domain 1 (Appendix Figure A - 9)
- Material Contents
  - Density = **rho_s**
  - Porosity = **poro**
  - Heat capacity at constant pressure = **((cs_iii_f*(1-H)+cs_iii_u*H))+D*beta_wf*gmc_waste**
  - Thermal conductivity = **kiii**
  - Permeability = **perm_t3**

A.2.3.2 Till (mat2)

- *Materials, Blank Material 2*
- Label = **Till**
  - Geometric entity level = *Domain*
  - Selection = *Manual*
  - Domain = Domain 2 (Appendix Figure A - 9)
- Material Contents
  - Density = **rho_bulk_till**
  - Porosity = **poro_till**
  - Heat capacity at constant pressure = **(cs_till_f*(1- H)+cs_till_u*H)+D*beta_wf*gmc_till**
  - Thermal conductivity = **ktillf*(1-H)+ktillu*(H)**
  - Permeability = **perm_till**

A.2.3.3 Type I (Coarse) (mat3)

- *Materials, Blank Material 3*
- Label = **Type I (Coarse)**
- Geometric Entity Selection

    - Geometric entity level = *Domain*
    - Selection = *Manual*
    - Domain = Domain 3 (Appendix Figure A - 9)
        - Note: depending on choice this can be T1 (coarse) or T1
- Material Contents
    - Density = **rho_bulk_ic**
    - Porosity = **poro_tic**
    - Heat capacity at constant pressure = **cs_ic**
    - Thermal conductivity = **ki_c**
    - Permeability = **perm_t1c**

A.2.3.4 Type I (mat4)

- *Materials, Blank Material 4*
- Label = **Type I**
- Geometric Entity Selection
    - Geometric entity level = *Domain*
    - Selection = *Manual*
    - Domain = Domain 3 (Appendix Figure A - 9)
        - Note: depending on choice this can be T1 (coarse) or T1
- Material Contents
    - Density = **rho_s**
    - Porosity = **poro**
    - Heat capacity at constant pressure = **(cs_i_f*(1-H)+cs_i_u*H)+D*beta_wf*gmc_waste**
    - Thermal conductivity = **ki**
    - Permeability = **perm_t1**

A.2.3.5 Air_custom (mat5)

- *Materials, Blank Material 5*
- Label = **Air_custom**
- Geometric Entity Selection
    - Geometric entity level = *Domain*
    - Selection = *Manual*
    - Domain = No selection
- Material Properties

    - Material type: *Nonsolid*
    - *Basic Properties*
        - *Density, Add*
        - *Dynamic Viscosity, Add*
        - *Heat Capacity at Constant Pressure, Add*
        - *Ratio of Specific Heats, Add*
        - *Thermal Conductivity, Add*
- Material Contents
    - Density = **rho_air**
    - Dynamic viscosity = **-8.38278E-7[Pa*s]+8.35717342E-8[Pa*s]*(T[1/K])^1-7.69429583E-11[Pa*s]*(T[1/K])^2+4.6437266E-14[Pa*s]*(T[1/K])^3-1.06585607E-17[Pa*s]*(T[1/K])^4**
    - Heat capacity at constant pressure = **1047.63657[J/(kg*K)]-0.372589265[J/(kg*K)]*(T[1/K])^1+9.45304214E-4[J/(kg*K)]*(T[1/K])^2-6.02409443E-7[J/(kg*K)]*(T[1/K])^3+1.2858961E-10[J/(kg*K)]*(T[1/K])^4**
    - Ratio of specific heats = **1.4**
    - Thermal conductivity = **-0.00227583562[W/(m*K)]+1.15480022E-4[W/(m*K)]*(T[1/K])^1-7.90252856E-8[W/(m*K)]*(T[1/K])^2+4.11702505E-11[W/(m*K)]*(T[1/K])^3-7.43864331E-15[W/(m*K)]*(T[1/K])^4**

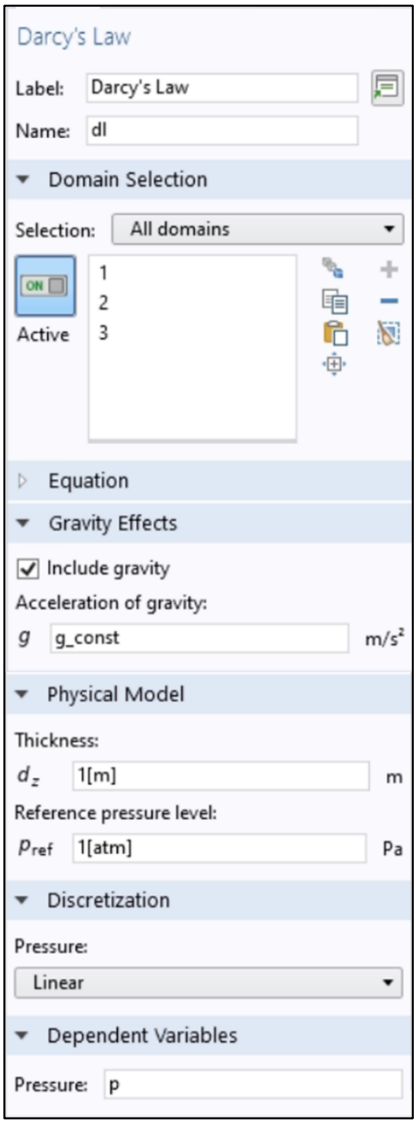

Appendix Figure A - 10: Darcy's Law Inputs

A.2.4 Darcy's Law (dl)

- See Appendix Figure A - 10.
- Label = **Darcy's Law**
- Name = **dl**
- Domain Selection = *All domains (1, 2, and 3)*
- Gravity Effects
    - Darcy's Law (dl), *Include gravity*
    - Acceleration of gravity = **g_const**
- Physical Model

    - Thickness = **1[m]**
    - Reference pressure level = **1[atm]**
- Discretization
    - Pressure = *Linear*
- Dependent Variables
    - Pressure = **p**

A.2.4.1 Fluid and Matrix Properties 1

- See Appendix Figure A - 11
- Domain Selection
    - Domain Selection = 1, 2, 3 (All Domains)
- Coordinate System Selection
    - Coordinate system = *Global coordinate system*
- Fluid Properties
    - Fluid material = *Air_Custom (mat5)*
    - Density = *From material*
    - Dynamic Viscosity = *From material*
- Matrix Properties
    - Porous material = *Domain material*
    - Porosity = *From material*
    - Permeability model = *Permeability,*
        - Permeability = *From material*

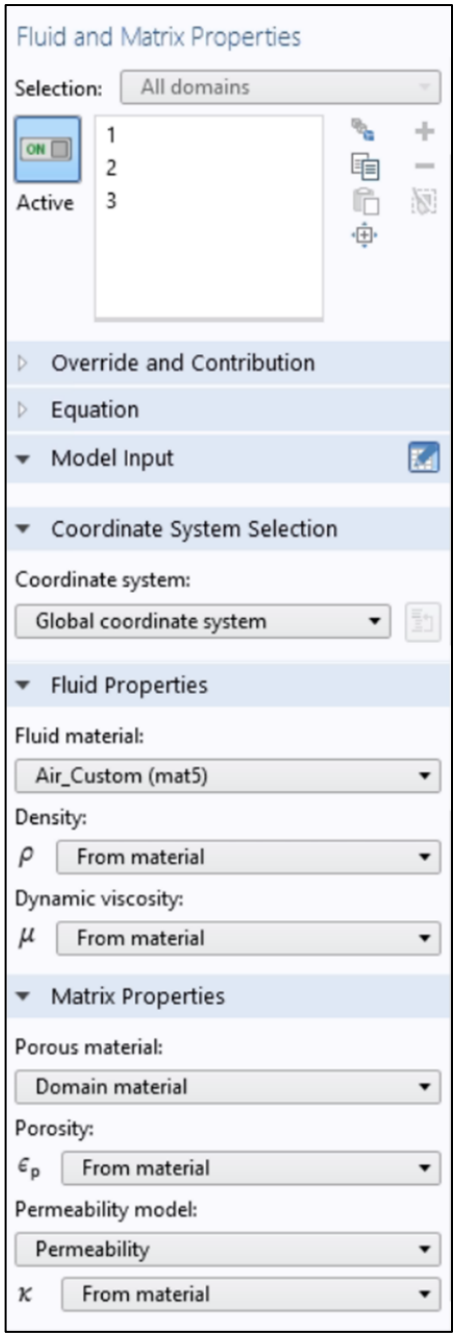

Appendix Figure A - 11: Fluid and Matrix Properties Inputs (Darcy's Law)

A.2.4.2 Initial Values 1

- See Appendix Figure A - 12
- Domain Selection
  - Domain Selection = 1, 2, 3 (All Domains)
- Initial Values
  - Pressure = **Patm-1.27[kg/m^3]*g_const*y**

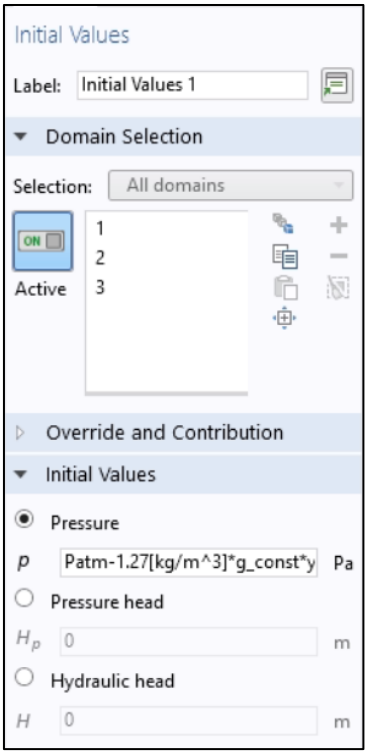

Appendix Figure A - 12: Initial Value Inputs (Darcy's Law)

A.2.4.3 Gravity

- See Appendix Figure A - 13
- Coordinate System Selection
  - Coordinate system = *Global coordinate system*
- Gravity
  - Specify = *Acceleration*
  - Gravity vector:
    - x = **0**
    - y = **-g_const**

A.2.4.4 No Flow 1

- See Appendix Figure A - 14
- Boundary Selection = 1, 2, 3, 5, 11, 12, 15 (both sides and bottom)
  - Note: No changes will be needed, these other boundaries were overridden or not applicable given previous selections

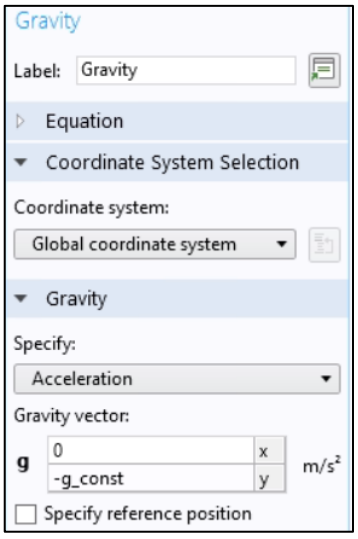

Appendix Figure A - 13: Gravity Inputs (Darcy's Law)

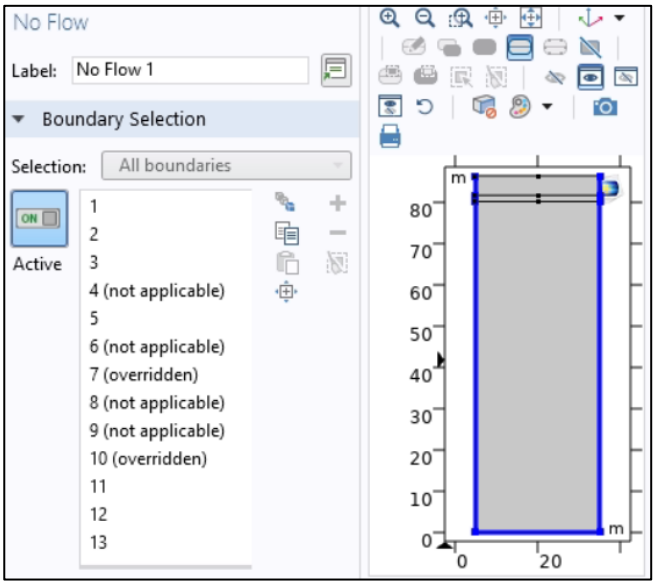

Appendix Figure A - 14: No Flow 1 Inputs (Darcy's Law)

A.2.4.5 Pressure 1

- See Appendix Figure A - 15
- Add *Pressure*
- Boundary Selection
- Selection = *manual*
- Boundaries 7, 10 (top surface)
- Pressure
  - P_0 = **Ps**

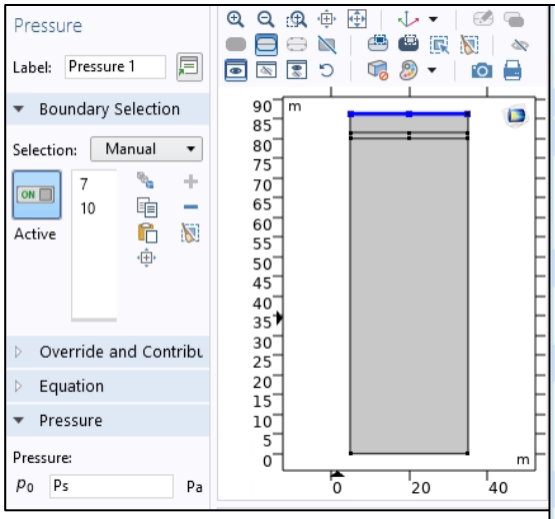

Appendix Figure A - 15: Pressure 1 Inputs (Darcy's Law)

A.2.5 Heat Transfer in Porous Media (ht)

A.2.5.1 Porous Medium 1

- See Appendix Figure A - 16
- Domain Selection
  - *1, 2, and 3 (All domains)*
- Coordinate System Selection
  - Coordinate system = *Global coordinate system*
- Fluid Material
  - Select *Air_Custom (mat5)*
- Heat Conduction, Fluid
  - Thermal conductivity = *From material*
- Thermodynamics, Fluid
  - Fluid type = *Gas/Liquid*
  - Density = *From Material*
  - Heat capacity at constant pressure = *From material*
  - Ratio of specific heats = *From material*
- Immobile Solids
  - Solid material = *Domain material*
  - Volume fraction = *Volume fraction (dl/dlm1)*
- Heat Conduction, Porous Matrix
  - Thermal conductivity = *From Material*

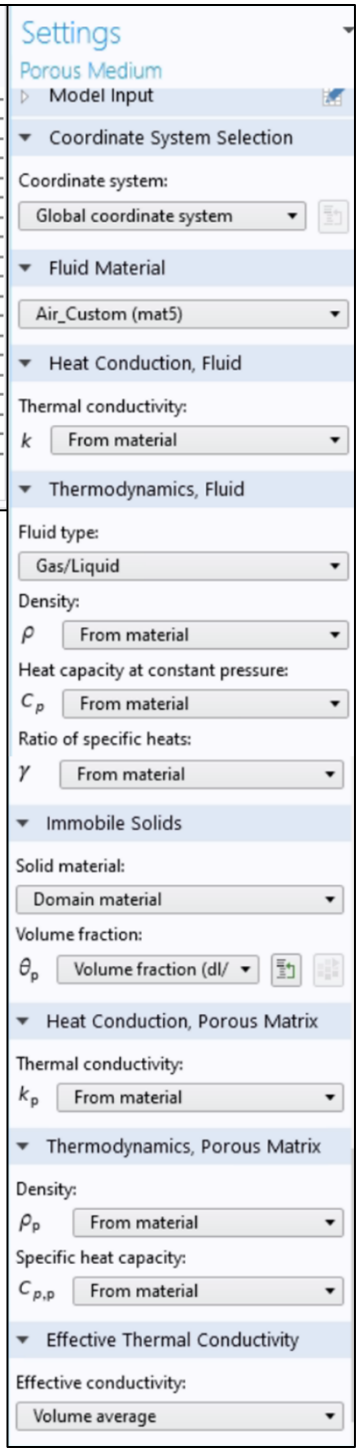

Appendix Figure A - 16: Porous Media Inputs (Heat Transfer)

- Thermodynamics, Porous Matrix
    - Density = *From Material*
    - Specific heat capacity = *From Material*
- Effective Thermal Conductivity
    - Effective conductivity = *Volume Average*

A.2.5.2 Initial Values 1

- See Appendix Figure A - 17
- Domain Selection
    - 1, 2, and 3 (All domains)
- Initial Values
    - Temperature
        - *User Defined*
        - T = **int1(80-y)**

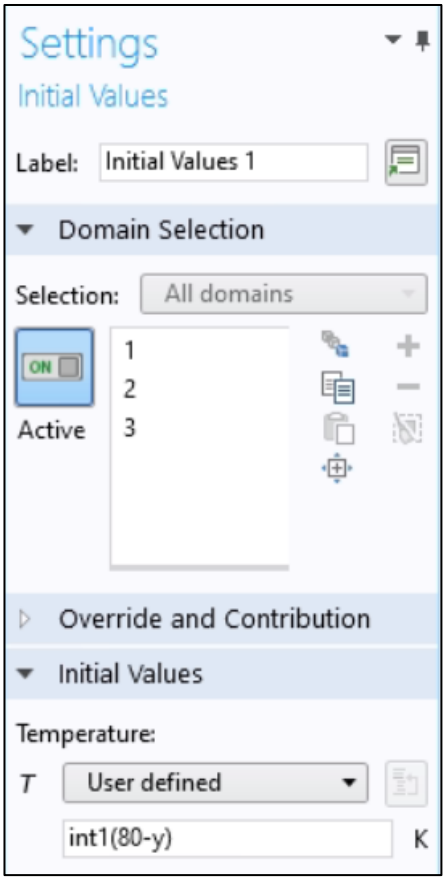

Appendix Figure A - 17: Initial Values (Heat Transfer)

A.2.5.3 Thermal Insulation 1

- See Appendix Figure A - 18
- Boundary Selection = 1, 2, 3, 5, 11, 12, 15 (both sides and bottom)
    - Note: No changes will be needed, these other boundaries were overridden or not applicable given previous selections

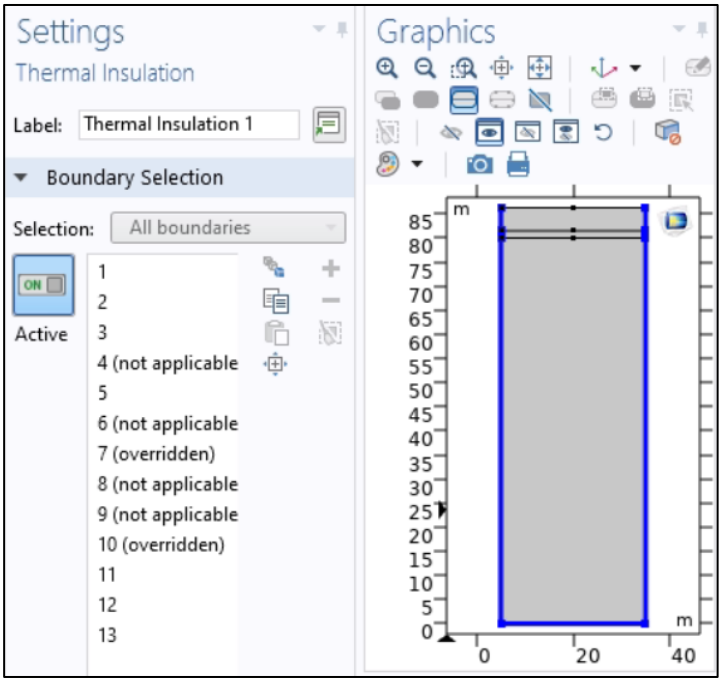

Appendix Figure A - 18: Thermal Insulation (Heat Transfer)

A.2.5.4 Temperature 1

- See Appendix Figure A - 19
- Add *Temperature*
- Label = **Temperature 1**
- Boundary Selection
    - Selection = *Manual*
    - Boundary 7, 10
- Temperature
    - *User Defined*
    - T_o = **Ts**

A.2.6 Multiphysics

- *Flow Coupling*, Add
  - Source = *Darcy's Law (dl)*
  - Destination = *Heat Transfer in Porous Media (ht)*
- *Temperature Coupling*, *Add*
  - Source = *Heat Transfer in Porous Media (ht)*
  - Destination = *Darcy's Law (dl)*

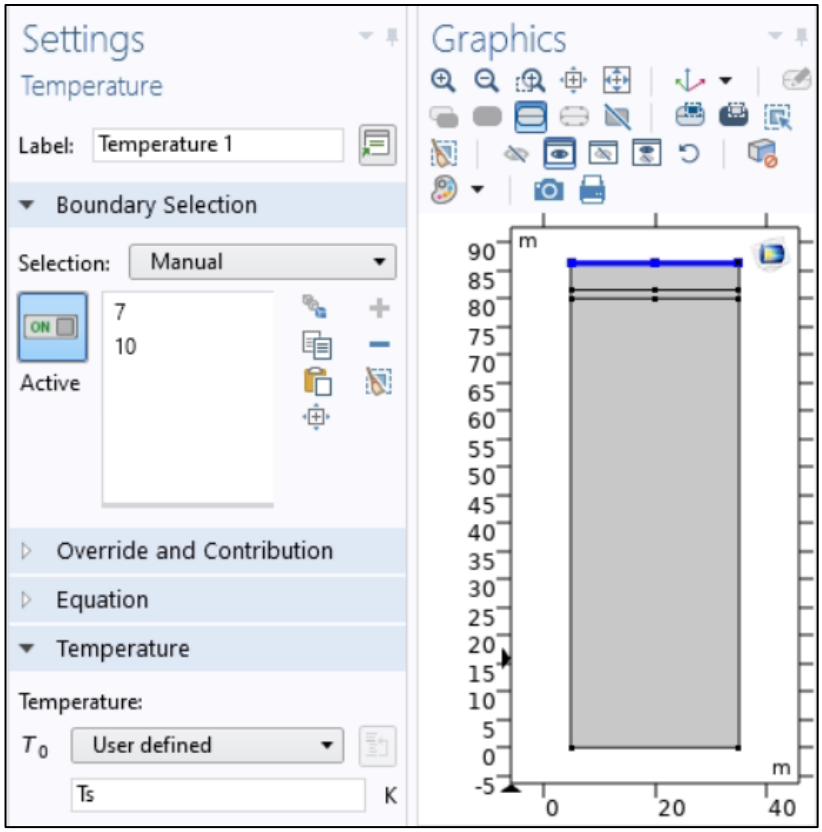

Appendix Figure A - 19: Temperature (Heat Transfer)

A.2.7 Mesh 1

- Sequence type = *User-controlled mesh*

A.2.7.1 Size

- See Appendix Figure A - 20
- Right-click Mesh, *Size*, Add
- Label = **Size**
- Element Size
  - Calibrate for = *General physics*
  - Select *Custom*
- Element Size Parameters
  - Maximum element size = **20**
  - Minimum element size = **0.001**
  - Maximum element growth rate = **1.3**
  - Curvature factor = **0.3**
  - Resolution of narrow regions = **1**

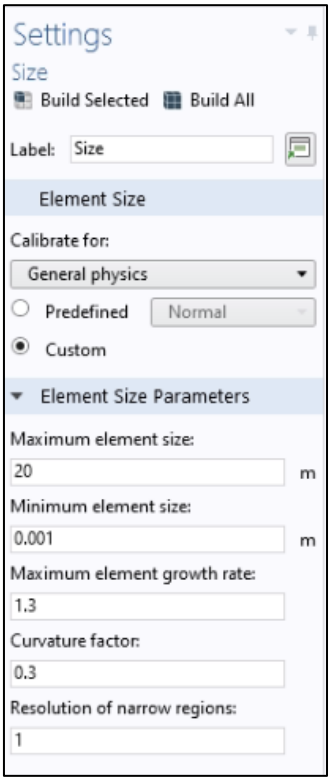

Appendix Figure A - 20: Mesh Inputs, Size

A.2.7.2 Branch set-up

- Branch set up as seen in Appendix Figure A - 21
- Right-click Mesh 1, *Size*, Add
- Right-click Mesh 1, *Free Triangular*, Add
- Right-click Free Triangular 1, *Size*, Add
- Right-click Free Triangular 1, *Distribution*, Add
- Right-click Free Triangular 1, *Distribution*, Add
- Right-click Mesh 1, *Free Triangular*, Add
- Right-click Free Triangular 2, *Size*, Add
- Right-click Free Triangular 1, *Distribution*, Add

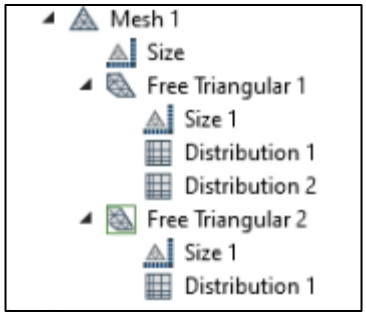

Appendix Figure A - 21: Mesh branch set-up

A.2.7.3 Mesh 1

- Label = **Mesh 1**
- Mesh Settings
    - Sequence type = *User-controlled mesh*

A.2.7.4 Mesh 1/Size

- Label = **Size**
- Element Size
    - Calibrate for = *General physics*
    - Select Custom
- Element Size Parameters
    - Maximum element size = **20**
    - Minimum element size = **0.001**
    - Maximum element growth rate = **1.3**
    - Curvature factor = **0.3**
    - Resolution of narrow regions = **1**

A.2.7.5 Mesh 1/Free Triangular 1

- Label = **Free Triangular 1**
- Domain Selection
    - Geometric entity level = *Domain*
    - Selection = *Manual*
    - Selection = *Domain 3* (Appendix Figure A - 9)
- Scale Geometry

- x-direction scale = **1**
- y-direction scale = **1**

- Control Entities
  - Select Smooth across removed control entities
  - Number of iterations = **8**
  - Maximum element depth to process = **8**
- Tessellation
  - Method = *Automatic*

A.2.7.6 Mesh 1/Free Triangular 1/Size 1

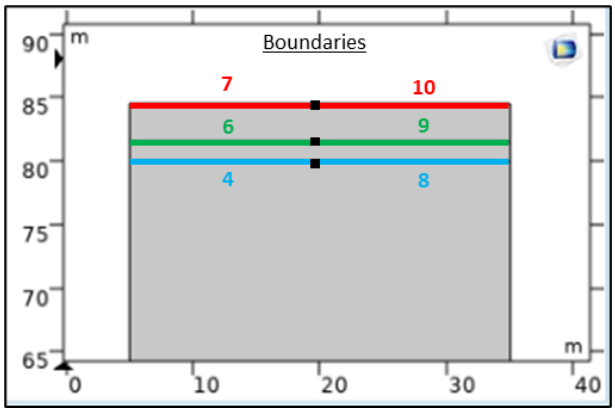

Appendix Figure A - 22: Boundary Labels

- Label = **Size 1**
- Geometric Entity Selection
  - Geometric entity level = *Domain*
  - Selection = *Manual*
  - Selection = *Domain 3* (Appendix Figure A - 9)
- Element Size
  - Calibrate for = *General physics*
  - Select Custom
- Element Size Parameters
  - Select *Maximum element size*
  - Maximum element size = **t1_mesh_max**
  - Select *Minimum element size*
  - Maximum element size = **t1_mesh_min**

A.2.7.7 Mesh 1/Free Triangular 1/Distribution 1

- Label = **Distribution 1**
- Boundary Selection
  - Selection = *Manual*
  - Select boundaries 7 and 10 (upper boundary, see Appendix Figure A - 22)
- Distribution
  - Distribution type = *Fixed number of elements*
  - Number of elements = **mesh_dist**

A.2.7.8 Mesh 1/Free Triangular 1/Distribution 2

- Label = **Distribution 2**
- Boundary Selection
    - Selection = *Manual*
    - Select boundaries 6 and 9 (bottom of T1 boundary, see Appendix Figure A - 22)
- Distribution
    - Distribution type = *Fixed number of elements*
    - Number of elements = **floor(mesh_dist/2)**

A.2.7.9 Mesh 1/Free Triangular 2

- Label = **Free Triangular 2**
- Domain Selection
    - Geometric entity level = *Domain*
    - Selection = *Manual*
    - Selection = *Domain 1 and 2* (Appendix Figure A - 9)
- Scale Geometry
    - x-direction scale = **1**
    - y-direction scale = **1**
- Control Entities
    - Select *Smooth across removed control entities*
    - Number of iterations = **8**
    - Maximum element depth to process = **8**
- Tessellation
    - Method = *Automatic*

A.2.7.10 Mesh 1/Free Triangular 2/Size 1

- Label = **Size 1**
- Geometric Entity Selection
    - Geometric entity level = *Domain*
    - Selection = *Manual*
    - Selection = *Domain 1 and 2* (Appendix Figure A - 9)
- Element Size
    - Calibrate for = *General physics*
    - Select *Custom*
- Element Size Parameters

- Select *Maximum element size*
- Maximum element size = **10**
- Select *Minimum element size*
- Maximum element size = **0.5**

A.2.7.11 Mesh 1/Free Triangular 2/Distribution 1

- Label = **Distribution 1**
- Boundary Selection
  - Selection = *Manual*
  - Select boundaries 4 and 8 (top of T3, see Appendix Figure A - 22)
- Distribution
  - Distribution type = *Fixed number of elements*
  - Number of elements = **floor(mesh_dist/4)**

A.2.7.12 Mesh 1/Free Triangular 1/Distribution 2

- Label = **Distribution 2**
- Boundary Selection
  - Selection = *Manual*
  - Select boundaries 6 and 9 (bottom of T1 boundary, see Appendix Figure A - 22)
- Distribution
  - Distribution type = *Fixed number of elements*
  - Number of elements = **floor(mesh_dist/2)**

→ *Mesh 1, select Build All*

A.3 Study 1

- Label = **Study 1**
- Study Settings
  - Select *Generate default plots*
  - Select *Generate convergence plots*

A.3.1 Step 1: Time Dependent

- Label = **Time Dependent**
  - Study Settings
  - Time Unit = *a*

        - Times = **range(0,0.01,100)**
            - Note: This is running for 100 years. Adjust as needed.
        - Tolerance = *Physics controlled*
    - Results While Solving
        - *Plot* (leave unselected)
        - Probes = *All*
        - Update at = *Time steps taken by solver*
    - Physics and Variables Selection
        - *Modify model configuration for study step*, (leave unselected)
        - *Darcy's Law (dl),* Select *Solve for*, Discretization = *Physics Settings*
        - *Heat Transfer in Porous Media (ht),* Select *Solve for*, Discretization = *Physics Settings*
        - *Flow Coupling 1 (fc1),* Select *Solve for*
        - *Temperature Coupling 1 (tc1),* Select *Solve for*
    - Values of Dependent Variables
        - Initial values of variables solved for
            - Settings = *Physics controlled*
        - Values of variables not solved for
            - Settings = *Physics controlled*
        - Store fields in output
            - Settings = *All*
    - Mesh Selection
        - Geometry = Geometry 1
        - Mesh = *Mesh 1*
    - Study Extensions
        - No selections

A.4 Data Tables

base_x	20[m]	20 m	X-coordinate for pile centre (bottom)
beta_wf	333.7e3[J/kg]	3.337E5 J/kg	Latent heat of fusion
cc_temp	0.056[K]	0.056 K	Temperature Increase due to Climate Change
cv_i_f	2.38e6[J/(m^3*K)]	2.38E6 J/(m³·K)	Frozen bulk heat capacity of Type I soil
cv_i_u	2.40e6[J/(m^3*K)]	2.4E6 J/(m³·K)	Thawed bulk heat capacity of Type I soil
cv_ic	1.6e6[J/(m^3*K)]	1.6E6 J/(m³·K)	Volumetric Heat capacity of type I material
cv_iii_f	2.13e6[J/(m^3*K)]	2.13E6 J/(m³·K)	Frozen bulk heat capacity of Type III soil
cv_iii_u	2.15e6[J/(m^3*K)]	2.15E6 J/(m³·K)	Thawed bulk heat capacity of Type III soil
cv_till_f	2.13e6[J/(m^3*K)]	2.13E6 J/(m³·K)	Frozen bulk heat capacity of till
cv_till_u	2.51e6[J/(m^3*K)]	2.51E6 J/(m³·K)	Thawed bulk heat capacity of till
gt_offset	4.999315537[year]	1.5776E8 s	Offset from July 2010 (start)
gt_phase	1.188[rad]	1.188 rad	Ground phase change
h_t1	3[m]	3 m	Height of T1 layer
h_t3	80[m]	80 m	Height of T3 layer
h_till	1.5[m]	1.5 m	Height of till layer
ki	1.65[J/(K*m*s)]	1.65 W/(m·K)	Thermal Conductivity of Type I material
ki_c	0.71[J/(K*m*s)]	0.71 W/(m·K)	Thermal Conductivity of Type I (Coarse) material
kiii	1.8[J/(K*m*s)]	1.8 W/(m·K)	Thermal Conductivity of Type III material
ktillf	3.2[J/(K*m*s)]	3.2 W/(m·K)	Frozen thermal conductivity of till
ktillu	3.2-0.29[J/(K*m*s)]	2.91 W/(m·K)	Thawed thermal conductivity of till
logi_k	5	5	Logistic equation factor k
mesh_dist	200	200	Distribution of Nodes along upper boundary
mm_air	28.97[g/mol]	0.02897 kg/mol	Molar mass of air
model_width	30	30	Width of model
Patm	101.3[kPa]	1.013E5 Pa	Atmospheric Pressure
perm_t1	2e-9[m^2]	2E-9 m²	Permeability of T1 Waste rock
perm_t1c	4e-7[m^2]	4E-7 m²	Permeability of T1 (Coarse) Waste rock
perm_t3	2e-9[m^2]	2E-9 m²	Permeability of T3
perm_till	5e-16[m^2]	5E-16 m²	Permeability of Till
poro	0.25	0.25	Porosity of Waste
poro_tic	0.30	0.3	Porosity of T1 (coarse)
poro_till	0.2	0.2	Porosity of Till
R	8.3145[m^3*Pa/(K*mol)]	8.3145 J/(mol·K)	Ideal Gas Constant
rho_s	2700[kg/m^3]	2700 kg/m³	Density of Bulk Waste Rock
rho_till	2650[kg/m^3]	2650 kg/m³	Solids Density of Till Material
rho_w	1000[kg/m^3]	1000 kg/m³	Density of water
t_trans	273.15-0.2[K]	272.95 K	Transition Temperature for Phase Change
t1_mesh_max	3[m]	3 m	Maximum Mesh Parameter Setting
t1_mesh_min	0.01[m]	0.01 m	Minimum mesh parameter setting
vmc_till	0.18	0.18	Volumetric Moisture Content of Till
vmc_waste	0.06	0.06	Volumetric Moisture Content of Waste (T1, T3)
year	365.25[day]	3.1558E7 s	Seconds in a year

Appendix Table A - 1: Parameters 1

-(h_t1+h_till)	12.91861252
9.5	-2.119209677
9.696774194	-2.205787781
9.916129032	-2.292604502
10.35483871	-2.321543408
10.68387097	-2.292604502
11.23225806	-2.205787781
11.89032258	-2.090032154
12.43870968	-1.916398714
13.43771195	-1.621050308
13.86451613	-1.482315113
14.30322581	-1.337620579
14.8516129	-1.221864952
15.50084725	-1.053694238
16.49677419	-0.78778135
17.63081095	-0.524802986
19.47061211	-0.178619621
21.4669921	-0.063225166
22.7483871	-0.064308682
23.95060218	-0.109382948
26.30446782	-0.159387212
28.12258065	-0.209003215
29.9526194	-0.236316848
31.63225806	-0.209003215
33.12334055	-0.188235825
34.48387097	-0.151125402
35.47096774	-0.180064309
36.73504705	-0.186312584
38.87096774	-0.209003215
38.9	-0.21386129
h_t3	-0.21386129

Appendix Table A - 2: Interpolation 1

cs_i_f	cv_i_f/rho_bulk_i	J/(kg·K)	Specific Heat Capacity of frozen Type I
cs_i_u	cv_i_u/rho_bulk_i	J/(kg·K)	Specific Heat Capacity of thawed Type I
cs_ic	cv_ic/rho_bulk_ic	J/(kg·K)	Specific Heat capacity of Type I (coarse) material
cs_iii_f	cv_iii_f/rho_s	J/(kg·K)	Specific Heat Capacity of frozen Type III
cs_iii_u	cv_iii_u/rho_s	J/(kg·K)	Specific Heat Capacity of thawed Type III
cs_till_f	cv_till_f/rho_bulk_till	J/(kg·K)	Specific Heat Capacity of Frozen Till
cs_till_u	cv_till_u/rho_bulk_till	J/(kg·K)	Specific Heat Capacity of Unfrozen Till
D	d(H,T)	1/K	Differential of Scaling factor for Latent Heat
gmc_till	vmc_till*rho_w/((1-poro_till)*rho_till+vmc_till*rho_w)		Gravimetric Moisture content of Till
gmc_waste	vmc_waste*rho_w/((1-poro)*rho_s+vmc_waste*rho_w)		Gravimetric Moisture content of Waste
H	1/(1+exp(-2*logi_k*tt[1/K]))		Frozen-Unfrozen Scaling Factor
nu_air	mat5.def.mu/rho_air	m²/s	Kinematic Viscosity of Air
Ps	Patm-rho_air*g_const*(y)	Pa	Surface Pressure
Ra	(rho_air)*(g_const)*(1/T)*(perm_t1c)*(h_t1)*(mat5.def.Cp)*(abs(opTop(T)-opBot(T)))/((nu_air)*(ki_c))		Rayleigh's Value at Centre of T1 (coarse) layer
rho_air	p*mm_air/(R*T)	kg/m³	Density of Air
rho_bulk_i	rho_s*(1-poro)+rho_w*vmc_waste	kg/m³	Bulk density of Type I Material
rho_bulk_ic	rho_s*(1-poro_tic)+rho_w*0	kg/m³	Bulk density of Type I (Coarse) Material
rho_bulk_till	rho_till*(1-poro_till)+rho_w*vmc_till	kg/m³	Bulk density of Till Material
Ts	(-6.3+20.4*sin((2*pi/(year))*(t+gt_offset)+gt_phase)+(cc_temp[1/K]/(year))*(t+gt_offset))[degC]	K	Surface temperature, top of pile [K]
tt	T-t_trans	K	Transition Temp for surface

Appendix Table A - 3: Variables 1